

ALMA MATER STUDIORUM – UNIVERSITÀ DI BOLOGNA

DIPARTIMENTO DI INGEGNERIA DELL'ENERGIA ELETTRICA E DELL'INFORMAZIONE

SCUOLA DI DOTTORATO IN AUTOMATICA E RICERCA OPERATIVA

CICLO XXIX

SETTORE CONCORSUALE : AREA 09/G1

SETTORE SCIENTIFICO DISCIPLINARE : AUTOMATICA (ING-INF/04)

Design and Implementation of Innovative Robotic Devices Using Twisted String Actuation (TSA) System

Coordinatore Dottorato:
Chiar.mo Prof. Daniele Vigo

Relatore:
Chiar.mo Prof. Claudio Melchiorri

Correlatore:
Prof. Gianluca Palli

*Tesi conforme ai requisiti per il rilascio del titolo di Dottore di Ricerca
in
Automatica e Ricerca Operativa*

Mohssen Hosseini

Marzo 2017

UNIVERSITY OF BOLOGNA

DEPARTMENT OF ELECTRICAL, ELECTRONIC AND INFORMATION ENGINEERING

DOCTORAL SCHOOL OF AUTOMATION AND OPERATIONAL RESEARCH

XXIX CYCLE

Design and Implementation of Innovative Robotic Devices Using Twisted String Actuation (TSA) System

Ph.D. Coordinator:

Prof. Daniele Vigo

Supervisor:

Prof. Claudio Melchiorri

Co-Supervisor:

Prof. Gianluca Palli

*A thesis submitted in fulfillment of the requirements
for the degree of Doctor of Philosophy*

in

Automations and Operational Research

by

Mohssen Hosseini

March 2017

“Do you know what you are?
You are a manuscript a divine letter.
You are a mirror reflecting a noble face.
This universe is not outside of you.
Look inside yourself; everything that you want,
you are already that.”

— Rumi (Persian poet)

I would like to dedicate this thesis to my loving parents.

For their endless love, support and encouragement.

Declaration

I hereby declare that except where specific reference is made to the work of others, the contents of this dissertation are original and have not been submitted in whole or in part for consideration for any other degree or qualification in this, or any other university. This dissertation is my own work and contains nothing which is the outcome of work done in collaboration with others, except as specified in the text and Acknowledgements.

Mohssen Hosseini

March 2017

Acknowledgements

The completion of my dissertation and subsequent Ph.D. has been a long journey. It's true that "life is what happens" when you are completing your dissertation. Life doesn't stand still nor wait until you are finished and have time to manage it.

I would like to express my special appreciation and thanks to my Ph.D. supervisor, Professor Dr. Claudio Melchiorri, head of DEI. You have been a tremendous mentor for me, and I would like to thank you for encouraging my research and growth as a research scientist. Your advice on both research, as well as on my career, have been priceless.

I would also like to thank my co-supervisor, Professor Dr. Gianluca Palli, for his valuable guidance, scholarly inputs and consistent encouragement that I received throughout the research work. He is a person with an amicable and positive disposition and always made himself available to help me.

I couldn't have survived the past few years if not for all my friends at LAR. A support network is always important, but one with a sense of humor is even better.

And last but definitely not least, a special thanks to my family. Words cannot express how grateful I am to my father, my mother, my brother and my sister for all of the sacrifices that you've made on my behalf. Your prayers for me are what have sustained me thus far.

Abstract

The twisted string actuation system is particularly suitable for very compact, low-cost and light-weight robotic devices, like artificial limbs and exoskeletons, since it allows the implementation of powerful tendon-based driving systems, based on small-size DC motors characterized by high speed, low torque and very limited inertia.

The following activities has been done using the Twisted String Actuation System:

- The basic properties of the twisted string actuation system.
- An ongoing work for verifying the behavior of a twisted string actuator in contact with a sliding surface or guided through a sheath.
- The implementation of a variable stiffness joint actuated by a couple of twisted string actuators in antagonistic configuration.
- The design and the implementation of a force sensor based on a commercial optoelectronic component called light fork and characterized by the simple construction process.
- A twisted string actuation module with an integrated force sensor based on optoelectronic components.
- The preliminary experimental study toward the implementation of an arm rehabilitation device based on a twisted string actuation module.
- A 6 DoF cable-driven haptic interface for applications in various robotic scenarios.

- A wearable hand haptic interface driven by a couple of twisted string actuators.

Table of contents

List of figures	xvii
List of tables	xxiii
1 Introduction	1
2 Twisted String Actuation (TSA) System	5
2.1 Modeling of the TSA	7
3 Twisted String Actuation with Sliding Surfaces	17
3.1 Modeling of the TSA in contact with external elements	18
3.2 Input-Output Characteristic	25
3.3 Output Feedback Control	29
3.4 Conclusions	30
4 A Variable Stiffness Joint Based on TSA System	33
4.1 Dynamic Model of The Variable Stiffness Joint	34
4.2 Control Algorithms	38

4.3	System Design	39
4.4	Actuation Module	40
4.5	System Identification	42
4.6	Conclusions	48
5	Force Sensor	51
5.1	Sensor Design	55
5.1.1	Sensor Structure	55
5.1.2	Sensor Working Principle	57
5.1.3	Compliant Frame Design	64
5.2	Specimen Design and Experimental Evaluation	67
5.2.1	Experimental Setup	67
5.2.2	Specimen Design and Comparison	69
5.2.3	Static Calibration	70
5.2.4	Dynamic Sensor Response	72
5.2.5	Evaluation of measurement noise	76
5.3	Conclusions	79
6	Actuation Module	81
6.1	System Description	83
6.1.1	TSA Module Structure	85
6.1.2	Sensor Working Principle	86

6.1.3	Force Sensor Design	87
6.1.4	Validation of the Actuation Module Design	88
6.2	Experimental Evaluation	89
6.2.1	Experimental Setup	89
6.2.2	Force Sensor Calibration	91
6.2.3	Input-Output Characteristic	92
6.2.4	System Responses	92
6.3	Conclusions	94
7	A Wearable Robotic Device Based on TSA	97
7.1	System Description	99
7.1.1	TSA Module Design	100
7.2	Experimental Evaluation of the TSA Module as an Assistive Device . . .	103
7.2.1	Hardware and setup overview	103
7.2.2	Experiment Configuration, Control Scheme and Results	104
7.3	Conclusions	109
8	A Haptic Interface based on TSA	111
8.1	System Design	114
8.1.1	Overall System Description	114
8.1.2	The TSA Module	116
8.2	Conclusions and Future Works	117

9 A Wearable Robotic Hand Exoskeleton	119
9.1 System Description	122
9.1.1 Fingers Structure	122
9.1.2 Design of the Hand Exoskeleton	122
9.1.3 Control of the System	125
9.2 Conclusions	125
10 CONCLUSIONS	127
Appendix A Feedback Linearization of VSA Based on TSA	131
A.1 Control Algorithms	131
A.1.1 Static Model Inversion	132
A.1.2 Feedback Linearization	134
A.1.3 Control of the Feedback-Linearized System	137
A.2 Conclusions	142
Appendix B PUBLICATIONS	145
References	149

List of figures

- 2.1 Using ropes in transmission systems in ancient time. 7
- 2.2 Using ropes in military application in ancient time. 8
- 2.3 Basic concept of the twisted string actuation system. 9
- 2.4 Twisted string transmission sections for different values of the parameters n and rc . (a) String section with $n = 6$. (b) Two-string section with null core radius ($n = 2$).. . . . 9
- 2.5 Schematic representation of the helix formed by the strands that compose the twisted string. 10
- 2.6 Simplified geometry and force distribution of the twisted string transmission (sectional view, $n = 2$)... 11

- 3.1 Experimental setup of the TSA guided by the teflon tube and environmental constraints. 19
- 3.2 Schematic representation of the TSA in contact with an obstacle. 20
- 3.3 Schematic representation of the dynamic model of the TSA in contact with environmental constraints (s denotes the Laplace variable). 22
- 3.4 Input output position characteristic with constant load. 24

3.5	Input output position characteristic with spring-like load.	25
3.6	Output load position control with ramp setpoint.	26
3.7	Output load position control with 0.5Hz sinusoidal setpoint.	28
3.8	Output load position control with 1Hz sinusoidal setpoint.	28
3.9	Output load position control with 2Hz sinusoidal setpoint.	30
3.10	Output load position control with step setpoint.	31
4.1	Schematic representation of the rotative joint with two twisted string transmission systems.	34
4.2	Stiffness of the link versus motor positions, no external load is assumed. .	35
4.3	Admissible external torque across possible motor positions.	36
4.4	Position of the motor A (top) and B (bottom) over the joint stiffness and position variation range.	38
4.5	Top view of the experimental setup.	40
4.6	Detail of the actuation module.	41
4.7	Identification of the joint characteristics.	44
4.8	Identification of the motor response.	45
4.9	Identification of the joint response.	47
5.1	Schematic view and design of the proposed force sensor: the compliant frame structure and the detailed view of the light fork and obstacle ar- rangement.	56
5.2	Detailed view of the light fork (from OMRON EE_SX1108 datasheet). .	57

5.3	Schematic representation of the LED-PD interaction.	58
5.4	Measuring circuit for the force sensor based on optoelectronic component.	60
5.5	Responsivity curve of the light fork: it is possible to note the variation of the PD current (about 70%) with respect to the obstacle displacement (0.12 mm) from the point A to the point B.	61
5.6	Responsivity curve of the light fork.	62
5.7	Deflection of curved beam	64
5.8	Overview of the experimental setup.	68
5.9	FEA of the four compliant frame specimens.	71
5.10	Comparison between theoretical, FEA and experimental deformation of the three compliant frame specimens.	72
5.11	Static calibration of the sensors.	74
5.12	Evaluation of the response to a chirp signal varying from 0.1 to 20 Hz for the four sensor specimens.	75
5.13	Experimental evaluation of the force sensor hysteresis for the different specimens at frequencies ranging from 0.2 to 2 Hz.	77
5.14	Measuring circuit with PWM LED modulation for noise reduction. . . .	78
5.15	Comparison of the measurement spectrum with and without LED pulsing.	78
6.1	Schematic representation of the twisted string actuation system structure.	82
6.2	Conceptual view of an elbow exoskeleton based on the twisted string actuation module.	83
6.3	Detail of the twisted string actuation module.	84

6.4	Scheme of the sensor structure and component arrangement.	85
6.5	Finite Element Analysis (FEA) of the compliant frame.	87
6.6	Deformation of the motor module in the direction of the transmission:comparison between experimental values and FEA.	88
6.7	Overview of the experimental setup.	89
6.8	Static Calibration.	90
6.9	Input output position characteristic with constant load (right) and with spring-like load (left).	91
6.10	Experimental evaluation of the constant load	93
6.11	Experimental evaluation of the Spring-like load	94
7.1	Conceptual view of an elbow exoskeleton based on the twisted string actuation module.	98
7.2	Detailed view of the TSA module prototype and control electronics. . . .	100
7.3	Overview of the experimental setup.	102
7.4	Plots for the lifting task without the assistive device support.	105
7.5	Variable stiffness control scheme of the TSA module for the assistive ap- plication.	107
7.6	Plots for the lifting task with the assistive device support.	108
8.1	CAD rendering of the proposed haptic interface.	113
8.2	Schematic view of the haptic interface and actuators arrangement.	114
8.3	Using ropes in transmission systems in ancient time.	115

8.4	Detail of the TSA module design.	116
8.5	Detailed view of the TSA module prototype and control electronics.	117
9.1	Detailed view of the hand exoskeleton.	120
9.2	Detail of the actuation module.	121
9.3	Detailed view of the fingers structure.	122
9.4	Detail view of the hand exoskeleton.	123
9.5	Detailed veiw of the finger supports.	124
A.1	Top view of the experimental setup.	132
A.2	Position and stiffness response with constant stiffness setpoint.	133
A.3	Position and stiffness response with variable stiffness setpoint.	134
A.4	Simulation of the joint system with feedback linearization control: sinusoidal position setpoint and constant stiffness.	138
A.5	Simulation of the joint system with feedback linearization control: constant position setpoint and sinusoidal stiffness setpoint.	139
A.6	Simulation of the joint system with feedback linearization control: sinusoidal position setpoint and sinusoidal stiffness setpoint.	143

List of tables

- 4.1 Identified joint response parameters. 46

- 5.1 Parameters of the four compliant frame specimens. 68

- 5.2 RMS errors with respect to the experimental deformation measurements of the four compliant frame specimens (values are expressed as a percentage of the maximum deformation). 73

- 5.3 Maximum deformation of the four compliant frame specimens. 73

- 5.4 Linearity error of the calibration curve 74

- 5.5 Mean hysteresis areas for different frequency values (areas are expressed in N²). 76

- 5.6 Accuracy of the developed sensors for the four specimens. 76

Chapter 1

Introduction

The twisted string actuation system is a very simple, extremely low-cost, compact and lightweight actuation system, particularly suitable for highly integrated robotic devices designed or interacting with humans and unknown environments like artificial limbs and exoskeletons, since it renders a very low apparent inertia at the load side, allowing the implementation of powerful tendon-based driving systems, using small-size DC motors characterized by high speed, low torque and very limited inertia. The basic properties of the twisted string actuation system have been discussed in [Chapter 2](#).

In [Chapter 3](#), an ongoing work for verifying the behavior of a twisted string actuator in contact with a sliding surface or guided through a sheath is presented. One of the major limitations of this actuation system is by now related to the fact that the string should not be in contact with any obstacle, because this contact will alter the twisting angle propagation along the string and, eventually, completely stop the string twisting. This design constraint imposes a straight path between the motor and the linear load attached to the other string end. A model of the twisted string in contact with a sliding surface is discussed and the behavior of the system has been then experimentally verified and discussed. A preliminary evaluation of control strategies for compensating the side

effects generated by the contact of the twisted string with the sliding surface is also presented.

In Chapter 4, the implementation of a variable stiffness joint actuated by a couple of twisted string actuators in antagonistic configuration is presented. A simple PID-based motor-side algorithm for controlling simultaneously both the joint stiffness and position is discussed, then the identification of the system parameters is performed on an experimental setup for verifying the proposed model and control approach.

The design and the implementation of a force sensor based on a commercial optoelectronic component called light fork and characterized by the simple construction process is presented in Chapter 5. The proposed sensor implementation is designed to measure the force applied by a cable-based actuation, called twisted string actuation system, by detecting the deformation of a properly designed compliant structure integrated into the actuation module. Despite this, the design method here presented allows to adapt the sensor to a large set of robotic applications, thanks to its simplicity in the construction and low cost. The main advantages of the proposed sensor consist in the use of a very compact commercial optoelectronic component, called light fork, as sensing element. This solution allows a very simple assembly procedure together with a good sensor response in terms of sensitivity, linearity and noise rejection to be achieved using an extremely simple electronics, thereby obtaining in this way a reliable and very cheap sensor that can be easily integrated in actuation modules for robots and can easily be adapted to a wide application set.

Chapter 6 implements a twisted string actuation module with an integrated force sensor based on optoelectronic components. The adopted actuation system can be used for a wide set of robotic applications, and is particularly suited for very compact, lightweight and wearable robotic devices, such as wearable rehabilitation systems and ex-

oskeletons. Then the preliminary experimental activity toward the implementation of an arm rehabilitation device based on a twisted string actuation module is reported.

A conceptual design of a wearable arm assistive system based on the proposed actuation module is presented in Chapter 7. Moreover, the actuation module has been used in a simple assistive application, in which surface-electromyography signals are used to detect muscle activity of the user wearing the system and to regulate the support action provided to the user to reduce his effort, showing in this way the effectiveness of the approach.

In Chapter 8, a 6 DoF cable-driven haptic interface for applications in various robotic scenarios is presented. The device takes advantage of four force-controlled twisted string actuators to generate a force in the Cartesian space while providing a considerable force-weight ratio and low inertia. The system consists of a frame fixed to the ground, where the four twisted string actuation modules are arranged, and by a mechanical interface devoted to the physical connection of the actuators with the forearm of the human operator. This mechanical interface allows to secure the forearm of the user while leaving to her/him the freedom to use the hand to accomplish other tasks, such as teleoperating a robotic gripper. The four twisted string actuators allow to control the three linear DoF of the haptic interface, allowing both Cartesian position and a force regulation. The design and the preliminary implementation of the haptic interface are presented in this work.

Chapter 9 presents a wearable hand haptic interface driven by a couple of twisted string actuators. This device is able to provide independent force feedback to the thumb on one side, and to the the index to little fingers grouped together on the other side. This configuration has been selected to provide the user with force feedback during the execution of grasping tasks by means of a teleoperated robotic manipulator. Therefore,

the design of the hand exoskeleton, the description of the actuation system and of the embedded controller has been presented.

In Appendix A, a theoretical investigation about the use of the TSA principle for the implementation of a variable stiffness mechanism using two actuators in antagonistic configuration is reported. Then aiming at improving the control system performance, a feedback linearization approach and a linear optimal control strategy are adopted to achieve fully decoupled control of the position and the stiffness profiles.

Chapter 2

Twisted String Actuation (TSA)

System

The string is known as one of the oldest means of transmitting power over a distance [1]. Several thousand years ago humans started using ropes in transmission systems such as woodworking and making the fire, see Fig. 8.3. Twisted rope transmission systems, were used in construction (windlasses), in military applications [2], such as catapults and ballistae and in many different applications, see Fig. 2.2. This actuation is able to transmit high forces with a very low input torque, while remaining mechanically simple and reliable.

Some similar actuation concept can be found in the literature. In [3], [4] and [5], the LADD actuator composed of number of cells connected end to end, and each cell consists of two rings joined by several high strength fibers. As each cell is twisted, the distance between the rings decreases, thus transforming rotary motion into linear motion. The Twist Drive actuator [6] and [7], uses two short strings that twist on each other to

produce a pulling force. The Twist Drive uses a DC motor with a speed reducer allowing a compact implementation of the actuator.

The Twisted String Actuation (TSA) concept [8, 9] represents a very interesting design solution for the implementation of very compact and low cost linear transmission systems. Indeed, with an proper choice of the strings parameters (in particular the radius and length), it is possible to easily satisfy the usually tight requirements for the implementation of miniaturized and highly-integrated mechatronic devices. As a proof of its benefits and advantages, the TSA has been already successfully used for the implementation of different robotic devices like robotic hands [10, 11], exoskeletons [12] and tensegrity robots for space applications [13]. The mathematical model of the TSA and, in particular, the analysis of its force/position characteristic and of the resulting transmission stiffness has been investigated in [9]. Recently, the TSA model has also been improved taking into account the characteristics of different type of strings and a non constant string radius in [1] and its stiffness variability [14].

The basic idea of the actuation system is quite simple: as schematically illustrated in Fig. 2.3, a couple of strings are connected in parallel on one end to a rotative electrical motor and on the other end to the load to be actuated. The rotation imposed to the strings by the electrical motor reduces their length, generating a linear motion at the load side.

The main advantages of this actuation system compared to conventional solutions, consist in the direct connection between the motor and the tendon without any intermediate mechanisms such as gearboxes, pulleys or ballscrews. This actuation concept, because of its high (though nonlinear) reduction ratio, permits the use of very small and lightweight electric motors and therefore is very interesting in applications where size and weight are of crucial importance.

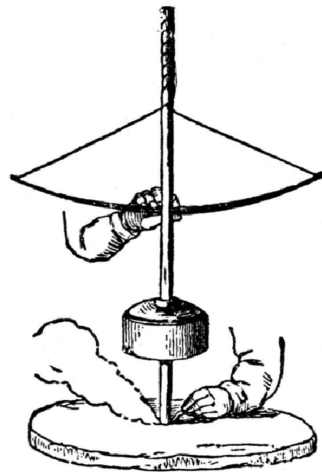
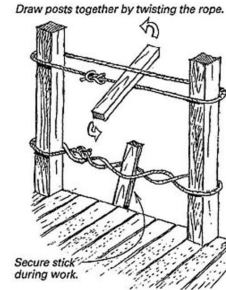
(a) Making fire ^a.^awww.karenswhimsy.com(b) Using rope in some application ^a.^awww.finehomebuilding.com

Fig. 2.1 Using ropes in transmission systems in ancient time.

2.1 Modeling of the TSA

The kinetostatic model[9] takes into account the effects of the finite string dimensions and elasticity, together with the case of multiple strands forming a single string. This analysis will provide some useful information for the design of the actuation system and for the choice of the driving motors as well as indicates the limits of the stroke and reduction ratio of the transmission system.

As a simplifying hypothesis, it is assumed here that some strands do not contribute to the total axial force: these fibers form the core of radius r_c of the helix [see Fig. 2.4a]. The load force F_z is balanced by the n external strands of radius r_s which form n coaxial helices of radius $r = r_s + r_c$. As a limit case, Fig. 2.4b shows a string formed by a pair of twisted strands, for which $r_c = 0$ and thus $r = r_s$, considering the helices formed by the strand axes.

In order to obtain the relationships describing the statics of the TSA system, we assume that the strands constituting the string form an ideal helix of constant radius

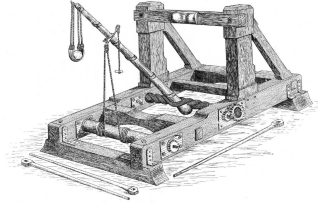
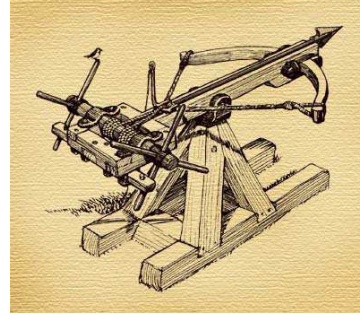
(a) catapult ^a.^awww.ancient-origins.net(b) ballistae ^a.^awww.pinterest.com

Fig. 2.2 Using ropes in military application in ancient time.

$r = r_c + r_s$ along the whole range of the motor angular position θ . The kinematic relationship between the motor angle and the load position can be easily derived from the geometry of the helix formed by the strings, see in particular Fig. 2.5, which implies the following straightforward relations:

$$L = \sqrt{\theta^2 r^2 + p^2} \quad (2.1)$$

$$\sin \alpha = \frac{\theta r}{L} \quad (2.2)$$

$$\cos \alpha = \frac{p}{L} \quad (2.3)$$

$$\tan \alpha = \frac{\theta r}{p} \quad (2.4)$$

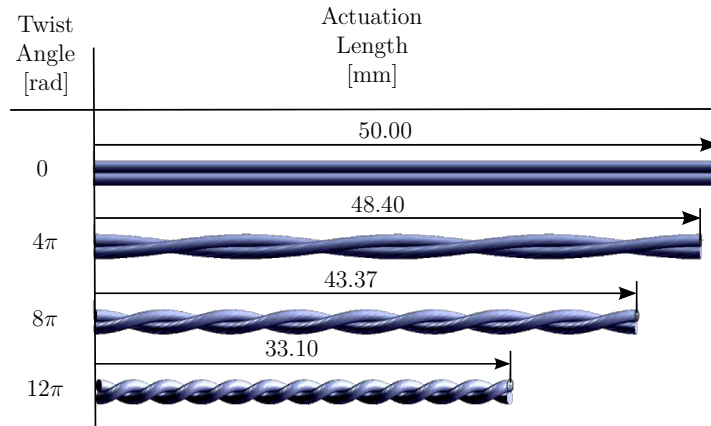


Fig. 2.3 Basic concept of the twisted string actuation system.

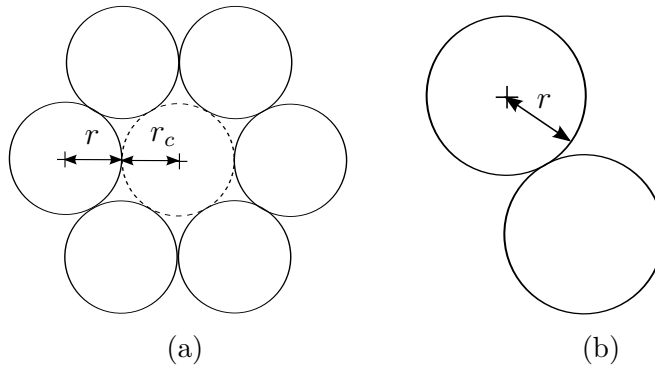


Fig. 2.4 Twisted string transmission sections for different values of the parameters n and rc . (a) String section with $n = 6$. (b) Two-string section with null core radius ($n = 2$).

where α is the helix slope, L is the strand length and p is the length of the transmission system or, in other words, the load relative position wrt the motor. Note that eq. (2.1) can be easily obtained by “unwrapping” the helix of total length L and radius r and applying Pythagoras’ theorem to the resulting triangle.

From eqs. (2.1), (2.2), (2.3) and (2.4) it follows that:

$$\dot{L} = \dot{p} \cos \alpha + \dot{\theta} r \sin \alpha. \quad (2.5)$$

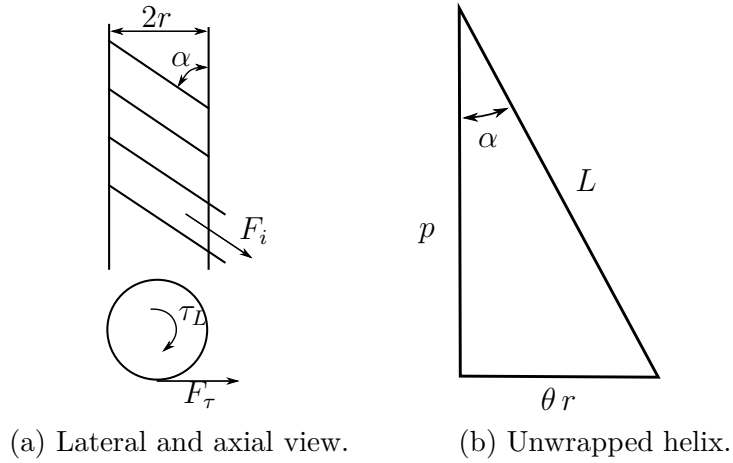


Fig. 2.5 Schematic representation of the helix formed by the strands that compose the twisted string.

The static model of the actuation system can be easily obtained looking at Fig. 2.5, where the external torque τ_L is balanced by the tangential force F_τ , i.e.:

$$F_\tau = \frac{\tau_L}{r} \quad (2.6)$$

Assuming that the load is equally distributed over the n strands that form the string, one obtains

$$\frac{F_\tau}{n} = F_i \sin \alpha \Rightarrow \tau_L = rnF_i \sin \alpha \quad (2.7)$$

where F_i is the longitudinal feasible force in each strand. The resulting total axial force F_z acting on the transmission system is

$$F_z = nF_i \cos \alpha \Rightarrow \tau_L = F_z r \tan \alpha = F_z \frac{\theta r^2}{p} \quad (2.8)$$

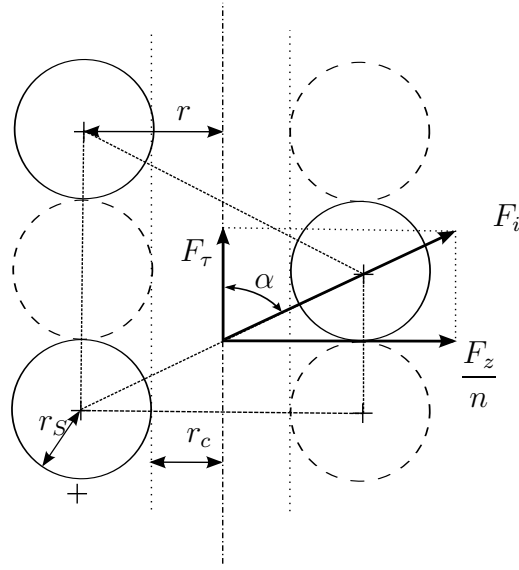


Fig. 2.6 Simplified geometry and force distribution of the twisted string transmission (sectional view, $n = 2$)...

In this analysis, the strings are assumed to act as linear springs, with the capability of resisting tensile (positive) forces only. With respect to the unloaded length L_0 , the total length of a string L changes according to the fiber tension F_i and the string stiffness K (normalized with respect to the length unit), i.e.

$$F_i = \frac{K}{L_0} (L - L_0) = \frac{K}{L_0} \left(\sqrt{p^2 + r^2\theta^2} - L_0 \right) \quad (2.9)$$

where r is the string radius, θ is the motor angle and p is the resulting length of the transmission system. It is worth noticing from (2.9) that the string acts as a spring whose deformation is defined as $\sqrt{p^2 + r^2\theta^2} - L_0$ and, therefore, can be modulated through the motor angular position θ . It follows that the transmission length p is given by:

$$p = \sqrt{L_0^2 \left(1 + \frac{F_i}{K}\right)^2 - \theta^2 r^2} \quad (2.10)$$

whereas, from the helix geometry, the pitch q of the helix is related to the string length p and to the motor rotation angle θ by the relation

$$2\pi p = q\theta \quad (2.11)$$

The external torque τ_L provided by the motor and the load force F_L can be derived from (2.9) and by the geometrical considerations on the system

$$\tau_L(\theta, p) = 2 \frac{\theta r^2 K}{L_0} \left(1 - \frac{L_0}{\sqrt{p^2 + r^2 \theta^2}}\right) \quad (2.12)$$

$$F_L(\theta, p) = 2 \frac{Kp}{L_0} \left(1 - \frac{L_0}{\sqrt{p^2 + r^2 \theta^2}}\right) \quad (2.13)$$

Moreover, the stiffness S of the transmission system can be modeled by computing the derivative of the load force F_L in (2.13) with respect to the load position p :

$$\begin{aligned}
S(\theta, p) &= \frac{\partial F_L}{\partial p} = \\
&= 2K \left(\frac{1}{L_0} - \frac{1}{\sqrt{p^2 + r^2\theta^2}} + \frac{p^2}{(p^2 + r^2\theta^2)^{3/2}} \right)
\end{aligned} \tag{2.14}$$

The previous relations show that the motor torque and the force along the string as well as the transmission stiffness depend on the twist angle θ and actuation length p .

The maximum actuator stroke (contraction) is computed by considering the maximum motor rotation angle before the string becomes closely wound. Fig. 2.6 shows a limit condition for the case of two strands ($n = 2$): due to their finite radius, a maximum value of the angle α exists such that the strands form a closely wound helix. With reference to Fig. 2.6 and with some simplifications on the system geometry, in the general case of n strands, this condition is given by

$$q_{min} = 2nr_s \tag{2.15}$$

Combining 2.10 and 2.11, the maximum motor angle and actuation contraction in the case of no load (i.e., $F_z = 0$, $F_i = 0$) can then be defined as

$$\theta_{max} = \frac{L_0}{\sqrt{r^2 + \frac{r_s^2 n^2}{\pi^2}}}, p_{min} = \frac{L_0}{\sqrt{\frac{\pi^2 r^2}{r_s^2 n^2} + 1}} \tag{2.16}$$

and the maximum no-load relative contraction is

$$\frac{L_0 - p_{min}}{L_0} = 1 - \frac{1}{\sqrt{\frac{\pi^2 r^2}{r_s^2 n^2} + 1}} \quad (2.17)$$

It is important to note that in case of null core radius ($rc = 0, n = 2$), the maximum actuation contraction is about 46% of the maximum string length L_0 .

From 2.2, 2.3, 2.4 and 2.11

$$\tan \alpha = \frac{2\pi r}{q} \quad (2.18)$$

and from 2.15, it is possible to note that the maximum helix slope is

$$\tan \alpha_{max} = \frac{\pi r}{nr_s} \quad (2.19)$$

The nonlinear kinetostatic model of the actuation system is summarized by the reduction ratio and by the relationship between the motor angle and the load displacement, derived as follows. From 2.8, 2.18 and 2.11, the generalized reduction ratio of the transmission can be found as

$$h(\theta, p) \equiv \frac{\tau_L}{F_z} = r \tan \alpha = \frac{\theta r^2}{p} \quad (2.20)$$

and it goes from $h(\theta, p) = 0$, when $\theta = 0$, to $h(\theta, p) = \frac{\pi r}{n}$, when $\theta = \theta_{max}$ and $r_c = 0$. The transmission length in unloaded and unwrapped configuration is equal to the string length L_0 and the actuation stroke Δp is given by

$$\Delta p = L_0 - p \equiv k_{(p)} \quad (2.21)$$

Chapter 3

Twisted String Actuation with Sliding Surfaces

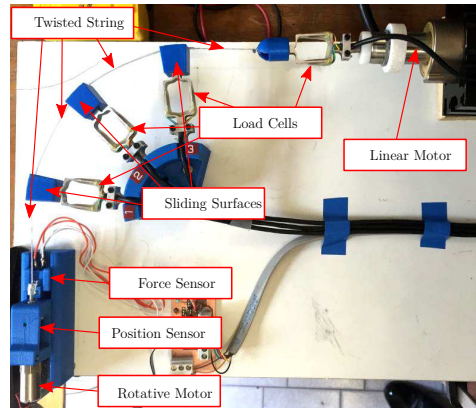
Even if in literature, some variants of the TSA exploiting environmental constraints to change or adjust the characteristics of the TSA [15], have been proposed, one of the major disadvantages of TSA is related to the fact that, by now, the transmission system should be not in contact with other structures because the generated friction will introduce deviations from the ideal behavior of the system. This fact limits in some way the applicability of the TSA concept or increases the space need for the actuators, in particular in case of robotic hands. Indeed, in the DEXMART Hand [11], the whole forearm length is exploited to host the TSAs driving the wrist and the fingers, and the TSAs are connected to a conventional tendon-based transmission system just before the wrist to avoid any TSA contact with the hand structure. The possibility of using the TSA even if the string is in contact with structural elements may introduce significant improvements in the design of such a robotic hand, reducing the space needed for hosting the actuation and allowing the optimization of the actuator arrangement.

In this chapter, an ongoing work for evaluating the TSA in contact with a sliding surface or guided by means of a Teflon sheath is reported. Particular attention is posed in both the modeling and the experimental verification of the hysteresis introduced in the transmission system by the friction. The chapter reports also the preliminary activity for the experimental evaluation of the system behavior and related control strategies.

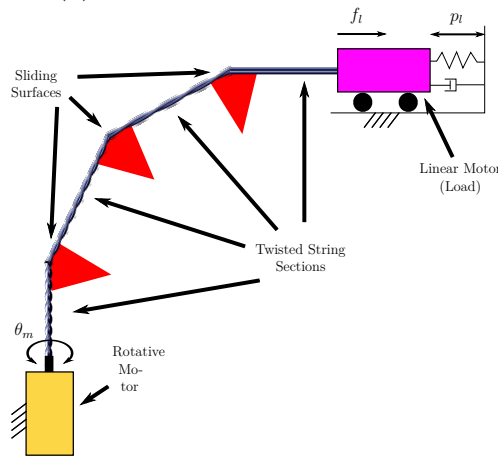
3.1 Modeling of the TSA in contact with external elements

In Figure. 3.1 an overview of the setup used for the evaluation of the TSA in contact with external elements is reported. The experimental setup is composed by a rotative motor used to twist the string on one end and a linear motor (LinMot-37×160) attached to the opposite string end acting as a load for the TSA. The linear motor is equipped with a load cell for measuring the load-side force and with a integrated high-resolution encoder ($1\mu\text{m}$) for load position measurement and it can be controlled to act as a modulable inertia or to apply a constant force compensating for the slider friction [16]. The rotative motor is hosted in a suitably developed motor module [17, 18] with integrated force sensor, position sensor and motor power electronics.

As can be seen in the detailed view of the experimental setup reported in Figure. 3.1, the twisted string is not straight from the rotative motor to the linear load, but it is deviated by three external elements, i.e. the sliding surfaces, emulating the environmental constraints or the structural parts of the robot, to form an arc of 90 degrees from the rotative motor to the load. In the investigation reported in this chapter, both the cases in which the string is directly in contact with the environmental constraints and the case in which the twisted string is passed through a Teflon tube to reduce the friction



(a) Overview of the experimental setup



(b) Schematic view of the experimental setup.

Fig. 3.1 Experimental setup of the TSA guided by the teflon tube and environmental constraints.

between the string and the environment are considered. The environmental constraints guiding the TSA are also equipped with load cells for measuring the resultant constraint force: this information allows to estimate the friction acting on the string, but these data are not reported here for brevity and will be subject to future investigation. This particular structure of the experimental setup allows a deeper investigation of both the friction effects and the TSA behavior, since the state of the system can be evaluated in some intermediate points along the curvature from the rotative motor to the load. In particular, it is here assumed that the string parts not in contact with the obstacles behaves as ideal TSA according to the model described in Sec. 2.1 (see [9] for further de-

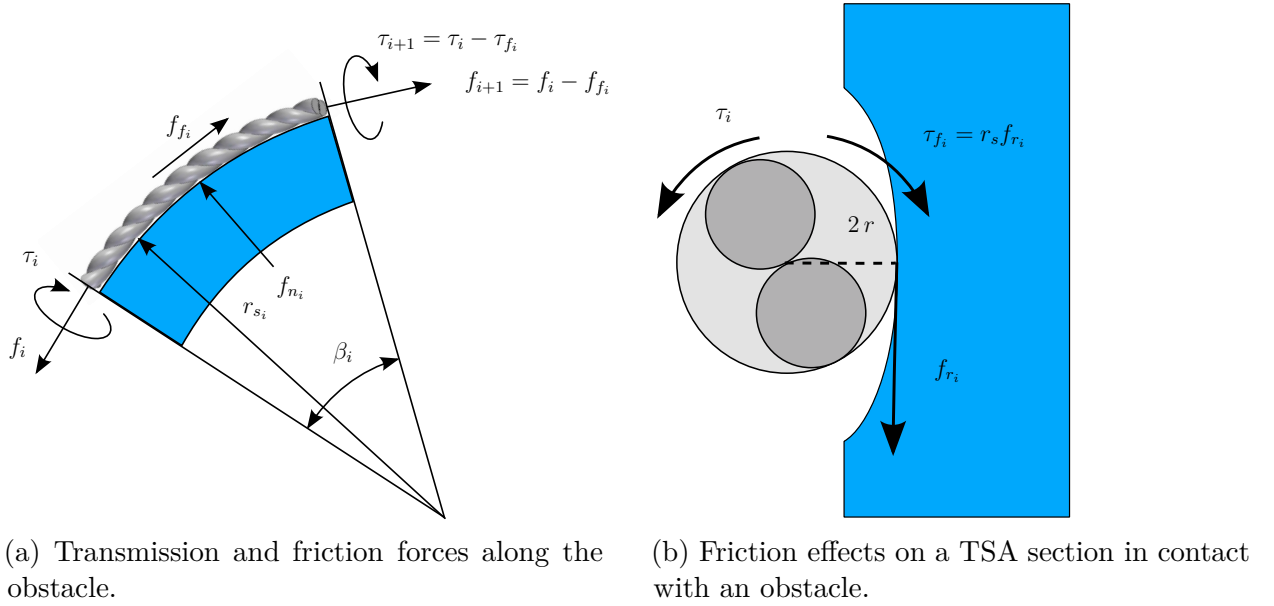


Fig. 3.2 Schematic representation of the TSA in contact with an obstacle.

tails). On the other hand, the contact of the TSA with a sliding surface will be modeled adopting the same assumptions regarding the distribution of the load along the string typical of tendon-based transmission systems, and the effect of the string twisting will be included for completing the system model. According to what reported in [19] about the modeling of tendon-based transmission systems, the string path can be represented as an arc connecting the input and the output string directions, as schematically represented in Figure. 3.2a. In this picture, the force f_{f_i} represents the overall friction effect along the string on the i -th sliding surface characterized by a curvature angle $\beta_i = 30$ deg and by a radius $r_{s_i} = 100$ mm, whereas f_{n_i} represents the normal force acting on the sliding surface given by the combined effect of the string deviation and tension force. It follows that, referring to f_i as the input force applied to the twisted string on the rotative motor side of the sliding surface, the output force on the load side is decremented by the effect of friction, i.e. $f_{i+1} = f_i - f_{f_i}$. Differently from the case of conventional tendon-based transmissions, in the case of TSA also the torque propagation from the motor to the load side of the sliding surface plays a crucial role since this torque causes the twist of

the string itself. In Figure. 3.2a also the input and the output torques acting on the twisted string, τ_i and τ_{i+1} respectively, are represented. While in the case of ideal (with no contact) TSA, the torque is constant along the whole string length, in case of contact with some obstacle (i.e. the sliding surface), a friction force f_{r_i} emerges, generating a counteracting torque also, namely τ_{f_i} . From the schematic representation of a section of the TSA interacting with an obstacle reported in Figure. 3.2b, it can be seen that the obstacle surface friction generates a counteracting torque proportional to the TSA radius. Assuming for simplicity that the overall effect on the TSA torque propagation of the i -th obstacle is concentrated in a single point, it is possible to write $\tau_{f_i} = 2r f_{r_i}$ where r represents the string radius. It follows that $\tau_{i+1} = \tau_i - \tau_{f_i}$. As a simplifying assumption, we assumed the friction f_{f_i} affecting the string transmission force and the friction force f_{r_i} can be independently treated, allowing to deal with the force and torque propagation as two independent phenomenon.

Following the analysis reported in [19], the normalized value of the friction coefficient $\bar{\mu}_{d_i}$ and of the normal load \bar{f}_{n_i} are introduced:

$$v_{s_i} = \text{sign}(v_{r_i}) \quad (3.1a)$$

$$\bar{\mu}_{d_i}(v_{s_i}) = \frac{|1 - e^{-\mu_d \beta_i v_{s_i}}|}{1 + e^{-\mu_d \beta_i v_{s_i}}}, \quad \bar{\mu}_{s_i} = \bar{\mu}_{d_i} \frac{\mu_s}{\mu_d} \quad (3.1b)$$

$$\bar{f}_{n_i}(v_{s_i}) = f_i + f_{i+1} = f_i (1 + e^{-\mu_d \beta_i v_{s_i}}) \quad (3.1c)$$

where μ_d and μ_s are the friction and the stiction coefficients respectively, while v_{r_i} is the relative velocity between the string and the sliding surface. Note that the normalized friction coefficient $\bar{\mu}_{d_i} \rightarrow 0$ if $\beta_i \rightarrow 0$, while $\bar{\mu}_{d_i} \rightarrow 1$ if $\beta_i \rightarrow \infty$. In particular, this latter case means that the system cannot move since the friction is always equal to the tendon

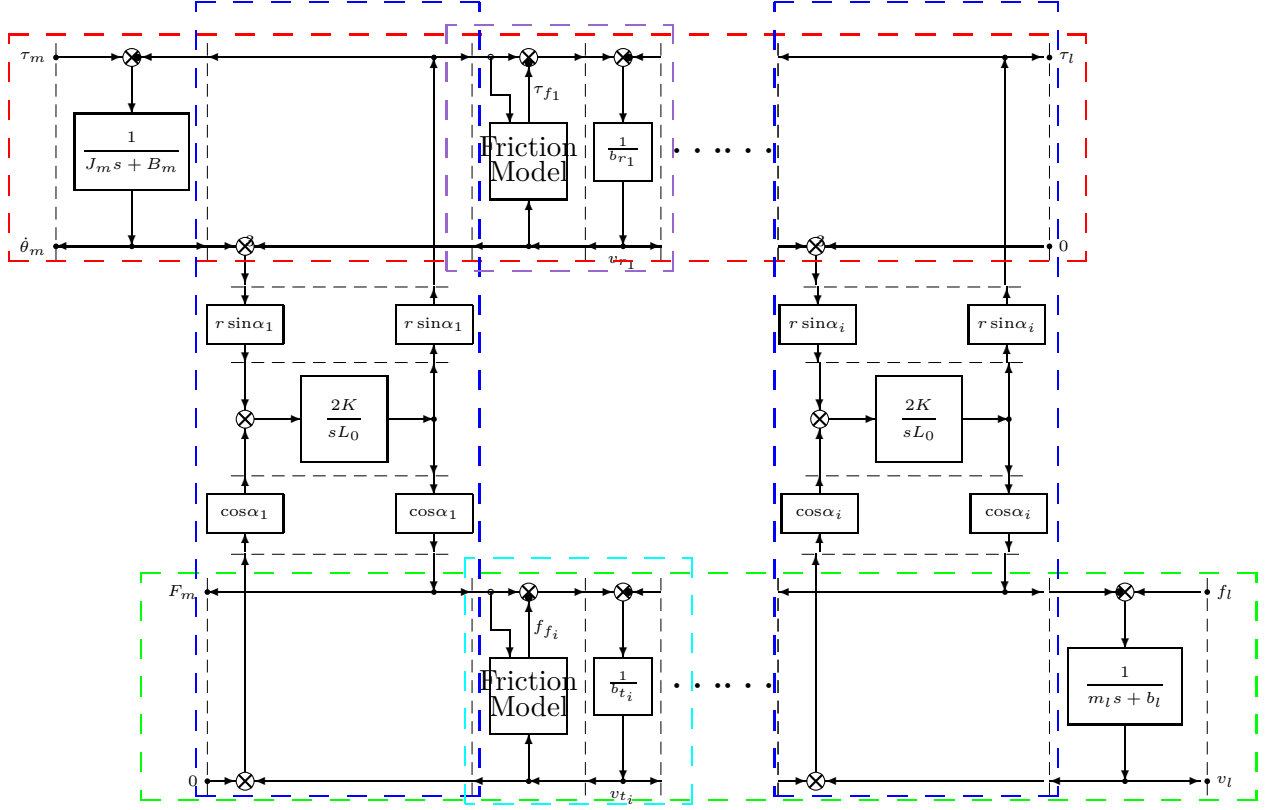


Fig. 3.3 Schematic representation of the dynamic model of the TSA in contact with environmental constraints (s denotes the Laplace variable).

tension. Finally, the friction model used to describe the effects of friction on the i -th sliding surface can be rewritten as:

$$\dot{f}_{s_i}(v_{r_i}) = \sigma \left(v_{r_i} - \frac{f_{s_i}}{f_{n_i} \bar{\mu}_i} |v_{r_i}| \right) \quad (3.2a)$$

$$\bar{\mu}_i(v_{r_i}) = \bar{\mu}_{d_i} + (\bar{\mu}_{s_i} - \bar{\mu}_{d_i}) e^{-\frac{|v_{r_i}|}{\omega}} \quad (3.2b)$$

$$f_{f_i}(v_{r_i}) = f_{s_i} + b_i v_{r_i} \quad (3.2c)$$

where ω is the Stribeck velocity [20] and b_i is the viscous friction coefficient. In these equations, the dependence of the various functions from v_{s_i} has been omitted for brevity.

This approach has been already successfully used for the study of the friction effects in tendon driven robots [19]. It is important to note that the friction model (3.1), (3.2) can be used for computing the friction force acting on both the string translation and the string rotation. So, in case of the friction generated by the string translation, $v_{r_i} = v_i$, where v_i is the string translation velocity, while $v_{r_i} = 2r\dot{\theta}_i$ in case of friction generated by the string rotation. Future work will be devoted to the validation of the model here proposed by means of simulations and comparison with experimental results.

A schematic representation of the joint dynamic model is reported in Figure 3.3. In this scheme, the model has been divided in two main parts, the upper horizontal part modeling the rotation of the motor and of the string (inside the red dashed box), and the lower horizontal part modeling the translation of the string and the load (inside the green dashed box). The friction caused by the contact between the string and the environment partially prevents both the contraction and the propagation of the twisting angle along the string loop. In this model, we suppose the friction acting on the string caused by the contact with the environmental constraints can be split in two separated phenomena: one friction effect acting on the translation part of the string (the “Friction Model” block in the lower part), and a separated friction effect affecting the rotation of the string (the “Friction Model” block in the upper part). Both these friction effects have been modeled as reported in (3.1) and (3.2). It is also assumed that the friction can be concentrated in a single central point for each obstacle, and that the string loop before and after this point can be considered as a chain of ideal TSAs connecting the rotative motor with the obstacles contact points and the load. For this reason, the rotative (upper red box) and the linear (lower green box) part of the model are connected by vertical blocks (inside the blue dashed boxes) representing the geometric relations characterizing the TSAs as described in Sec. 2, (2.1)–(2.13). It is worth noticing that these vertical blocks take also into account the finite stiffness of the string. The TSA

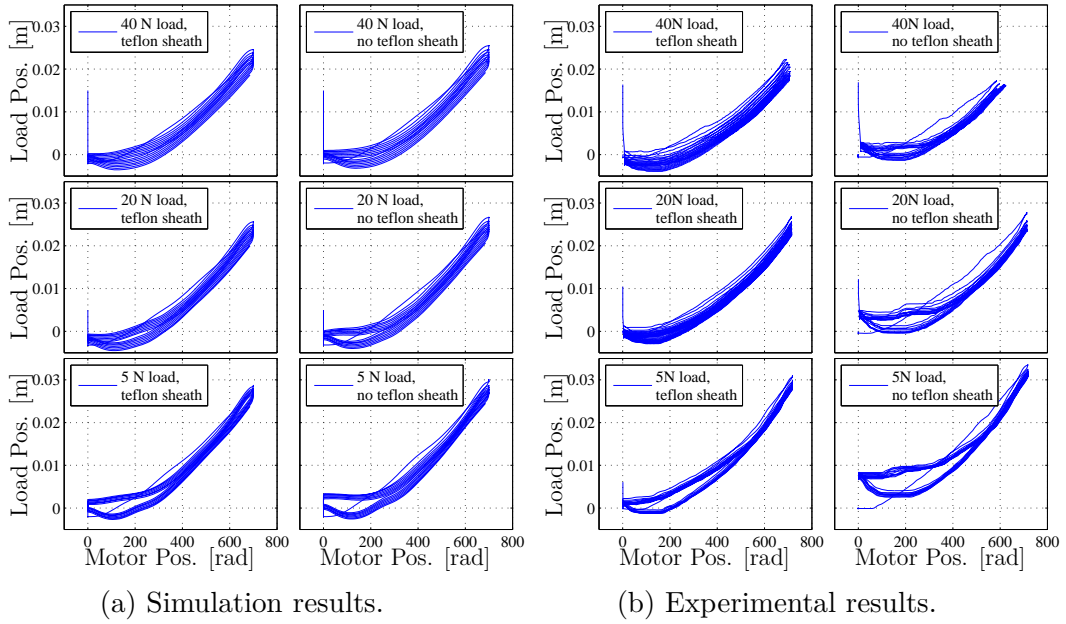


Fig. 3.4 Input output position characteristic with constant load.

sections in which the overall actuation length has been divided are then connected by friction blocks, representing the effects of the obstacle contacts on both the rotation (inside the purple block) and the translation (inside the light blue box) of the TSA. Because of the limited space, the effect of one obstacle only is reported in the scheme, and horizontal dots are inserted to represent the repetition of the previous blocks for modeling the other obstacles. Indeed, all the TSA portions going from an obstacle to the following one can be modeled as reported in the blue boxes, whereas the effect of friction of each obstacle can be modeled as in the purple (for the rotation) and the light blue (for the translation) blocks. The model shown in Figure. 3.3 has been used for simulating the system behavior, the simulation results are described in the next section for a better comparison with the experimental results.

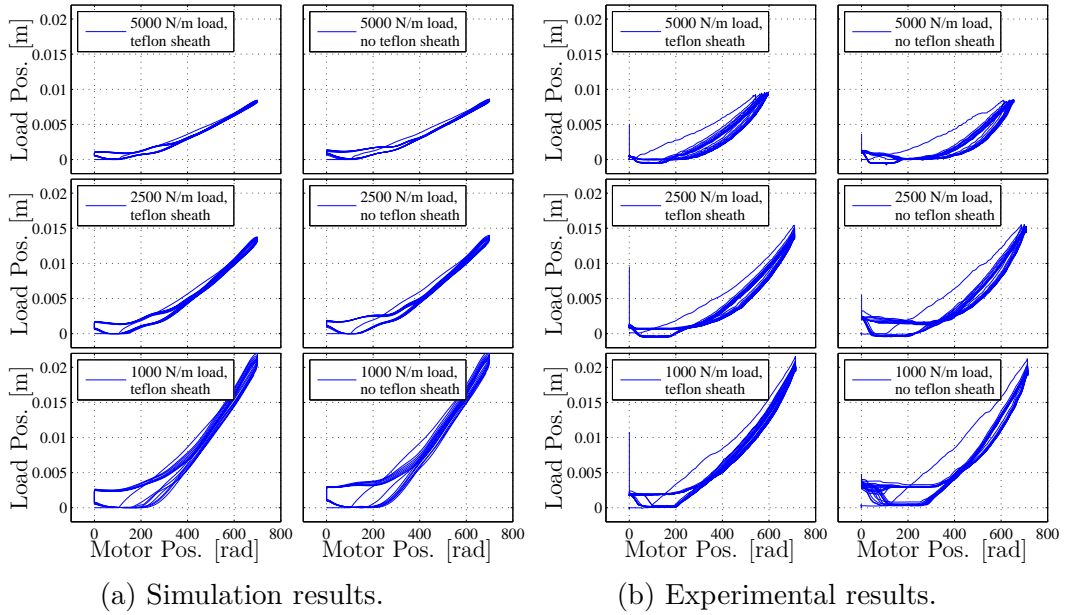


Fig. 3.5 Input output position characteristic with spring-like load.

3.2 Input-Output Characteristic

In this section, the input-output characteristic of the TSA in contact with guiding elements is investigated by means of the experimental setup is depicted in Figure. 3.1. Moreover, aiming at verifying the effects of different material characterized by different surface friction, the experiments here reported have been performed with the TSA directly in contact with the obstacle material (ABS plastic) or guided inside a Teflon tube for reducing the friction coefficient.

The input-output characteristic has been evaluated in two different load conditions. It is worth noticing that the linear motor acting as a load for the TSA is provided with a real time controller making it response very close to an ideal mass-damper system, compensating also for the slider friction [16]. At first, the load is programmed to apply a constant force on the TSA output side, then the rotative motor has been programmed to move from the initial zero position (untwisted string) to a maximum value of 720 rad with trapezoidal trajectory. The simulated input-output position characteristic is reported in

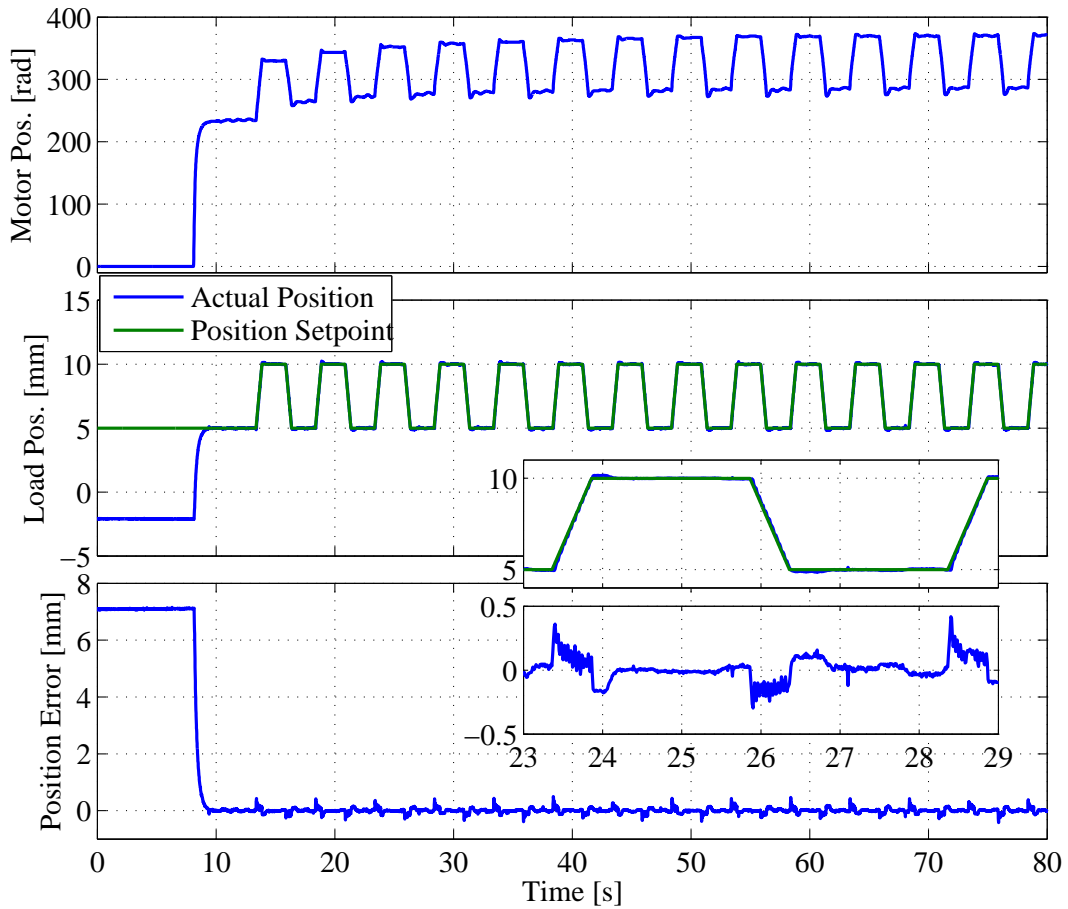


Fig. 3.6 Output load position control with ramp setpoint.

Figure. 3.4a, whereas the experimental one is reported in Figure. 3.4b: in the plots on the right column show the response of the system without the introduction of the Teflon tube, whereas the ones in the left column reports the experiments where the Teflon tube guiding the TSA is introduced. From these plots, different properties of the system can be evaluated: first, by looking at Figure. 3.4b, the plot in lower right corner in which the system is evaluated in the worst conditions from the friction effects point of view, corresponding the case in which the load is applying a constant load of 5 N without the Teflon tube, a large hysteresis cycle between the input and the output position can be clearly seen. Moreover, it can be seen that starting from the zero initial position, the system quickly converge to the aforementioned hysteresis cycle. Now, if the attention is

moved to the upper plots, corresponding to increasing value of the load force (20 N and 40 N respectively), it can be seen that the hysteresis cycle caused by friction reduces as the load increases. This happens because the overall friction effect on the string twisting is less evident for large string tension. On the other hand, increasing the load, the overall system response takes longer to reach the final hysteresis cycle, this phenomenon can be ascribed to the slower propagation of the string twist angle from the contact point closer to the rotative motor to the one near the load. It can be also noted that for the larger load (40 N) the motor torque is not sufficient to reach the desired angular position (700 rad) because of the high friction caused by the load. Another important point to note is that, by comparing the plots on the right and in the left column, the introduction of the Teflon tube significantly reduce the effect of friction. Indeed, the hysteresis decreases in case the Teflon tube is present, fact that suggest the reduced friction coefficient reduces the system hysteresis as expected. It is also worth noticing that the convergence of the TSA to the steady state behavior seems slower in all the load conditions when the Teflon tube is introduced. From the simulation results reported in Figure. 3.4a, it can be seen how the developed model is able to qualitative reproduce the most evident effects observed during the experiments, like the asymmetric hysteresis and the load dependent input-output relations.

A second experiment set has been performed with a different behavior of the load. In this case, the load is programmed to act as a spring. From the experimental results reported in Figure. 3.5b, where the system input-output characteristic has been evaluated with a load stiffness of 1000, 2500 and 5000 N/m respectively, also in this case with and without the Teflon sheath covering the TSA, it can be seen that the main response characteristics highlighted in the previous case are preserved, even if the hysteresis cycle results more evident in all the plots. Moreover, in these plots it is also possible to see that a quite evident height-shaped hysteresis cycle emerges. This can be ascribed to

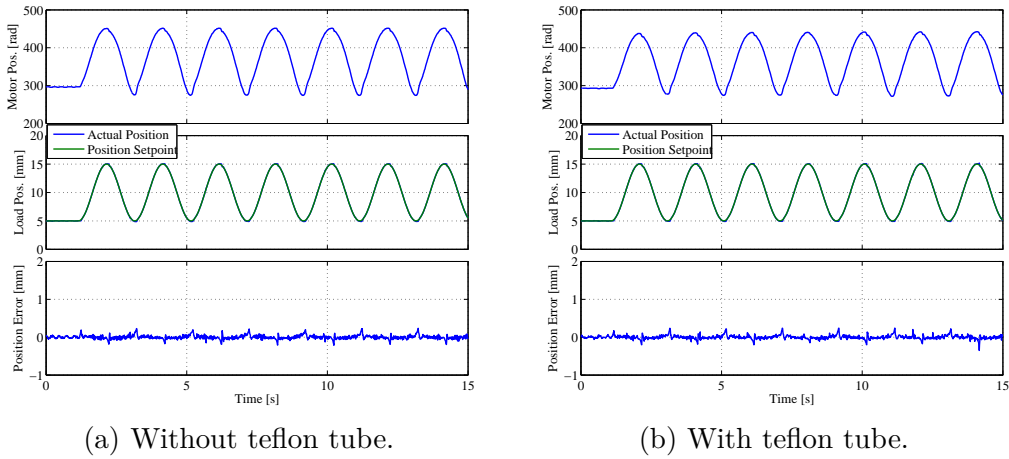


Fig. 3.7 Output load position control with 0.5Hz sinusoidal setpoint.

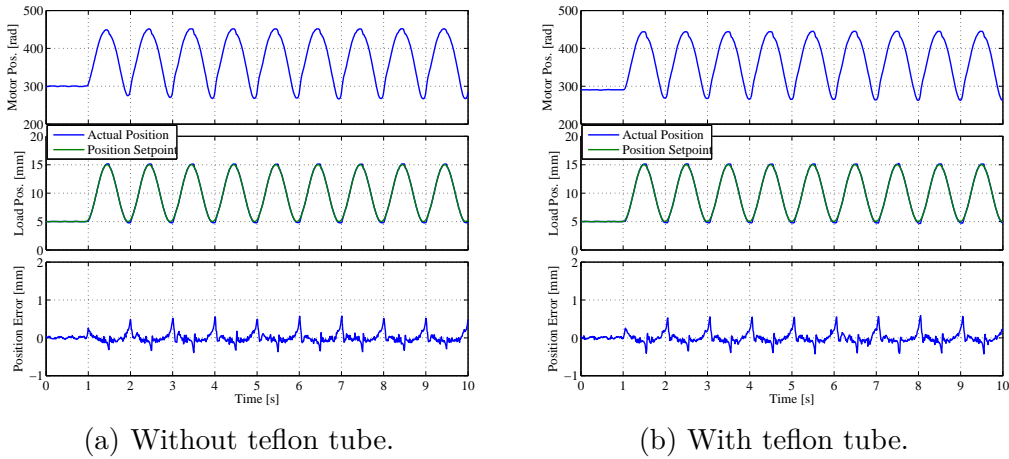


Fig. 3.8 Output load position control with 1Hz sinusoidal setpoint.

the different load behavior, i.e. the spring-like load response causes the load to decrease for lower string twisting angle, fact that make the friction more evident in the initial motion region (the region closer to the zero coordinates) and cause the twisting angle to propagate faster during the release phase because of the decreasing load. Also in this case, from the simulation results reported in Figure. 3.5a, it can be seen how the developed model is able to qualitative reproduce the most evident effects observed during the experiments, like the height-shaped hysteresis and the large direction-dependent dead-zone close to the lower left corner in the plots, especially for low value of the load stiffness.

3.3 Output Feedback Control

In this section, the control of the load position by means of the TSA in contact with sliding surfaces, as depicted in Figure. 3.1, assuming that the system output (i.e. the load position itself) can be measured is taken into account. In the experimental setup, the load position can be measured by means of the linear motor integrated encoder, and a digital PID controller is adopted because of its implementation and tuning simplicity for the preliminary evaluation of the control performance.

In Figure. 3.6, the response of the system starting from untwisted conditions (i.e. $\theta = 0$) is reported. The load is programmed to apply a constant force of 10 N, and the initial load position is -2 mm (because of the initial load force). The TSA is required to apply a load position setpoint composed by a trapezoidal trajectory from 5 mm to 10 mm, with a ramp duration of 0.5 s in both the positive and the negative direction. The upper plot in Figure. 3.6 shows the string twisting angle, whereas the middle plot reports the actual load position and the position setpoint. The load position error is reported in the lower plot. From these plots, it can be seen that the control system rapidly reaches the desired output position after the control activation at time $t = 8$ s, and that the setpoint tracking of the trapezoidal trajectory is quite good. It is worth noticing from the upper plot reporting the string twisting angle that, when the trapezoidal trajectory starts, the rotative motor position present a transitory to the steady-state response. This phenomenon is due to the friction preventing the twisting angle to propagate immediately from the input to the output, while the forward and backward motion of both the rotative and the linear motor allows the system to reach the steady state behavior after approximately 4 cycles of the trapezoidal trajectory.

Further experiments have been carried out to evaluate the system response. In the experiment reported in Figure. 3.10 the PID controller shows a fast step response and

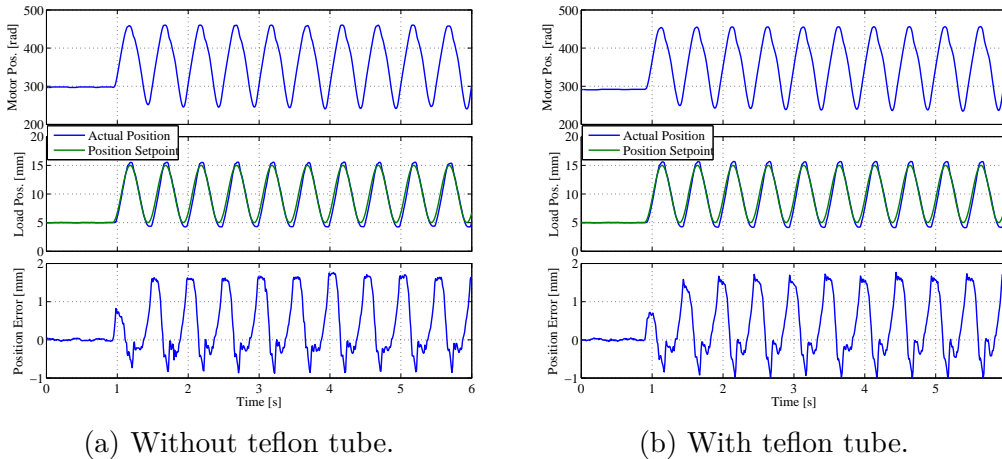


Fig. 3.9 Output load position control with 2Hz sinusoidal setpoint.

the steady-state error is almost zero thanks to the introduction of the integral action in the controller. It is possible to see from Figure. 3.10 that the load position shows a small overshoot to the step setpoint, moreover the overshoot is not symmetric because of the non-linearity of the TSA transmission characteristic. For evaluating the system bandwidth, the response to sinusoidal setpoints with different frequency has been verified. In Figure. 3.7 a 0.5 Hz sinusoidal setpoint has been applied: the lower plot, reporting the tracking error, shows that the PID controller is able to track this setpoint compensating for the effect of friction both in the case the teflon tube is present or not. Increasing the setpoint frequency, the tracking error rapidly increases, as reported in Figure. 3.8 and Figure. 3.9 where the response to a 1 Hz sinusoid and a 2 Hz sinusoid are reported respectively, denoting the bandwidth of the system at around 2 Hz. A more precise identification of the system bandwidth will be object of future research.

3.4 Conclusions

In this chapter, an investigation on the behavior of this actuation principle in the case the string is in contact with obstacles or constraints guiding the string itself is investigated.

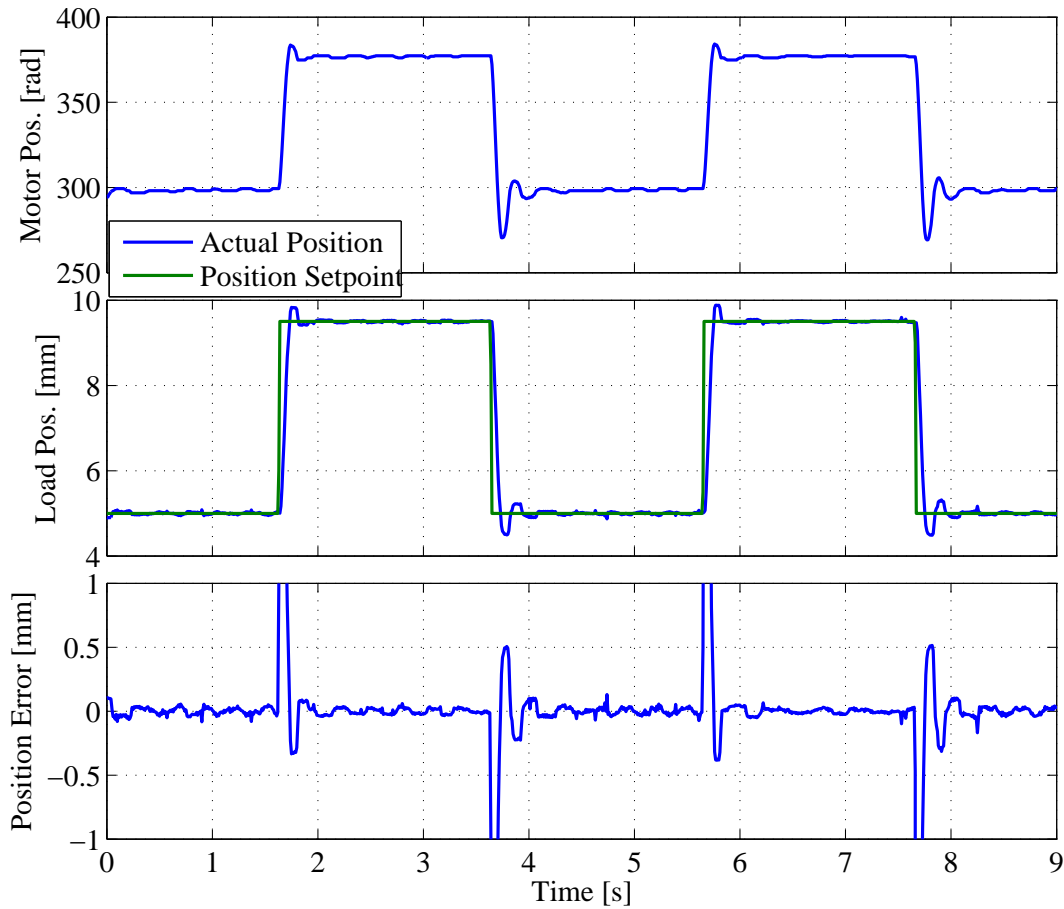


Fig. 3.10 Output load position control with step setpoint.

With respect to the conventional TSA working conditions where the string is straight and no contact is present along the string, this solution opens the scenario to a wider TSA application, reducing the design constraints and enabling more compact actuation system implementations. In the analysis here reported, the TSA has been evaluated with different loading conditions and including a Teflon tube covering the twisted string for reducing the surface friction. An experimental setup for the evaluation of the TSA characteristics has been developed, and the characterization of the input-output position system response has been carried out. The comparison between simulation and experimental results shows that the developed model is able to reproduce the main effects observed in the system experimental response. Finally, a PID regulator for controlling

the load position has been introduced and experimentally evaluated, showing the possibility of compensating the effect of friction introduced along the string by means a simple and standard controller. Future activities will be devoted to further characterizing the behavior of the system, to a better identification of the system parameters and to the evaluation of different control strategies on the experimental setup presented in this chapter.

Chapter 4

A Variable Stiffness Joint Based on TSA System

A relevant research interested all over the world is devoted to the implementation of Variable Stiffness Joints (VSJs) [21] because they allow to solve several safety issues related to the interaction of robots with unknown environments and humans. Many different VSJ implementations can be found in literature, the most noticeable are the VSA-II [22], where the variable stiffness is obtained by coupling two electric motors to the joint through a belt and a pretensioning system, the DLR VS-Joint [23] where the circular spline of the harmonic drive is connected to the joint frame by a modulated spring, the IIT Pneumatic Joint [24] actuated by McKibben motors, the AwAS-II [25] based on the moving pivot concept and the Energy-Efficient Variable Stiffness Actuators [26] developed by the Twente University. Recently, Vanderborght et al. published a review of different VSJ implementations [27].

The TSA is used for the implementation of a Variable Stiffness Joints. The system is composed by a couple of TSA in antagonistic configuration connected to a rotating link,

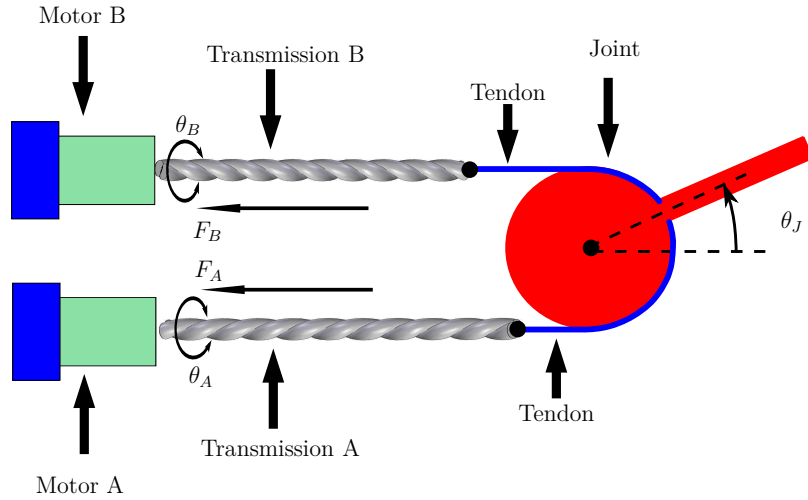


Fig. 4.1 Schematic representation of the rotative joint with two twisted string transmission systems.

as shown is the scheme reported in Fig. 4.1. The intrinsic non-linearity and configuration-dependent stiffness of the TSA [9] is exploited for this purposes. The design of a VSJ and its dynamic model has been described.

4.1 Dynamic Model of The Variable Stiffness Joint

The structure of the considered VSJ is illustrated schematically in Fig. 4.1: two TSAs are connected in antagonistic configuration to the rotating link on one end and to the DC motors on other end respectively. The connection between the TSA and the link is implemented by a pulley driven by tendons, the tendons are then connected to the TSAs by linear guides to avoid the twist of the tendon itself.

In this implementation, conventional DC motors are used to drive the TSAs. Since the electric dynamics is usually very fast in comparison to the other effects and then it can be neglected, a simplified dynamic model for the DC motors is assumed. Taking into account the symmetry of the actuation system, in the following we will distinguish

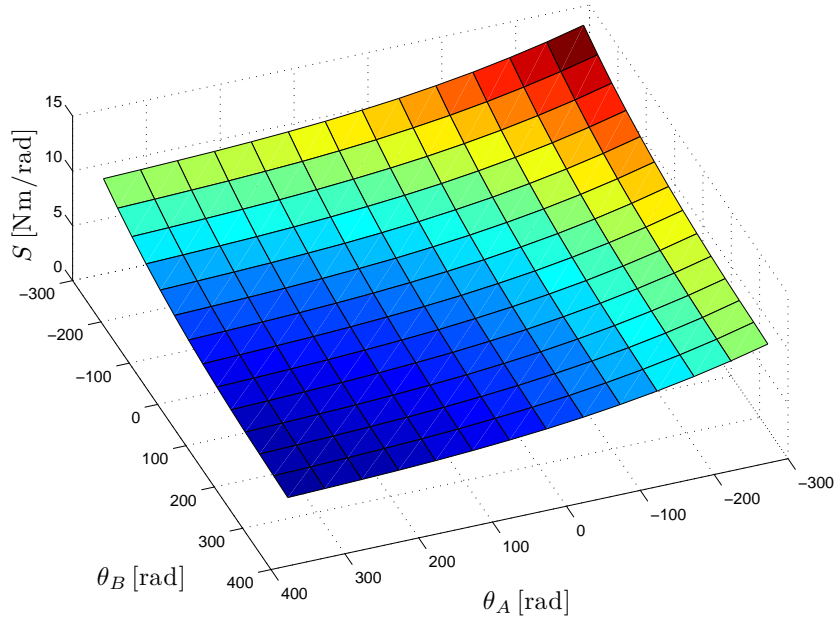


Fig. 4.2 Stiffness of the link versus motor positions, no external load is assumed.

the two actuators by using the subscript A and B respectively. Moreover, the length of the transmission in the zero joint position is called p_0 , and the maximum transmission length is limited by the controller to limit the joint motion range into the interval $[-60, 60]$ deg. Assuming a certain minimum tension force of the TSA and considering inextensible tendons for the connection with the joint, it follows from the scheme in Fig. 4.1 that the length of the two TSAs p_A and p_B can be computed as:

$$p_A = p_0 - r_j \theta_j \quad (4.1)$$

$$p_B = p_0 + r_j \theta_j \quad (4.2)$$

where θ_j and r_j are the link rotation angle and the link pulley radius. Finally, the link dynamics can be modeled considering the equilibrium of the forces exerted by the two TSAs on the link pulley. It results that the complete joint dynamic model can be written

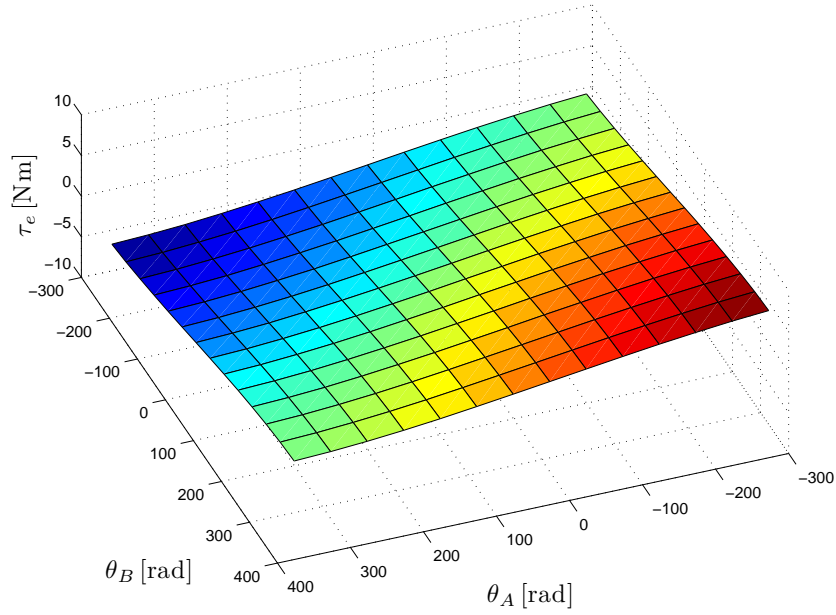


Fig. 4.3 Admissible external torque across possible motor positions.

as:

$$J_m \ddot{\theta}_{mA} + B_m \dot{\theta}_{mA} + \tau_{LA} = \tau_A \quad (4.3)$$

$$J_m \ddot{\theta}_{mB} + B_m \dot{\theta}_{mB} + \tau_{LB} = \tau_B \quad (4.4)$$

$$J_j \ddot{\theta}_j = r_j [F_{LA} - F_{LB}] + \tau_e \quad (4.5)$$

where

$$\tau_{L\{A,B\}} = \tau_L \left(\theta_{m\{A,B\}}, p_{\{A,B\}} \right) \quad (4.6)$$

$$F_{L\{A,B\}} = F_L \left(\theta_{m\{A,B\}}, p_{\{A,B\}} \right), \quad (4.7)$$

$\theta_{m\{A,B\}}$ and $\tau_{\{A,B\}}$ are the motor position and the (commanded) input torque of the DC motors A and B respectively, J_m and B_m the rotor inertia and the viscous friction of the DC motors, J_j and τ_e are the link inertia and the external load torque applied to the joint respectively. Then, the eqs. (4.3) and (4.4) describe the motor A and B dynamics respectively and eq. (4.5) represents the link dynamics. Note that the viscous friction acting on the joint is neglected because of its very small value.

The link stiffness S_j can be defined as the partial derivative of the external torque τ_e with respect to the link position θ_j in static conditions, i.e. when θ_j and $\theta_{m\{A,B\}}$ are constant. Then, considering eqs. (2.14) and (4.5), it results:

$$\begin{aligned} S_j &= \frac{\partial \tau_e}{\partial \theta_j} = -r_j \left[\frac{\partial F_{LA}}{\partial \theta_j} - \frac{\partial F_{LB}}{\partial \theta_j} \right] = r_j^2 [S_A + S_B] \\ &= \frac{4k}{L_0} - \frac{2kr^2\theta_A^2}{(p_A^2 + r^2\theta_A^2)^{3/2}} - \frac{2kr^2\theta_B^2}{(p_B^2 + r^2\theta_B^2)^{3/2}} \end{aligned} \quad (4.8)$$

$$S_{\{A,B\}} = S(\theta_{\{A,B\}}, p_{\{A,B\}}) \quad (4.9)$$

It is clear from that equation that the joint stiffness varies with its position θ_j and the motor angles $\theta_{m\{A,B\}}$. Figure 4.2 illustrates the stiffness characteristic of the joint over the admissible range of motor positions. In this plot, the joint is in static conditions, i.e. no external torque is applied to the joint. In Fig. 4.3 the admissible external torque the joint can support over the admissible range of motor position is reported. From these plots, it is possible to see that the joint stiffness can be adjusted independently from the external torque since their variation direction wrt the motor coordinates are almost orthogonal.

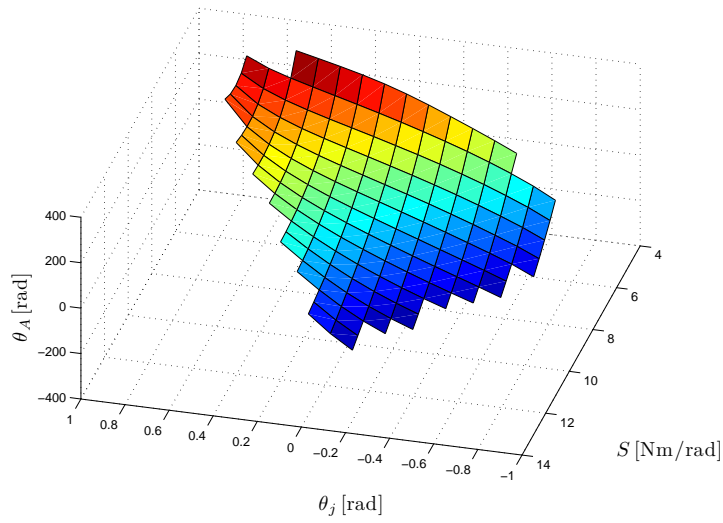
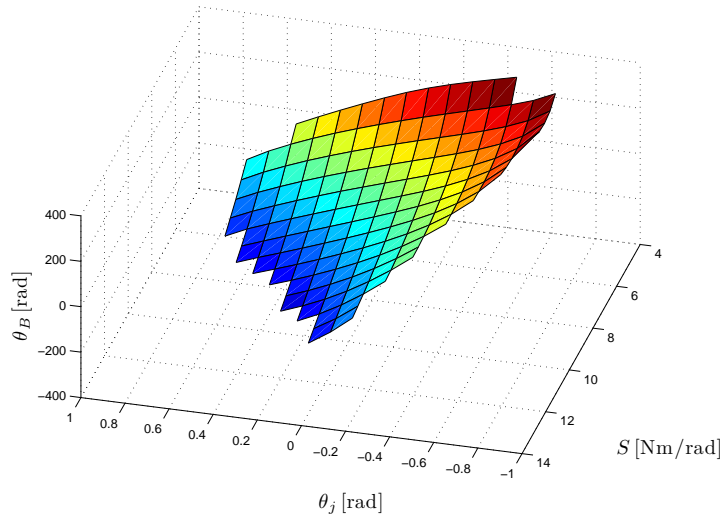
(a) Reference position for Motor A .(b) Reference position for Motor B .

Fig. 4.4 Position of the motor A (top) and B (bottom) over the joint stiffness and position variation range.

4.2 Control Algorithms

In the following, a simple control algorithm is based on the inversion of the static equations describing the system behavior and on standard PID motor position controllers is described and evaluated. In these experiment, the joint stiffness is measured from the joint and motors positions according to eq. (4.8).

The inversion of the system equations consists in finding the desired motor positions $\theta_{\{A,B\}d}$ given the desired joint position θ_{jd} and stiffness S_{jd} according to eqs. (4.5) and (4.8) assuming that the external torque τ_e is measurable and the joint is in static conditions (i.e. $\dot{\theta}_j = 0, \ddot{\theta}_j = 0$). To this end, the resulting transmission lengths $p_{A,B}$ are computed from eqs. (4.1) and (4.2) given the desired joint position θ_{jd} . Then, substituting $p_{A,B}$ into eqs. (4.5) and (4.8), these equations should be inverted to obtain a couple of equation providing the desired motor positions. Unfortunately, the closed form inversion of eqs. (4.5) and (4.8) is not directly possible since it will result in an implicit function. To solve this problem and to allow an easy realtime computation of the desired motor positions, the term of the type $1/\sqrt{p^2 + r^2\theta^2}$ in eq. (2.13) is fitted with a 2D polynomial interpolation of proper order over the desired range of p and θ using a SVD decomposition. This technique has the advantage of producing a least-squares best fit of the data even if those are overspecified or underspecified.

Considering also that, computationally speaking, computing the solutions of a polynomial of order higher than 3 could be quite expensive, a 3rd-order polynomial interpolation is selected for our purposes as a good trade-off between computational complexity and error. This approach allows an easy computation of the motor positions given the desired joint position and stiffness, even in a realtime system. Fig. 4.4a and Fig. 4.4b show the computed reference motor position over the range of admissible joint position and stiffness.

4.3 System Design

A picture of the experimental setup for the verification of the VSJ characteristics and the evaluation of the controller described in this chapter is shown in Fig. 4.5. The link is partly made in ABS plastic using rapid prototyping to reduce the mass, inertia and cost

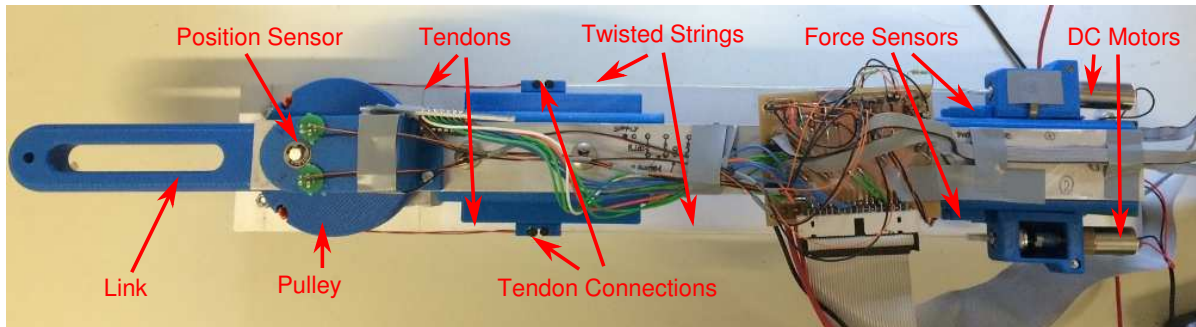


Fig. 4.5 Top view of the experimental setup.

and it is equipped with an optical position sensor [28] able to detect the absolute joint position over a range of motion of ± 60 deg. The joint is connected to the two antagonistic TSAs by means of tendons and linear guides to prevent the twisting of the tendon itself. Two identical DC motors are used to drive the TSAs. Each motor is equipped with an incremental encoder and an optical force sensor [17, 18] for the measurement of the actuation force. Moreover, also the motor power electronics is integrated into the motor module. This sensor equipment allows to measure both the joint and the motor positions, moreover the joint and motor velocities are computed using numerical filtering techniques [29]. On the other hand, the transmission force sensor can be exploited for the online estimation of the joint stiffness [30].

4.4 Actuation Module

Fig. 4.6 show a detailed view of the actuation module [18]. A plastic ABS frame manufactured by 3D rapid prototyping composes the mechanical structure along with a pair of axial-symmetric compliant beams. These beams function as a linear spring granting a certain compliance to the structure as well as the implementation of the force sensor. A DC motor is located in this module along with an optical encoder for position sensing while the output shaft is supported by an axial bearing at the point of the twisted string

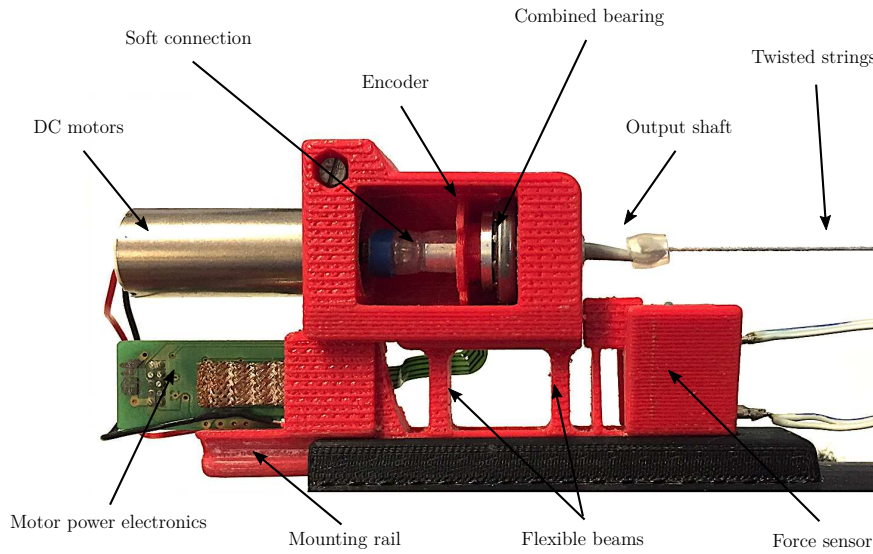


Fig. 4.6 Detail of the actuation module.

connection. A silicon tube is used to join the motor and transmission shafts to provide ample flexibility in order to solve problems regarding misalignment of the rotational axes of the motor and the transmission shaft. The particular structure of the motor module consents the transmission force to be completely supported by the output shaft through a combined bearing while the motor is only used to transmit the necessary torque for driving the twisted string actuation to the output shaft.

The integration of a force sensor into the actuation module is necessary to successfully measure the force which the actuators apply directly to the load [17]. Placing the force sensor between the frame connection point on the robot structure and the actuation module is one of the possible proposed solutions. In this setup, all of the components of the actuation system are integrated, thus optimizing encumbrance. A digital interface to input and output signals required for the actuation system control can be provided by the placement of the actuator electronics, including both the motor power electronics and the conditioning system for both the optical encoder and the force sensor, in a single printed circuit board.

4.5 System Identification

Several experiments are executed for verifying the stiffness variation of the developed VSJ by applying a deviation of 10 deg from the resting position to the link and then suddenly releasing it. The motion of the joint is recorded and the data are used for the identification of the joint stiffness and damping, assuming that the link inertia is known (it has been computed from the CAD files), that the stiffness and damping are constant over the joint motion range considered for the experiment, neglecting static friction because of its very low value and assuming that the joint behaves as a second-order linear dynamic system with transfer function expressed by:

$$\frac{\theta_j(s)}{\tau_e(s)} = K \frac{\omega_n^2}{s^2 + 2\delta\omega_n s + \omega_n^2} \quad (4.10)$$

where K , ω_n , δ and s are the gain factor, the natural frequency, the damping factor and the Laplace variable respectively. For identification purposes, the joint dynamics is redefined as:

$$J_j \ddot{\theta}_j + b_j(\theta_A, \theta_B) \dot{\theta}_j + k_j(\theta_A, \theta_B) \theta_j = \tau_e \quad (4.11)$$

where the dependence of the damping $b_j(\theta_A, \theta_B)$ and the stiffness $k_j(\theta_A, \theta_B)$ coefficients from the motor configuration (θ_A, θ_B) represents the damping and the stiffness variability of the joint. By moving eq. (4.11) to the Laplace domain it follows:

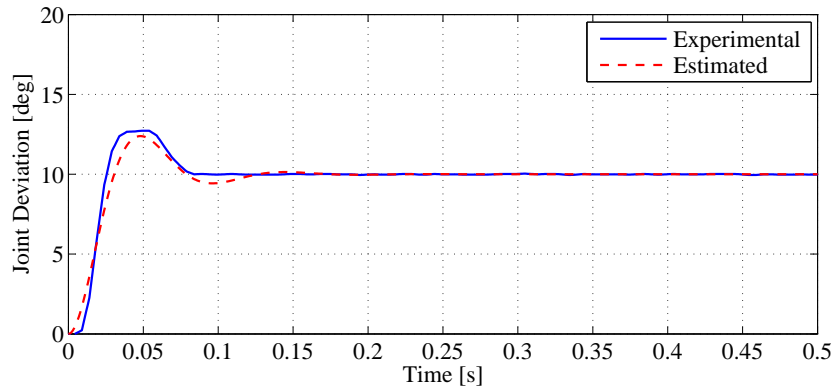
$$\frac{\theta_j(s)}{\tau_e(s)} = \frac{1/J_j}{s^2 + s b_j(\theta_A, \theta_B)/J_j + k_j(\theta_A, \theta_B)/J_j} \quad (4.12)$$

Then, by matching the coefficients of eq. (4.10) and (4.12) it results:

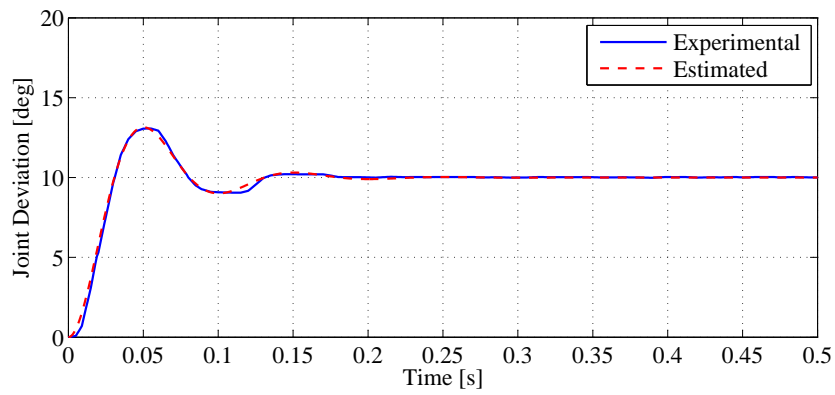
$$k_j = J_j \omega_n^2, \quad b_j = 2J_j \delta \omega_n, \quad K = 1/k_j \quad (4.13)$$

where the dependance from (θ_A, θ_B) is omitted for brevity. In particular, the parameters δ and ω_n can be easily identified by looking at the response of the system to a proper input function, e.g. a step input. In our experiments, the step input is reproduced by imposing to the joint the necessary external torque to deviate it of 10 deg from the zero position (to compare the joint motion over the same range, the external torque is not measured) and then releasing the joint. We assume in this way that the input torque goes from its initial value to zero instantaneously. The results of four tests executed with different desired joint stiffness are shown in Figure. 4.7: the blue line represents the experimental response while the red dashed line represent the response of the second-order linear dynamic system reported in eq. (4.10) with the parameters identified from the experimental response. These plots show that the real system behavior is well approximated by eq. (4.10) within the considered motion range. The damping and stiffness parameters identified from these experiments and the commanded joint stiffness k_j^* are reported in Tab. 4.1. The experiments are numbered from 1 to 4. From these results, it is possible to conclude also that a significant damping variation is induced in the system by the variation of the transmission configuration, the investigation on this aspect is out of the scope of this chapter and will be subject of future research.

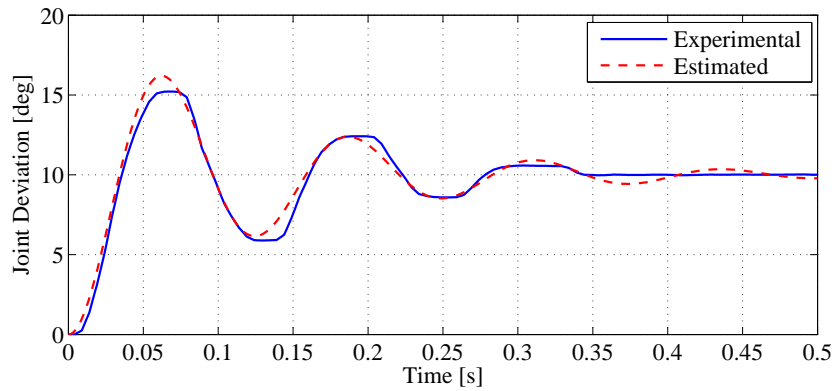
After the verification of the joint stiffness variability, the response of the whole system under the control of standard PID motor position controllers is evaluated in dynamic conditions. This control approach is selected because it is particularly simple and because it does not require sensor feedback from the joint, fact that may introduce stability



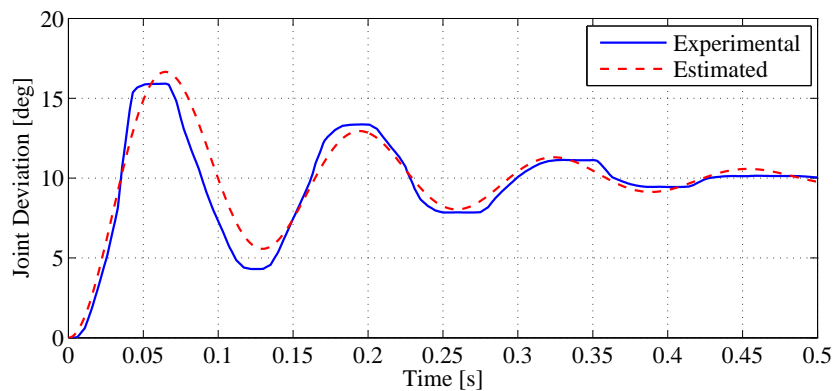
(a) Experiment 1.



(b) Experiment 2.

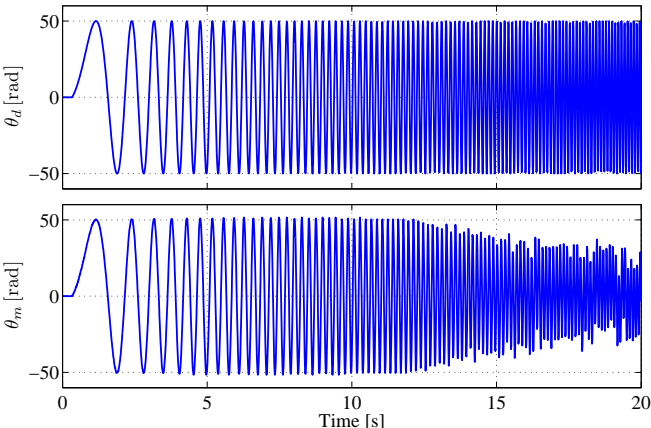


(c) Experiment 3.

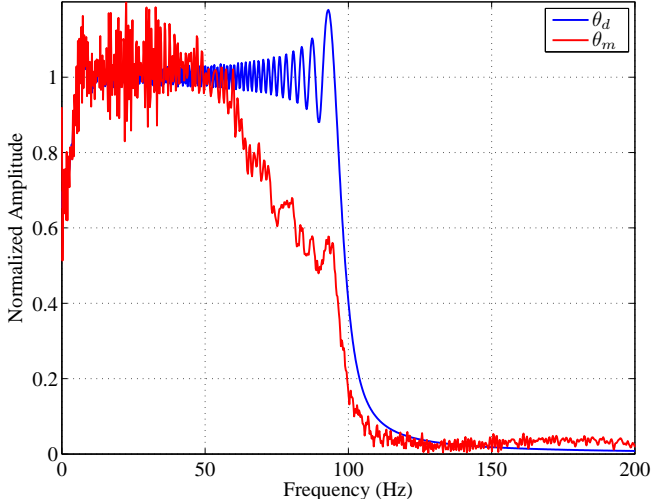


(d) Experiment 4.

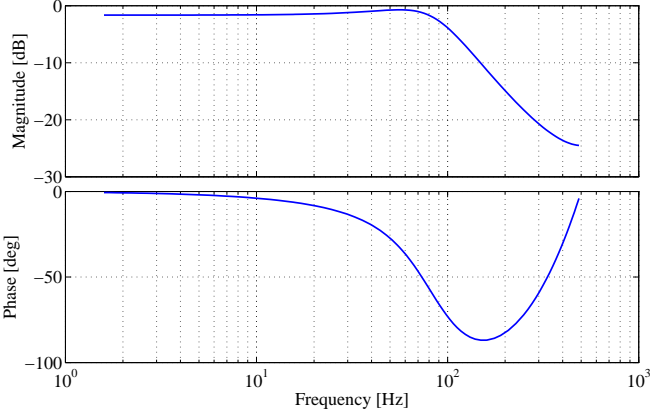
Fig. 4.7 Identification of the joint characteristics.



(a) [Motor response to the [0.1 20] Hz sweep signal.



(b) Reference signal spectrum and of the motor response.



(c) Bode plot of the motor response.

Fig. 4.8 Identification of the motor response.

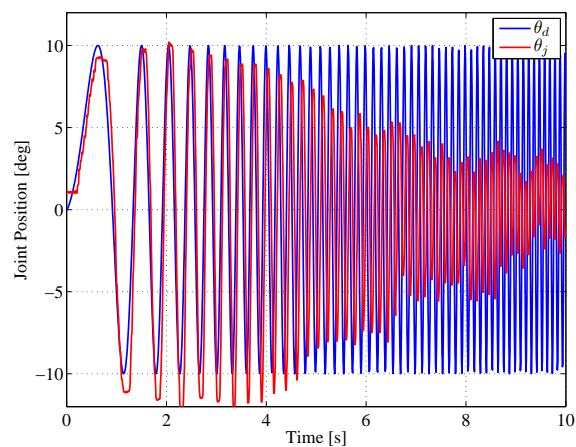
Symbol	Unit	Exp. 1	Exp. 2	Exp. 3	Exp. 4
J_j	kg m ²	2.44 E-3	2.44 E-3	2.44 E-3	2.44 E-3
k_j^*	N m	13	10	7	5
k_j	N m	12.57	10.88	6.37	5.83
b_j	N m s ⁻¹	0.15	0.11	0.04	0.03

Table 4.1 Identified joint response parameters.

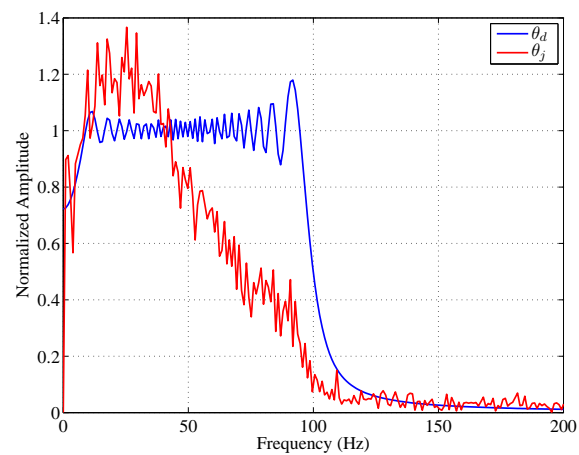
issues due to the limited joint stiffness. On the other hand, this control approach is based on the perfect knowledge of the system model and parameters, fact that may introduce significant errors when applied to the real system. To reduce these side effects, an accurate identification of the system parameters and the verification of the models need to be performed.

First, the motor response is evaluated, as can be seen in the plots reported in Figure. 4.8. To verify both the accuracy and the bandwidth of the motor position controllers, a sweep signal with amplitude 50 rad and frequency ranging from 0.1 to 20 Hz is used as a setpoint for the motor position controllers. The top plot in Figure. 4.8a shows the motor position setpoint of one of the two motors, whereas the bottom plot reports the motor effective position. From this plots it possible to see that the motor follows quite precisely the position setpoint at least within a certain frequency range. For an easier evaluation of the motor position control bandwidth, the FFT analysis of the motor setpoint and actual position is shown in Fig. 4.8b: this plot confirms that the motor controller accurately regulates the motor position within a frequency range up to 60 Hz. After this frequency, the amplitude of the motor output position rapidly decreases. Moreover, looking at the motor position Bode plot reported in Figure. 4.8c, it possible to see that the motor position controller behaves like a second order low-pass filter with cut-off frequency of about 90 Hz.

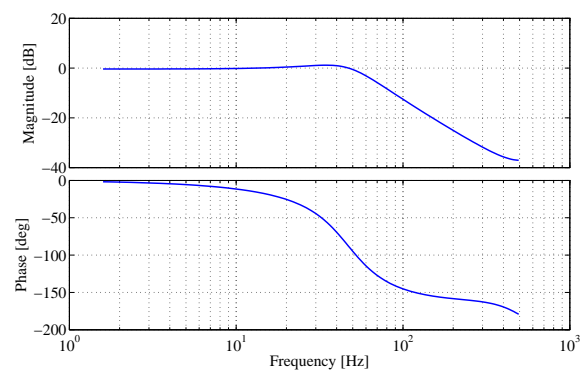
After the evaluation of the motor response, the response of the VSJ is tested. Also in this case, a sweep signal is used as joint position setpoint, but the amplitude is reduced



(a) Joint response to the [0.1 20] Hz sweep signal.



(b) Reference signal spectrum and of the joint response.



(c) Bode plot of the joint response.

Fig. 4.9 Identification of the joint response.

to 10 deg while the frequency ranges from 0.1 to 20 Hz, as in the previous case. In Fig. 4.9a the joint position setpoint and the actual joint position are reported in blue and red respectively. Since the controller is based on the inversion of the model static equations and on PID motor position controllers, a certain deviation of the joint position from the desired one can be expected, as shown in Fig. 4.9a. Anyway, the tracking of the desired joint position is quite good at least within a frequency range up to 40 Hz, as can be seen from Figure. 4.9b reporting the FFT of both the joint position setpoint and actual position. In Figure. 4.9c the Bode plot of the joint response is shown: from this plot it is possible to see that, also in this case, the joint behaves as a second order low-pass filter with a cut-off frequency of about 48 Hz. It is important to point out that the frequency response of the joint changes with the commanded joint stiffness. Indeed, the experiment here reported corresponds to the case in which the commanded stiffness is the same adopted in the experiment 1 shown in Fig. 4.7a, see also Tab. 4.1. In particular, it can be easily verified that the frequency response of the system reported in eq. (4.10) with the parameters reported in Tab. 4.1 for the first experiment match the one reported in Fig. 4.9c. The same can be verified also for the other value of the joint stiffness obtained during the other experiments, but the results are not here reported for brevity.

4.6 Conclusions

In this chapter, the use of this actuation principle for the implementation of a VSJ by using two actuators in antagonistic configuration is investigated by deriving the dynamic model of the system. An experimental setup for the evaluation of the VSJ characteristics is developed. An experimental setup for the evaluation of the VSJ characteristics is developed, and the identification of the main system parameters is carried out. A

simple controller based on the inversion of the device static model is introduced and experimentally evaluated. Future activities will be devoted to the experimental evaluation of different control strategies on the experimental setup presented in this chapter.

Chapter 5

Force Sensor

Nowadays, advanced robotic systems are conceived for dealing with unstructured environments, therefore the physical interaction and their coexistence with humans plays a crucial role. With respect to their precursors, these robots are provided with enhanced cognitive capabilities, making them able to adapt to dynamically changing conditions. A number of innovative features are required to achieve this goal, among them the physical interaction with the environment and human-robot interaction are enabled by the availability of the interaction forces measurement. Force and torque sensors are of primary importance also in the developments of wearable and assistive robotic devices, such as servo-actuated prostheses and exoskeletons, in which physical human-robot interaction is of paramount importance, providing proper information for detecting the human intentions. These devices cover a wide application set, ranging from rehabilitation and human assistance to military tasks and haptic operations. In last few years, the applications of exoskeletons to support the hand and lower/upper-limb mobility have significantly grown [31, 32].

Several uniaxial force sensor and multi-axis force/torque sensors are available on the market, and almost all of them are based on strain gauges, consisting on both thin-film

resistors or semiconductors. Conventional strain-gauge based force sensors measure the strain induced on the mechanical structure by the external force. The main advantage of these sensing elements are mainly the extremely good linearity, at the expense of quite complex electronics for the signal acquisition, sensitivity to electromagnetic noise and temperature variations. Moreover, strain gauges require properly designed supporting structures that can pose some difficulty during their integration into complex mechanical systems like robots. Another critical point with that sensing technology is that the strain gauge assembly procedure is a quite complex and error-prone task, requiring significant experience and careful implementation. This results in significant limitations of the design customization, fact that brings robot designers to rely very often on commercial non-application-optimized products.

Several advantages in the field of force measurement can be introduced by alternative sensing solutions. One alternative is provided by force sensors based on piezoelectric sensing elements, as proposed in [33]. Another promising solution relies on the use of optoelectronic components as sensing elements for the implementation of force sensors, as already proposed in literature by several authors [34–37]. These kind of sensors exploit the scattering and/or the reflection of a light beam emitted by a source and received by suitable detectors to detect the deformation of a compliant structure or the relative displacement between elastically coupled elements caused by the external force. In [36], a force sensor based on the use of discrete optoelectronic components for the measurements of the robotic hand tendon force at the actuator side is presented for force control and friction compensation purposes [38]. In [39], an optical micrometric force sensor based on the differential measures of the light intensity is presented, while [40] presents a sensor based on changing coupling of optical power between a photodiode and a vertical-cavity surface-emitting laser facing each other and separated by a deformable transducer layer. In [34] the authors adopt optoelectronic devices mounted on a compliant structure to

measure human-robot interaction forces. Hirose and Yoneda implemented an optical 6-axis F/T sensor adopting a 2-axis photosensor for measuring the deformation caused by the external load on a compliant structure [41]. Other optoelectronic devices such as fiber bragg gratings have been exploited for the implementation of force tactile sensors [42]. An optoelectronic force sensor based on CCD or CMOS camera to acquire the deformation of a surface caused by external force is presented in [43]. In [44] and [45] the light beam of a Light Emitting Diode (LED) is scattered by a silicon dome and a urethane foam cavity respectively: the compression of the dome or the cavity due to applying an external force, causes a scattered energy density variation that is detected by several PhotoDetectors (PDs). In [46] an optical tactile sensors based on a matrix of LED/PD couples covered by a deformable elastic layer is reported. In [47] an example of tactile/force sensor exploiting the reflection of the light cone emitted by an LED on a silicon rubber dome is reported. In [48] another alternative solution has been proposed by a fiber optic force sensor using Fabry-Perot Interferometry that is compatible in the high-field Magnetic resonance imaging (MRI). In [49] machine learning techniques are investigated to dynamically compensate for environmental biases affecting multi-axis optoelectronic force sensors, such temperature and ambient light.

This chapter reports an innovative solution for the implementation of an optoelectronic force sensors for robotic applications. The basic sensor elements are a compliant frame, manufactured in ABS plastic by 3D printing or in DELRIN[®] by CNC milling, and a commercial optoelectronic component, a light fork embedding in a compact and high-sensitive device both the LED and the PD required for measuring the compliant frame deformation. The same working principle adopted for the implementation of the proposed force sensor has been exploited by the one of the authors in [28] for the implementation of joint position sensors in highly-integrated robotic hands [11]. In the case here reported, an optoelectronic element integrating both the LED and the PD

has been exploited for improving the sensitivity, the compactness, the noise rejection and reduce the assembly complexity. Moreover, in this case the working principle is applied to the measurement of a linear force instead of an angular position. The main advantages of the proposed solution consist in the design and assembly simplicity, the low-cost, the sensitivity, the noise rejection and the possibility of an easy integration in the same monolithic structure of an actuation module manufactured by 3D printing. In particular, the proposed sensor structure has been investigated for the integration of an affordable force sensor in a twisted string actuation module [9]. The chapter reports the description of the sensor working principle, the design of the compliant frame, its theoretical model and Finite Element Analysis (FEA), the experimental characterization of the light fork used as sensing elements and the mechanical properties validation for four sensor specimens characterized by different physical dimensions, manufacturing modality and materials. The sensor specifications, such as sensitivity, linearity, hysteresis area and bandwidth, have been experimentally verified by means of static calibration procedure and evaluation in dynamic conditions. Finally, the noise attenuation obtained by means of a simple modulation and filtering technique.

This chapter is structured as follows. In Sec. 5.1, the structure of the proposed device, its working principle and the modeling of the compliant sensor frames are presented. The experimental evaluation and the comparisons of the four different sensor specimens are described in Sec. 6.2 together with their static calibration and the dynamic response of the proposed devices. Finally, Sec. 7.3 draws some conclusion about the presented research activity.

5.1 Sensor Design

5.1.1 Sensor Structure

A schematic view of the sensor is reported in Fig. 6.4, where its main components are detailed. The mechanical structure is composed by two symmetric connection elements, where the external force is applied, that allows connecting the sensor with the transmission system by means of a couple of fixing holes, one for connection element. The two connection elements are linked by a couple of axial-symmetric compliant beams acting as linear springs. The compliant structure is designed to be symmetric with respect to the direction of the measured force to obtain homogeneous deformations. The connection elements are also provided with supports for, on one end, the PCB hosting the light fork, i.e. the sensing element, and, on the other end, the obstacle occluding the light path going from the LED to the PD. The obstacle is provided by an offset regulation mechanism, composed by a screw used to adjust its position with respect to the light fork. This mechanism is used to perform a fine selection of the working point in resting conditions along the light fork characteristic curve, the point *A* in Fig. 5.5.

A detailed 3D view of the compliant frame CAD of one of the specimen used during the experimental validation is reported in Fig. 5.1b. From this picture, it can be appreciate in detail how the elements composing the sensor have been implemented. The sensor mechanical structure should be compatible with the optoelectronic component dimensions and properly designed to achieve the linear displacement within the force range.

The OMRON EE_SX1108 photomicrosensor, here called light fork because of its “forked” structure, is the sensitive element used for the implementation of the proposed sensor, and its design details are reported in Fig. 5.2. In particular, Fig. 5.2a portrays the

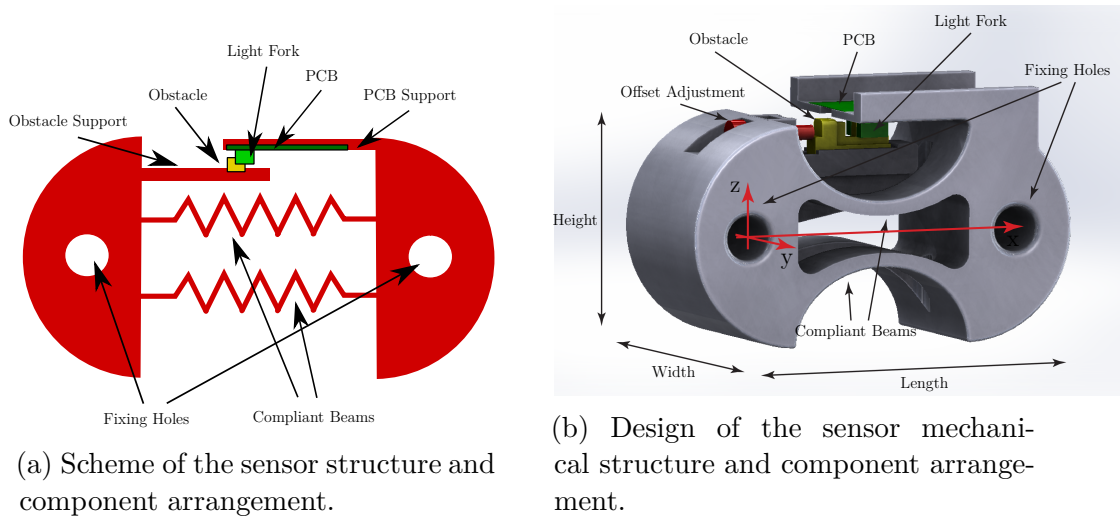
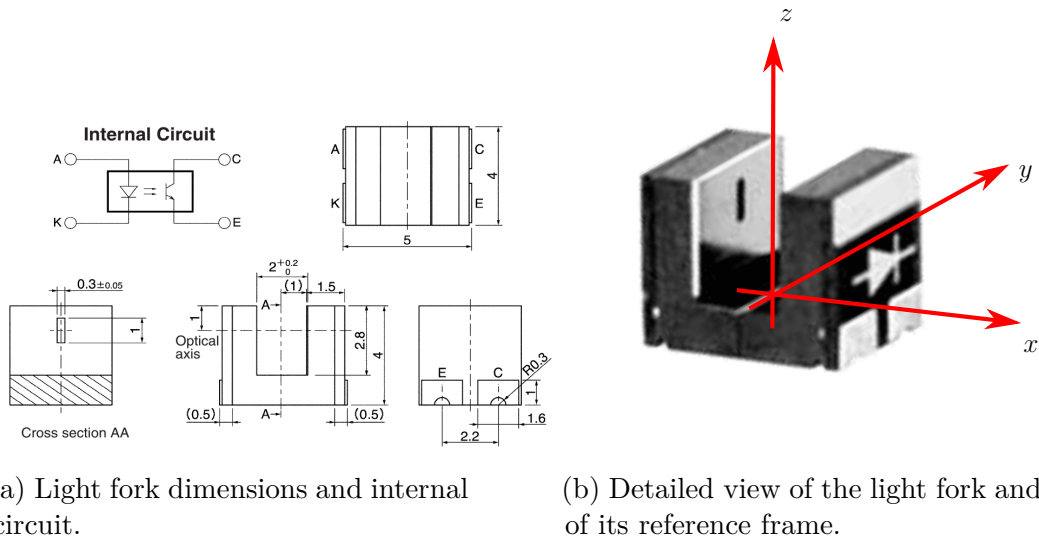


Fig. 5.1 Schematic view and design of the proposed force sensor: the compliant frame structure and the detailed view of the light fork and obstacle arrangement.

light fork sketch, dimensions and internal circuit, whereas in Fig. 5.2b the optoelectronic component can be seen in detail together with its reference frame. This component embeds both an LED and a PD (a phototransistor) facing each other and is provided with a window restricting the light cone coming from the LED to the PD to a thin and well-focused region. Several advantages accompany the use of this component. In particular, a compact sensor implementation is permitted because both the LED and the PD are embedded together in a compressed structure with precise relative position.

In order to provide an estimation of the sensor cost¹, the average cost of the light fork is about 1.29 Euro and the precision resistors for the LED and PD polarization cost about 0.3 Euro each on the retail market, while the cost of the PCB is 2 Euro. Moreover, the cost of the compliant frame in the worst case (Specimen 1, manufactured by 3D printing in ABS plastic) is about 20 Euro for the materials and a couple of machine hours for the production of the part. It is worth mentioning that in case of 3D printing, the part

¹The cost reported in the following have been taken from popular worldwide electronic components distributors, such as RS, Farnell and Digi-Key. These cost of electronic components is subject to continuous changes according to market quotations.



(a) Light fork dimensions and internal circuit.

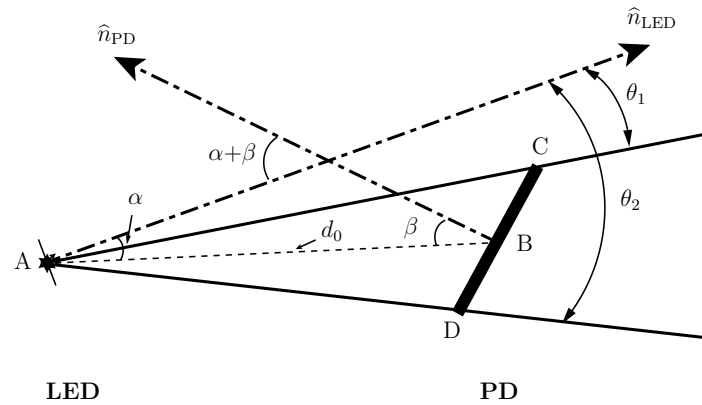
(b) Detailed view of the light fork and of its reference frame.

Fig. 5.2 Detailed view of the light fork (from OMRON EE_SX1108 datasheet).

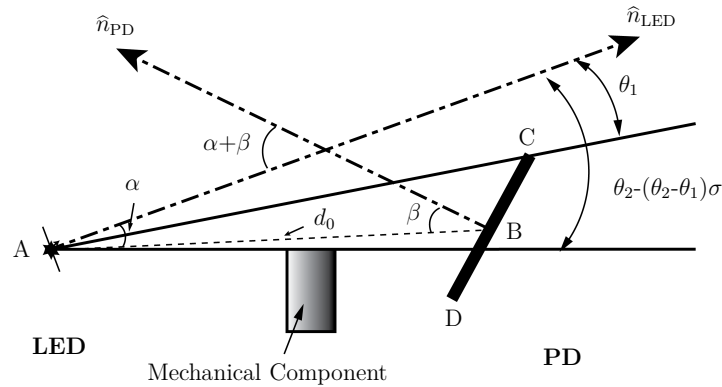
is produced directly from the CAD design without any intermediate working step. It follows that the overall cost is around 25 Euro and about 4 hours of parts production and assembly (the time are overestimated). In contrast, a set of 4 strain gauges for a complete Wheatstone bridge costs not less than 72 Euro in the retail market, and the conditioning electronics (instrumental amplifiers) for achieving the same signal level of the proposed solution needs to be added other than the cost of the compliant frame manufacturing and assembly time. A complete single-axis force sensor with the same range of the one proposed in this chapter (0-80 N) costs around 170 Euro in the retail market (conditioning electronics excluded).

5.1.2 Sensor Working Principle

The sensor working principle is based on the modulation of the current flowing through the PD achieved by means of a mechanical component, namely the obstacle, that partially intercepts the light emitted by the LED and received by the PD itself. The interaction between the LED and the PD when no obstacle limits the light flow and



(a) Interaction between a LED and a PD.



(b) Interaction between a LED and a PD with an obstacle.

Fig. 5.3 Schematic representation of the LED-PD interaction.

assuming that the LED is a point light source and the PD a finite receiver surface, is depicted in Fig. 5.3a: in this conditions, the current flowing through the PD depends on the relative position between the LED and the PD only [50]. The optical axes of LED and PD are respectively defined as \hat{n}_{LED} and \hat{n}_{PD} . α and β are the angles between the optical axis of the LED and the distance d_0 , and the optical axis of the PD and the same distance d_0 , respectively. It is evident that \overline{AC} presents a receiving angle with respect to \hat{n}_{PD} equal to $\alpha + \beta - \theta_1$, while \overline{AD} represents a receiving angle of $\alpha + \beta - \theta_2$.

In these conditions, the optical power P_0 can be computed through the following relation

$$P_0 = K \int_{\theta_1}^{\theta_2} I(\theta)R(\alpha + \beta - \theta) d\theta \quad (5.1)$$

where K is a constant representing the device characteristics, $I(\theta)$ and $R(\theta)$, the radiation pattern of the LED and the responsivity pattern of the PD, respectively.

When an obstacle is inserted between the LED and the PD, a specific amount of light is intercepted by the obstacle and the PD measures an optical power of $P(\sigma)$. The obstacle position is defined by a variable σ ranging from 0 in case of no occlusion to 1 in case of full occlusion. The amount of light emitted to the PD is restricted by the angles θ_1 and $\theta_2 - (\theta_2 - \theta_1)\sigma$. Therefore, the optical power received by the PD when considering the obstacle is a function of σ and can be represented as seen below

$$P(\sigma) = K \int_{\theta_1}^{\theta_2 - (\theta_2 - \theta_1)\sigma} I(\theta)R(\alpha + \beta - \theta)d\theta \quad (5.2)$$

where K is a constant representing the device characteristics, $I(\theta)$ and $R(\theta)$, the radiation pattern of the LED and the responsivity pattern of the PD, respectively. If $\sigma = 0$, i.e. no occlusion, $P(\sigma) = P_0$, while when the obstacle is moved in between the LED and the PD, $\sigma \rightarrow 1$ and $P(\sigma) \rightarrow 0$ (the total occlusion implies $P(1) = 0$).

Since in the light fork the optical axes of LED and PD, respectively, \hat{n}_{LED} and \hat{n}_{PD} , are aligned, α and β are equal to zero. Furthermore, the relation between the relative light current I_L and $P(\sigma)$ can be defined as

$$I_L = K_I P(\sigma) \quad (5.3)$$

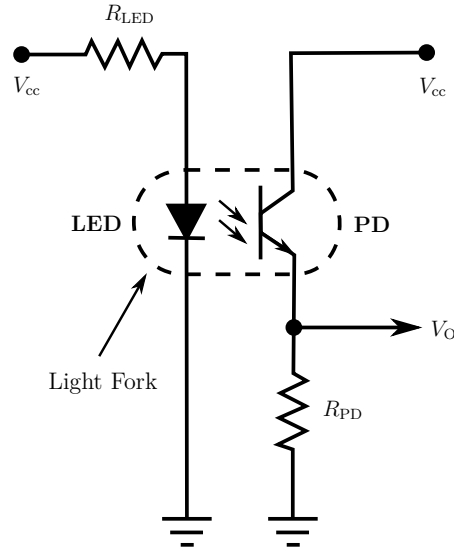


Fig. 5.4 Measuring circuit for the force sensor based on optoelectronic component.

where the K_I is a constant representing the PD characteristic. The sensor output voltage V_O can be computed from

$$V_O = R_{PD} I_L \quad (5.4)$$

The changes in light power received by the PD can be acquired by measuring the output voltage V_O of the simple conditioning circuit reported in Fig. 5.4. Given the supply voltage V_{cc} , the maximum sensor output voltage $V_{O_{max}}$ can be selected avoiding the saturation of the PD. Then, given the maximum obstacle displacement σ_{max} , the PD load resistance R_{PD} can be computed from (5.4) and (5.3) as follows

$$R_{PD} = \frac{V_{O_{max}}}{K_I P(\sigma_{max})} \quad (5.5)$$

The light cone of the light fork used in the proposed sensor design is well shaped, pro-

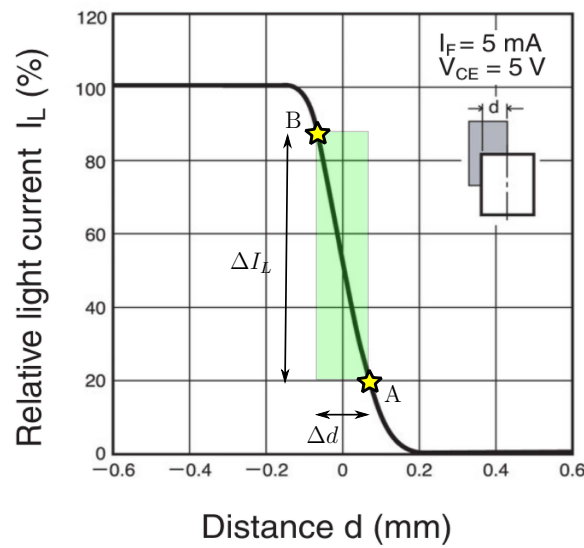
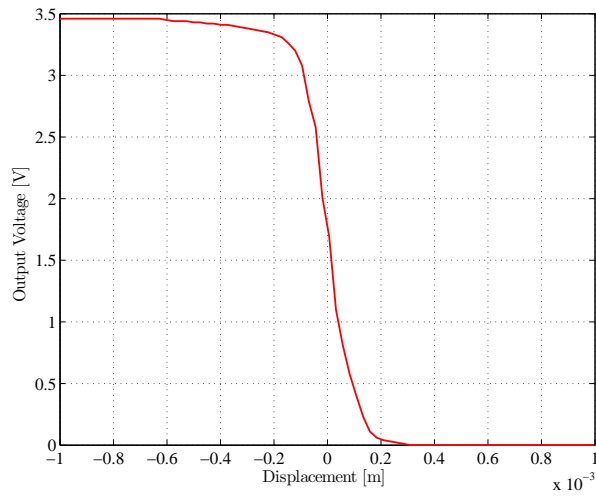


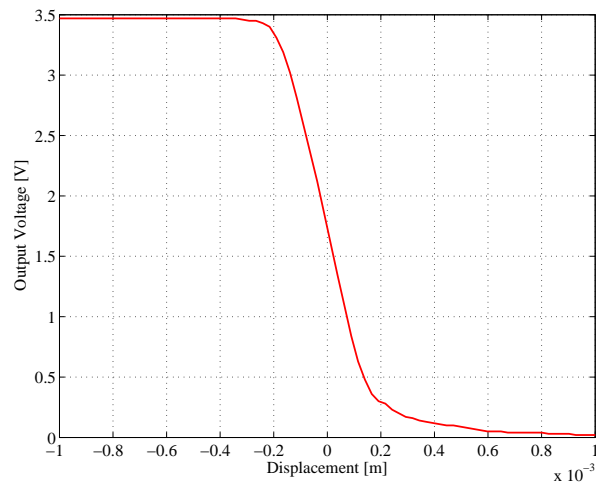
Fig. 5.5 Responsivity curve of the light fork: it is possible to note the variation of the PD current (about 70%) with respect to the obstacle displacement (0.12 mm) from the point A to the point B.

viding a very steep and linear transition region between the fully covered and the fully free light conditions and allowing a good sensitivity and linearity to be obtained. As shown in Fig. 5.5, where the component transition curve as a function of the obstacle position is reported, the light current I_L goes from about 10% to 90% in a quite linear way along an obstacle displacement range of about ± 0.1 mm with respect to the window center position. In this figure, the large variation of the relative light current ΔI_L over a very limited variation of the obstacle displacement Δd in a very suitably selected region has been highlighted in which the no-load working point A, and the maximum load working point B are indicated respectively in the lower and higher part of the response characteristic.

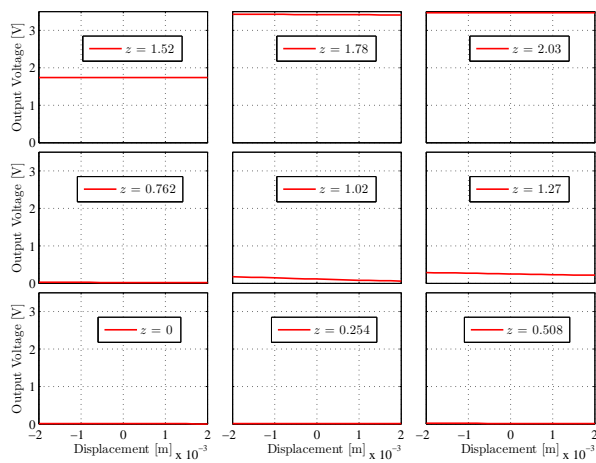
Therefore, the compliant frame design problem consists in the design of a mechanical structure exhibiting a linear displacement of about 0.2 mm when the load force ranging from 0 to 80 N is applied. It is worth mentioning that this force range is assumed as initial test, the force range and therefore the compliant frame design can be adjusted



(a) Experimental responsivity curve of the light fork along the y -axis.



(b) Experimental responsivity curve of the light fork along the z -axis.



(c) Experimental responsivity curve of the light fork along the x -axis for different values of the obstacle position along the z -axis.

Fig. 5.6 Responsivity curve of the light fork.

in case the particular application requirements are different. Due to the properties of the light fork responsivity curve, only the position of the obstacle with respect to the window along the measurement axis requires precise positioning, whereas the relative position between the light fork and the obstacles in the other directions does not significantly affect the sensor response within the limits of the arrangement adopted for the sensor implementation. The assembly of the sensor is subsequently much simpler than in the case of alternative solutions based on strain-gauges or optoelectronic components. It is well-known in the field of load cell manufacturing that the bonding of strain gauge on the compliant frame is a delicate phase requiring well-trained operators. On the other hand, several optoelectronic force sensors implementations requires precise positioning of the components. It follows that these solutions are sensitive to assembly errors. In contrast, the proposed solution is less prone to this problem, and to verify this point, the experimental validation of the light fork sensing characteristic has been performed, verifying the sensitivity with respect of the obstacle position not only during the movement along the principal measurement axis (i.e. the y -axis) but also along the other (secondary) axes. The experimental results reported in Fig. 5.6a confirm the light fork characteristic reported in Fig. 5.5 provided by the manufacturer, whereas Fig. 5.6b shows that if a sufficient displacement along the z -axis is taken into account, the device is almost insensitive to obstacle position variations. Finally, Fig. 5.6c shows that the light fork is almost insensitive to obstacle position changes along the x -axis even for different value of the obstacle position along the z -axis. The aforementioned relationship between the amount of interception and the measured power can be then used to optimize the design of the force sensor in order to fulfill the specifications in terms of linearity and sensitivity (see Fig. 5.5).

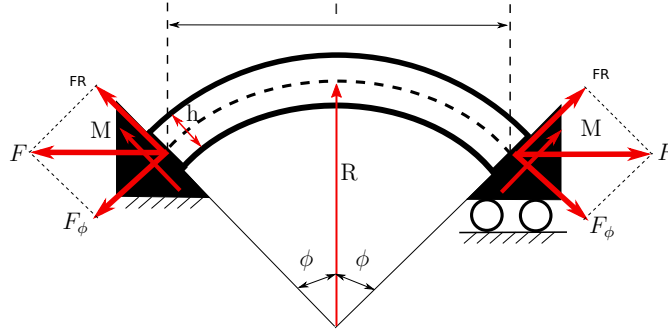


Fig. 5.7 Deflection of curved beam

5.1.3 Compliant Frame Design

The mechanical structure is designed to exhibit symmetric deformations along to the measured force direction (the y -axis). Moreover, the compliant frame is designed to achieve a linear displacement with the desired force range and must be compatible with the dimensions of the remaining parts of the actuation module and of the light fork.

In this section, the analysis focuses on the modeling and design of the curved beams, that are the main compliant element of the structure. The overall compliant frame is composed by four curved beams symmetrically arranged around the symmetry axis of the sensor (i.e. the measurement direction) to achieve linear displacement along the measurement direction. In Fig. 5.7, the behavior of a single curved beam subject to load along the sensor axis is shown. In this scheme, a curved uniform beam with rectangular section is considered, and the load force F is decomposed in its components along the beam axes (axial force F_ϕ) and transverse to the beam (shear force F_r). Moreover, due to the sensor structure and beam constraints, the load force generates also a moment at the beam ends, as schematically reported in Fig. 5.7. Generally speaking, the deflection of the curved beam can be calculated using Castigliano's theorem [51]

$$\delta = \frac{\partial U}{\partial F} \quad (5.6)$$

where δ is the deflection, U is the strain energy and F is the applied force. According to Fig. 5.7, the total strain energy in the beam consists of four terms

$$\delta = \frac{\partial U_1}{\partial F} + \frac{\partial U_2}{\partial F} + \frac{\partial U_3}{\partial F} + \frac{\partial U_4}{\partial F} \quad (5.7)$$

where U_1 is the strain energy due to bending moment M

$$M = F R \sin \phi$$

$$U_1 = \int_{\frac{\pi}{2}-\phi}^{\frac{\pi}{2}+\phi} \frac{M^2}{2 A e E} d\gamma = \frac{F^2 R^2}{2 A e E} \int_{\frac{\pi}{2}-\phi}^{\frac{\pi}{2}+\phi} \sin^2 \gamma d\gamma \quad (5.8)$$

where $A = h b$ is the beam section area, being h and b the height and the thickness of the curved beam respectively, e is the eccentricity and E is the young modulus. e is a parameter that depends on the beam section shape, for the rectangular section it can be assumed

$$e = R - r_n, \quad r_n = \frac{h}{2}$$

where R is radius, r_n is the radius of the neutral axis. U_2 is the strain energy due to axial force F_ϕ

$$\begin{aligned}
 F_\phi &= F \sin \phi \\
 U_2 &= \int_{\frac{\pi}{2}-\phi}^{\frac{\pi}{2}+\phi} \frac{F_\phi^2 R}{2 A E} d\gamma = \frac{F^2 R}{2 A E} \int_{\frac{\pi}{2}-\phi}^{\frac{\pi}{2}+\phi} \sin^2 \gamma d\gamma
 \end{aligned} \tag{5.9}$$

whereas U_3 is the strain energy due to the bending moment produced by the axial force F_ϕ

$$U_3 = \int_{\frac{\pi}{2}-\phi}^{\frac{\pi}{2}+\phi} \frac{F_\phi M}{A E} d\gamma = \frac{F^2 R}{A E} \int_{\frac{\pi}{2}-\phi}^{\frac{\pi}{2}+\phi} \sin^2 \gamma d\gamma \tag{5.10}$$

Finally, U_4 represents the strain energy due to the transverse shear force F_r

$$\begin{aligned}
 F_r &= F \cos \phi \\
 U_4 &= \int_{\frac{\pi}{2}-\phi}^{\frac{\pi}{2}+\phi} \frac{F_r^2 C R}{2 A G} d\gamma = \frac{F^2 C R}{2 A G} \int_{\frac{\pi}{2}-\phi}^{\frac{\pi}{2}+\phi} \cos^2 \gamma d\gamma
 \end{aligned} \tag{5.11}$$

where C is a modifier dependent on the cross sectional shape ($C = 1.2$ for rectangular shape) and G is the shear modulus.

The beam deflection along the load force direction can be then easily computed by integrating (5.8), (5.9), (5.10) and (5.11) along the beam curvature angle ϕ and computing the derivative in (5.7), therefore it follows

$$\delta = \frac{F R}{12 A} \left[\frac{(4\pi + 3\sqrt{3})}{E} \left(\frac{R}{e} - 1 \right) + \frac{(4\pi - 3\sqrt{3}) C}{G} \right] \tag{5.12}$$

It is worth mentioning that the curved shape of the compliant beams has been selected mainly because of the quite simple mathematical modeling of this structure reported in the previous equations. For manufacturing reasons and to reduce the stress concentration at the beam connection points, corner fillet beams have been implemented, therefore the previous mathematical modeling will be verified, as reported in the following, both by means of FEA and experimentally. Moreover, for further validation of the proposed approach, four different compliant frame specimens have been designed by means of the previous mathematical model and validated.

5.2 Specimen Design and Experimental Evaluation

5.2.1 Experimental Setup

In Fig. 6.7 an overview of the experimental setup for verification of the proposed force sensor and compliant frame specimens is shown. This setup consists of a commercial linear motor (LinMot 37x160), which slider is attached to the force sensor compliant frame through a rigid component in order to apply varying forces along the sensor measurement axis. The linear motor is equipped with a strain gauge load cell used as reference sensor that can measure a maximum force of 100 N. The linear motor is also provided with an integrated encoder with a resolution of 1 μm for the measurement of the compliant frame deformation. The linear motor load cell is connected to the amplifier through a shielded cable for noise rejection and the optoelectronic components of the proposed force sensor is connected to the circuit reported in Fig. 5.4.

A low-level control system is used to drive the linear motor in order to apply different force profile compensating on the friction acting on the motor slider [16]. A PC-104

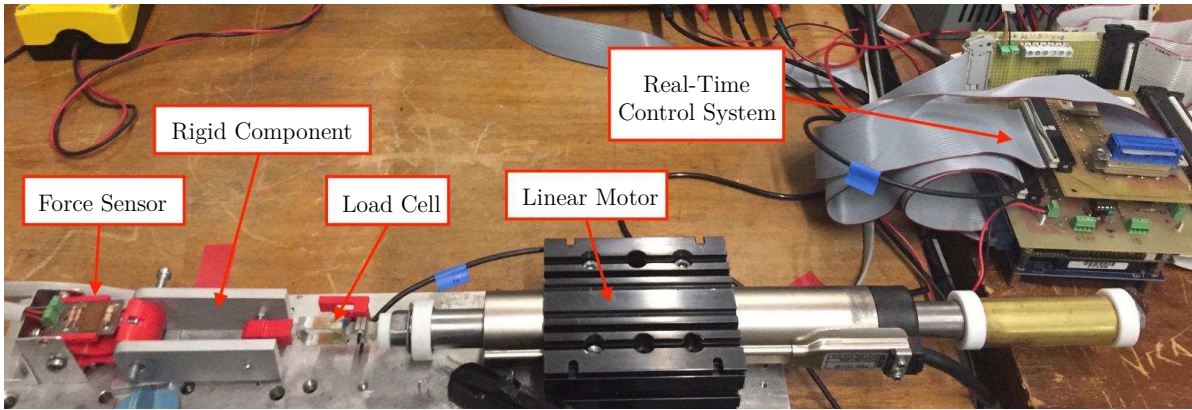


Fig. 5.8 Overview of the experimental setup.

Parameter	Unit	Spec. 1	Spec. 2	Spec. 3	Spec. 4
Height	mm	30	30	40	30
Width	mm	24	14	14	24
Length	mm	55	55	65	55
h	mm	2.9	2.9	3.7	2.9
b	mm	9	4	3	9
R	mm	17.32	17.32	17.32	17.32
ϕ		$\pi/6$	$\pi/6$	$\pi/6$	$\pi/6$
l	mm	25	25	25	25
δ_{\max}	mm	0.062	0.140	0.112	0.051

Table 5.1 Parameters of the four compliant frame specimens.

running RTAI-Linux real-time operating system and a Sensoray 526 data acquisition board is used for data collection and to control the system during the experiment. The force sensor is mechanically fixed with the measurement axis aligned with the one of the load cell which is mounted to the slider of the linear motor in order to obtain a ground truth measurement of the applied force during the experiment.

5.2.2 Specimen Design and Comparison

The comparison between four compliant frame specimens, namely Specimen 1, 2, 3 and 4 respectively, has been performed to validate the proposed design methodology and to select the most appropriate structure to be integrated into the twisted string actuation module. Table 5.1 reports the dimensions, design and beam parameters characterizing the four frame specimens. In Tab. 5.1, l represents the linear distance between the beams connection points and δ_{\max} represent the deformation at maximum load, i.e. 80 N, adopted during the specimen design. As can be seen, the four specimens have been designed to exhibit a different maximum deformation, this will allow to evaluate which specimen provides a better exploitation of the light fork characteristic. The frame specimens 1, 2 and 3 have been manufactured in ABS plastic by 3D rapid prototyping (by means of a Stratasys Dimension ELITE 3D printer) while the frame specimens 4 is made of DELRIN[®] plastic by CNC milling. The proposed specimens have also been verified by means of a FEA and experiments where an increasing load ranging from 0 to 80 N is applied and the frame deformation is measured. The FEA has been carried out with SolidWorks software with a maximum mesh size of 0.6813 mm, 0.5612 mm, 0.6639 mm and 0.6813 mm respectively for specimen 1, specimen 2, specimen 3 and specimen 4. The experimental setup for measuring these data is described in detail in Sec. 5.2.1. Figure 5.9 shows the results of the FEA performed on the four specimens at the maximum load conditions: this pictures allows to appreciate the differences among the specimens, to verify that the stress, and consequently the deformation, is concentrated on the curved beams and that the maximum stress is well below the ABS yield stress, $3.1e^{+07} N/m^2$ (from ABSplus Spec Sheet²) and DELRIN[®] yield stress, $6.2053e^{+07} N/m^2$ (from DELRIN[®] Spec Sheet³). It results that the Factor-of-Safety is 5.5 for Spec. 1, 2.7 for Spec. 2, 3.3 for

²Stratasys, <http://www.stratasys.com/materials/fdm/absplus>

³DELRIN[®], [http://www.sdplastics.com/delrin/delrin\[1\].pdf](http://www.sdplastics.com/delrin/delrin[1].pdf)

Spec. 3 and 11 for Spec. 4. The comparison between the theoretical deformation, the one evaluate by FEA and the experimentally measured deformation of the four compliant frame specimens is reported in Fig. 5.10. These plots allows to evaluate that, for all the specimens, both the theoretical model and the FEA analysis fit very well with the experimental measurements. In particular, for all the specimens, it can be noted that the measured deformation is slightly smaller than the FEA, which can be caused by the manufacturing process, and that the theoretical deformation is slightly larger than both the FEA and the measurement, that can be ascribed to model approximations and corner fillet beam ends.

Table 5.2 reports the RMS error (over the whole measurement) between the measured deformation and the FEA e_{FEA} and between the measured deformation and the theoretical one e_{th} for the four specimens. Moreover, the linearity RMS error e_L of the measured deformation (i.e. the RMS error between the measured deformation and its linear approximation over the whole measurement) is also reported in Tab. 5.2 to highlight the linearity of the four specimen deformation. The data reported in Tab. 5.2 are expressed as a percentage of the maximum measured deformation. In Tab. 5.3 the maximum deformation obtained by FEA (δ_{maxFEA}) and experimental measurements (δ_{maxREAL}) are also reported for comparison with one adopted during compliant frame design (δ_{max}).

In Tab. 5.3 the maximum deformation obtained by FEA (δ_{maxFEA}) and experimental measurements (δ_{maxREAL}) are also reported for comparison with one adopted during compliant frame design (δ_{max}).

5.2.3 Static Calibration

For the evaluation of the static response of the four compliant frame specimens, the optoelectronic sensing element has been mounted on each specimen and the calibration

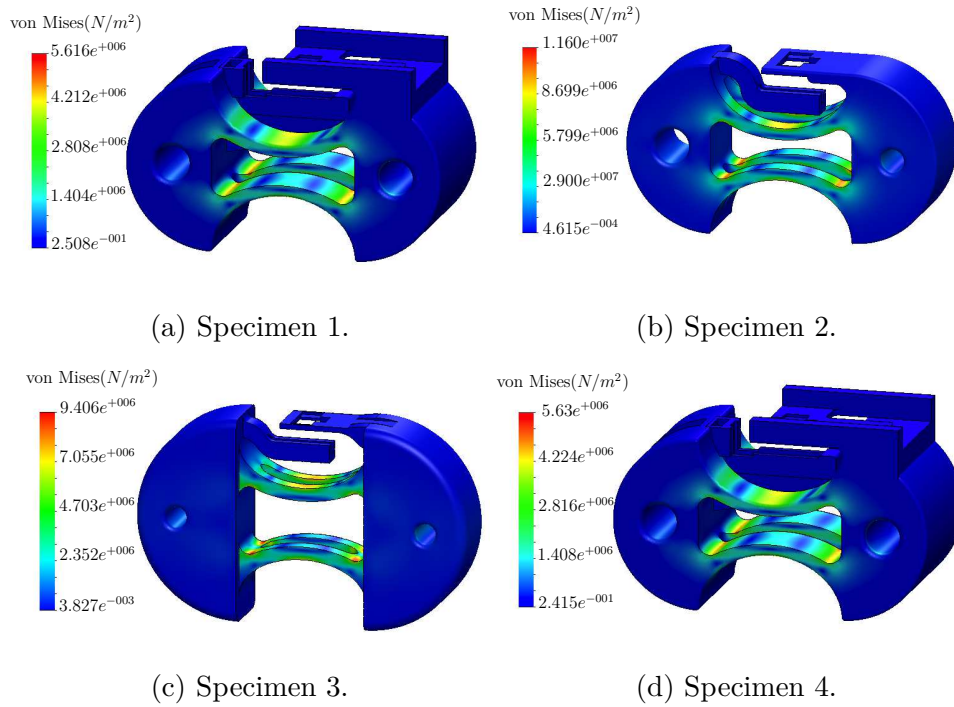
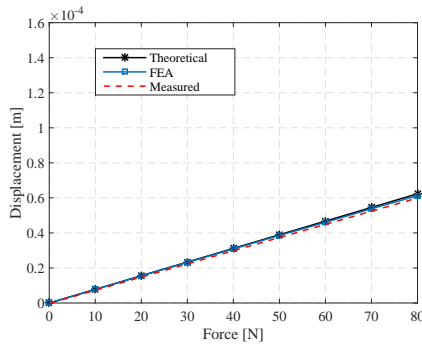
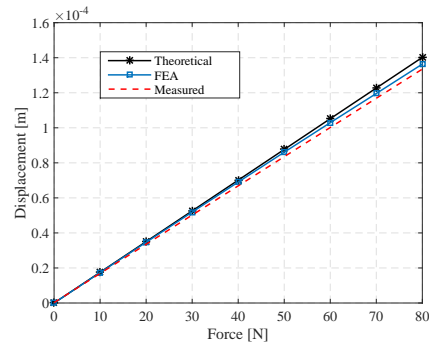


Fig. 5.9 FEA of the four compliant frame specimens.

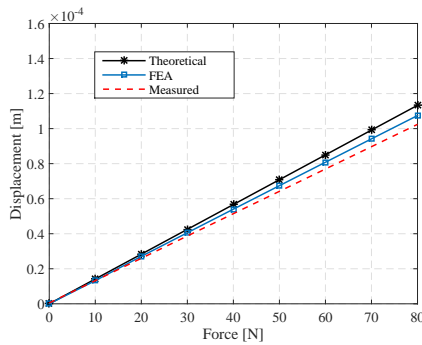
of the proposed four prototypes has been performed by applying a load force ranging from 0 to 80 N. In order to reconstruct the calibration curve of each specimen, the corresponding output voltage V_O has been measured using the conditioning circuit shown in Fig. 5.4. The calibration plots of the specimens are presented in Fig. 6.8: the experimental measures are compared with a suitable linear interpolation for evaluating the sensor linearity. The linearity error and the sensitivity of the four specimens are reported in Tab. 5.4. It is possible to note that, even if the specimen 2 presents a slightly larger linearity error with respect to specimen 1, it shows a significantly larger sensitivity, as expected considering the maximum deformation considered in the design of the specimens. It is also important to mention that, if a larger sensitivity can be good from the force measurement point of view, a larger deformation of the compliant frame implies a lower actuation module stiffness, facts that can have significant (sometimes negative from the stability point of view) implication on the control of the whole robotic



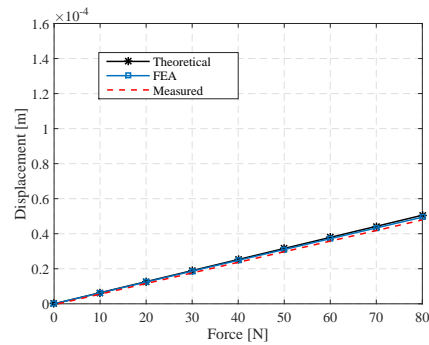
(a) Specimen 1.



(b) Specimen 2.



(c) Specimen 3.



(d) Specimen 4.

Fig. 5.10 Comparison between theoretical, FEA and experimental deformation of the three compliant frame specimens.

system. Therefore, having a larger sensitivity is not always a good choice, at least for this sensor implementation, this will strongly depend on the application and this is also the main reason why we performed this comparison among different specimens.

5.2.4 Dynamic Sensor Response

The four sensor specimens have been experimentally evaluated in dynamic conditions by means of a time-variable input force. The force applied to the force sensor is controlled using the experimental setup described in Sec. 5.2.1 by using of a force feedback loop based on the data coming from the load cell mounted on the slider of the linear motor.

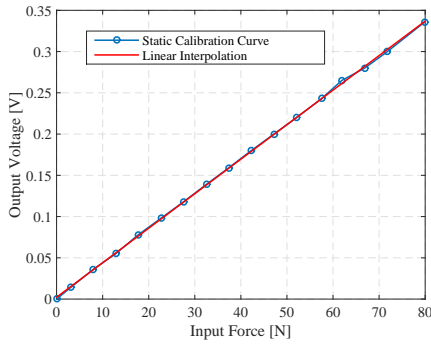
RMS Error [%]	Spec. 1	Spec. 2	Spec. 3	Spec. 4
e_{FEA}	0.75	1.64	2.97	0.98
e_{th}	1.78	4.73	8.76	2.50
e_{L}	0.0017	0.0010	0.0014	0.0023

Table 5.2 RMS errors with respect to the experimental deformation measurements of the four compliant frame specimens (values are expressed as a percentage of the maximum deformation).

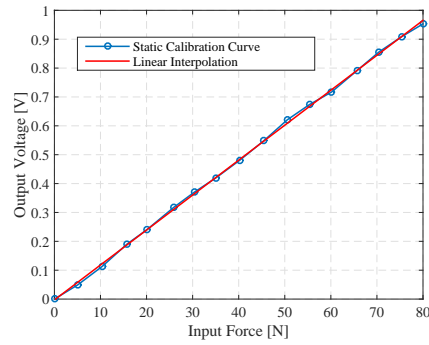
Max. Deformation [mm]	Spec. 1	Spec. 2	Spec. 3	Spec. 4
δ_{max}	6.2E-5	1.40E-4	1.12E-4	5.1E-5
δ_{maxFEA}	6.11E-5	1.36E-4	1.08E-4	4.95E-5
δ_{maxREAL}	6.01E-5	1.33E-4	1.05E-4	4.79E-5

Table 5.3 Maximum deformation of the four compliant frame specimens.

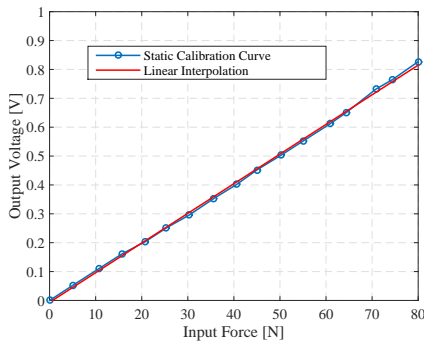
A sinusoidal signal with amplitude ranging from 0 to 80 N and with increasing frequency from 0.1 to 20 Hz (close to the limit of the linear actuator) has been adopted to evaluate the sensor bandwidth. In order to account for the actuator limitations, the comparison between the reference sensor (the linear motor load cell based on strain-gauges) force, namely the input force, and the force measured by the the proposed sensor implementation, namely the output force, is reported in Fig. 5.12 for the four specimens under evaluation. In the right column of Fig. 5.12, the input/output frequency analysis is reported to ease the evaluation of the sensor bandwidth. From these plots, it is possible to see that input to output ratio remains close to one (0 dB) along the whole frequency range of the test signal (from 0.1 to 20 Hz), and a limited phase delay is observed toward the higher frequencies. This result shows that the sensors have a bandwidth larger than 20 Hz, since no significant variation in the frequency response can be appreciated within the input signal frequency range. The magnitude and phase after the high input signal frequency limit (20 Hz, about 125 rad/s) is reported for completeness but is not significant due to the limited frequency contents of the input signal in this range.



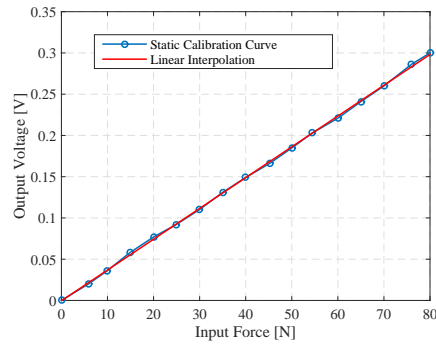
(a) Specimen 1.



(b) Specimen 2.



(c) Specimen 3.



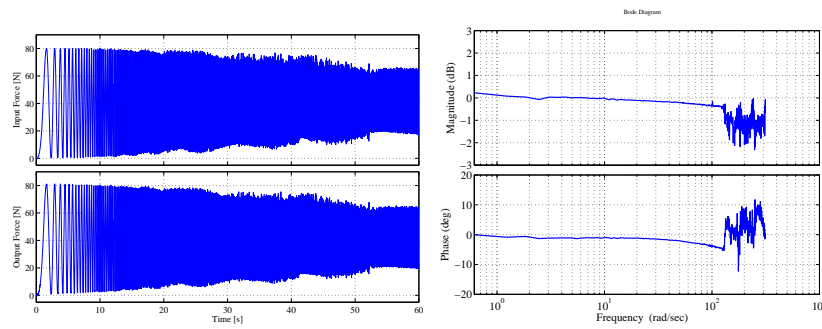
(d) Specimen 4.

Fig. 5.11 Static calibration of the sensors.

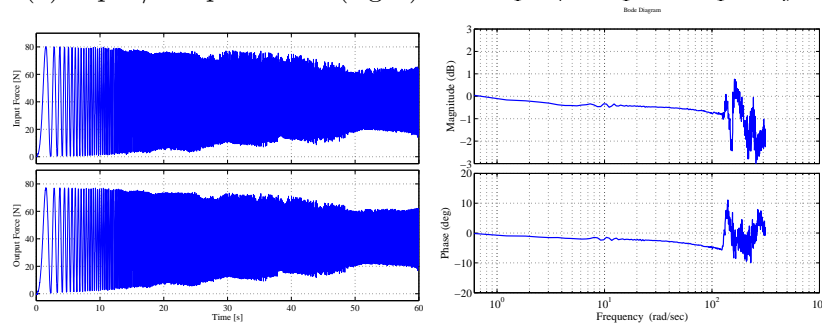
	Unit	Spec. 1	Spec. 2	Spec. 3	Spec. 4
Linearity error	%	1.11	1.25	1.48	1.03
Sensitivity	mV/N	4.2	12.1	10.3	3.7

Table 5.4 Linearity error of the calibration curve

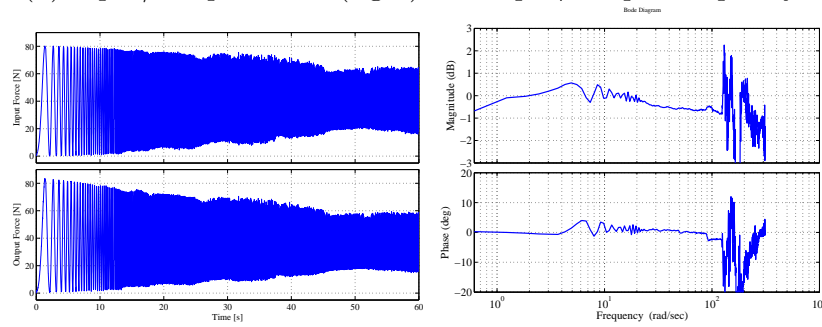
To highlight possible viscoelastic effects affecting the proposed sensors, the input/output relation for some particular frequencies, 0.2, 0.5, 1, 1.5 and 2 Hz, are reported in Fig. 6.9 for the four sensor specimens. From these plots, By comparing the sensor response with the linear interpolation, it is possible to note that a very limited hysteresis is present for all the specimens. In Tab. 5.5 the mean values of the hysteresis areas over each cycle of the plots shown in Fig. 6.9 are reported. These values are computed as a percentage of the full scale measurement, i.e.



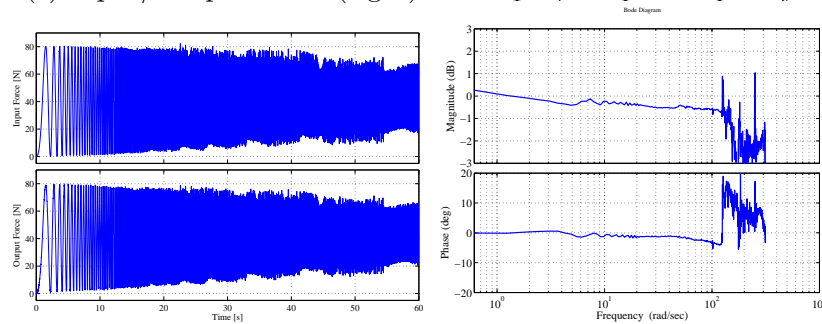
(a) Input/Output Force (right) and Input/Output frequency analysis (left) for specimen 1.



(b) Input/Output Force (right) and Input/Output frequency analysis (left) for specimen 2.



(c) Input/Output Force (right) and Input/Output frequency analysis (left) for specimen 3.



(d) Input/Output Force (right) and Input/Output frequency analysis (left) for specimen 4.

Fig. 5.12 Evaluation of the response to a chirp signal varying from 0.1 to 20 Hz for the four sensor specimens.

Spec. No.	0.2 Hz	0.5 Hz	1 Hz	1.5 Hz	2 Hz
1	0.4520	0.9933	0.4475	0.2491	0.5638
2	0.5293	0.0103	0.9744	0.2660	0.5887
3	0.9516	0.9380	0.0086	1.4533	0.6859
4	0.4457	1.2595	1.1368	0.7878	1.6595

Table 5.5 Mean hysteresis areas for different frequency values (areas are expressed in N²).

	Unit	Spec. 1	Spec. 2	Spec. 3	Spec. 4
Accuracy	N	1.88	1.98	2.39	2.18

Table 5.6 Accuracy of the developed sensors for the four specimens.

$$e_{H\%} = 100 \frac{\sqrt{\frac{1}{N} \sum_{i=0}^{N-1} (F_{IN_i} - F_{OUT_i}) \Delta F_{IN_i}}}{F_{\max}} \quad (5.13)$$

where N is the number of measurement samples, $F_{\max} = 80$ N is the maximum input force, F_{OUT_i} is the i -th sample of the force measured by the sensor, F_{IN_i} is the i -th sample of the input force imposed to the sensor and $\Delta F_{IN_i} = F_{IN_i} - F_{IN_{i+1}}$ is the variation of the input force between to consecutive measurement samples. These data show that there is no strict relation between hysteresis areas and signal frequency. Finally, considering hysteresis error in the worst case and the linearity error reported in Tab. 5.4, the accuracy (i.e. the error bound over the whole measurement range) of the four specimens has been computed, and these values are reported in Tab. 5.6.

5.2.5 Evaluation of measurement noise

As mentioned in Sec. 5.1, the sensor acquisition electronics has been kept as simple as possible to reduce the overall cost and easy the integration with other systems. On the

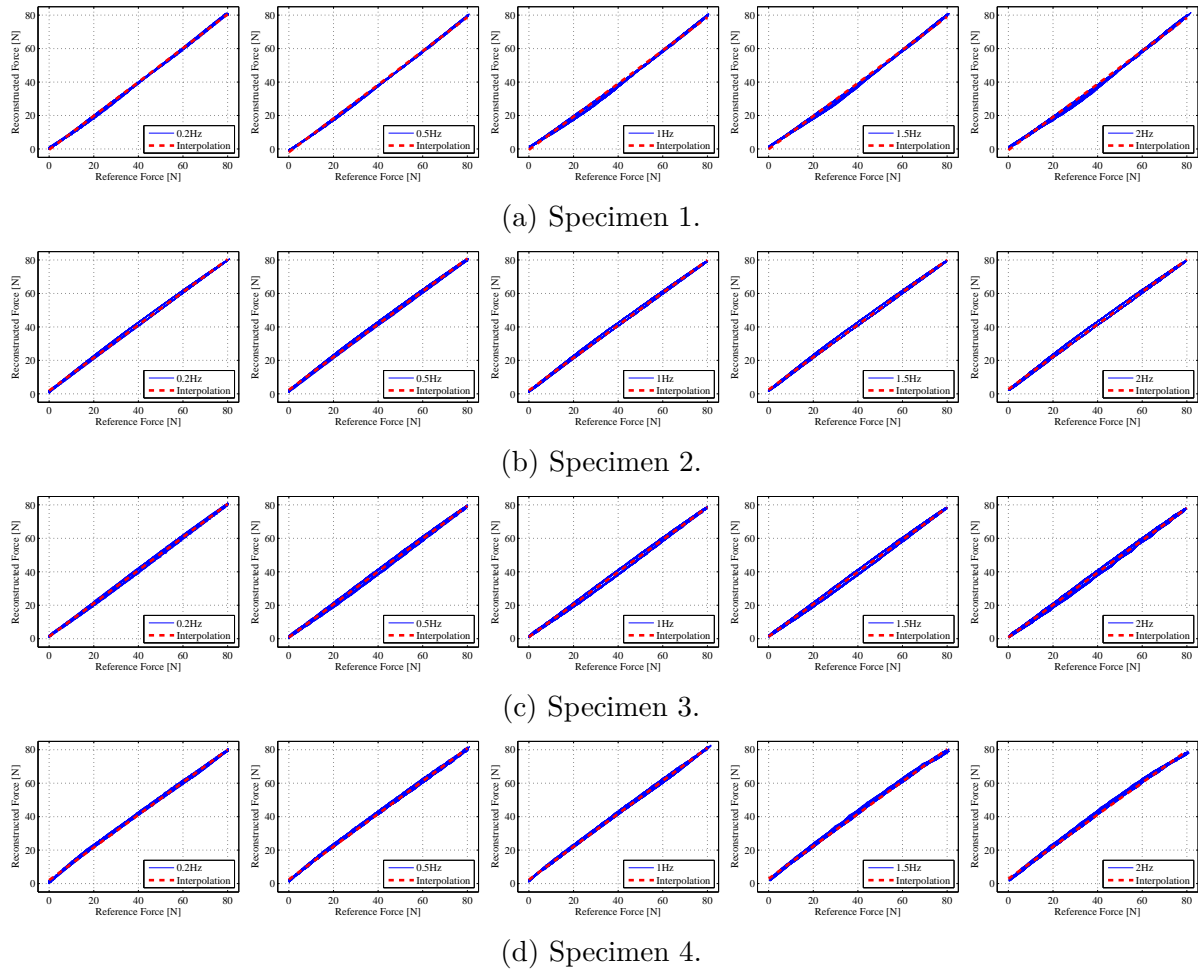


Fig. 5.13 Experimental evaluation of the force sensor hysteresis for the different specimens at frequencies ranging from 0.2 to 2 Hz.

other hand, a simple improvement that allow to significantly reduce the measurement noise of the proposed sensor consists in switching on and off the LED at high frequency (LED pulsing) and band-pass filtering the PD response at that same frequency to remove the effect of ambient light and other DC sources. In turn this solution request a more complex electronics to control the LED power supply and to synchronize the data sampling with the LED power source to avoid ripple induced in the measurement by non-ideal filtering. To evaluate this solution, the acquisition system represented in Fig. 5.14 has been implemented for the proposed sensor. The sampling of the output voltage V_{filt} has been executed synchronously and at the same frequency of the PWM

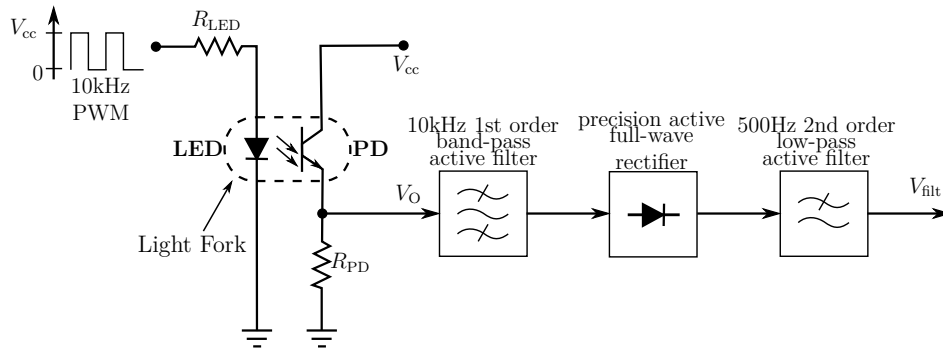


Fig. 5.14 Measuring circuit with PWM LED modulation for noise reduction.

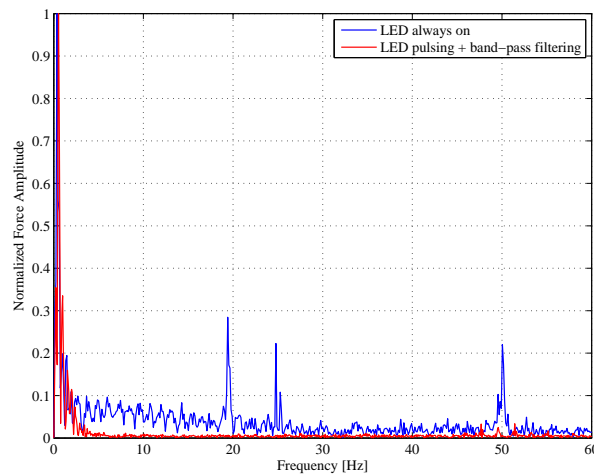


Fig. 5.15 Comparison of the measurement spectrum with and without LED pulsing.

LED supply source to reduce measurement ripple. The measurements collected in this way have been compared with the ones acquired with the LED powered with a constant supply source in terms of power spectrum. In Fig. 5.15 the comparison of the normalized measurement error power spectrum with and without LED pulsing for a 0.5 Hz full scale (80 N) input force is reported. While the spectrum are almost overlapped in the frequency range of the input signal, these plots clearly shows that the noise affecting the measurement is significantly attenuated by the LED pulsing and band-pass filtering. Therefore, the adopting of this acquisition technique can be taken into account for improving the signal-to-noise ratio.

5.3 Conclusions

This work reports the development of a low-cost and easy-to-build force sensor using as sensing element a commercial and very compact optoelectronic component, called light fork, embedding both the light source (LED) and the photodetector (phototransistor). The particular structure of the proposed sensor and the characteristics of the sensing element, the light fork, other than allowing a compact device implementation, allow the easy implementation of the force sensor without requiring particular care or experience in the component assembly. This allowed us to perform a quite fast evaluation of different design implementations.

The mathematical model of the sensor compliant frame has been presented and validated by means of both FEA and experimental evaluation of four different sensor specimens. These results confirmed the proposed design approach. The four sensor specimens have been also evaluated by means of static calibration and dynamic loading experiments, showing the good linearity and sensitivity of the implemented devices, which are also characterized by very limited hysteresis.

Future activities will be devoted to the development of robotic applications exploiting the proposed actuation module with integrated optoelectronic force sensor. Moreover, the use of the light fork for the implementation of multi-axis force/torque sensors will be investigated.

Chapter 6

Actuation Module

Research laboratories worldwide are concurrently designing a novel era of robots that are much more advanced than their predecessors in terms of cognitive capabilities and are able to adapt to constantly changing environments. These new robots have been intentionally designed for physical interaction with unstructured environments and humans. To achieve this objective, the measurement of the interaction forces is of paramount importance. A very important area where force and torque sensors play a key role is the development of wearable robotic devices, such as servo-actuated prostheses and exoskeletons. In these devices, the force and torque measurements are used to support and fulfill the human goals. An exoskeleton is a wearable robotic system designed for a variety of purposes. More specifically, it is an external structural mechanism with joints and links corresponding to those of the human body with important applications in rehabilitation and haptic operation, ultimately benefiting all populations, both disabled and healthy. In more recent years, the use of exoskeletons for the hand and lower/upper-limb support applications has drastically increased [31, 32, 52].

In this chapter, a novel design of a TSA module, schematically depicted in Fig. 6.1 is presented. This TSA module is characterized by an integrated force sensor and embed-

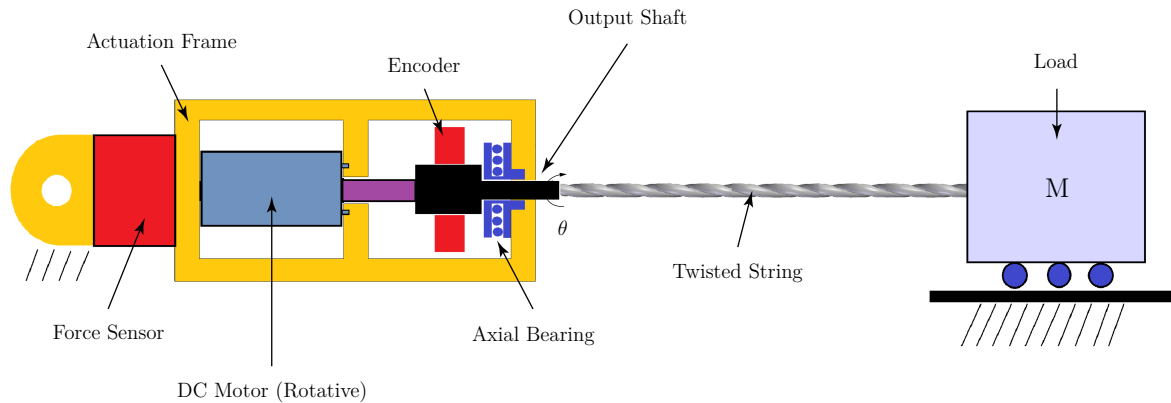


Fig. 6.1 Schematic representation of the twisted string actuation system structure.

ded acquisition and control electronics. The motor module structure is manufactured in ABS plastic by 3D printing, and a commercial optoelectronic component, called light fork because of its forked structure, has been adopted for the force sensor implementation. The light fork hosts in its package both the Light Emitting Diode (LED) and the Photodetector (PD) required for measuring the compliant frame deformation. This solution presents several advantages with respect to alternative strain-gauge based or optoelectronic based solutions, such as a simpler assembly, because of the well-defined package, high sensitivity and low cost. The module is driven by a low-cost DC motor, and a combined axial-radial bearing is adopted to support the output shaft at the location of the twisted string connection. Moreover, the actuation module is also provided with an optical encoder for output shaft position measurement. The Finite Element Analysis (FEA) together with experimental measures has been executed to validate the actuation module design, and the sensor calibration process has been performed. To validate the properties of the proposed TSA module, an experiment has been performed in dynamic conditions, and the results have been validated by means of a reference strain-gauge based force sensor.

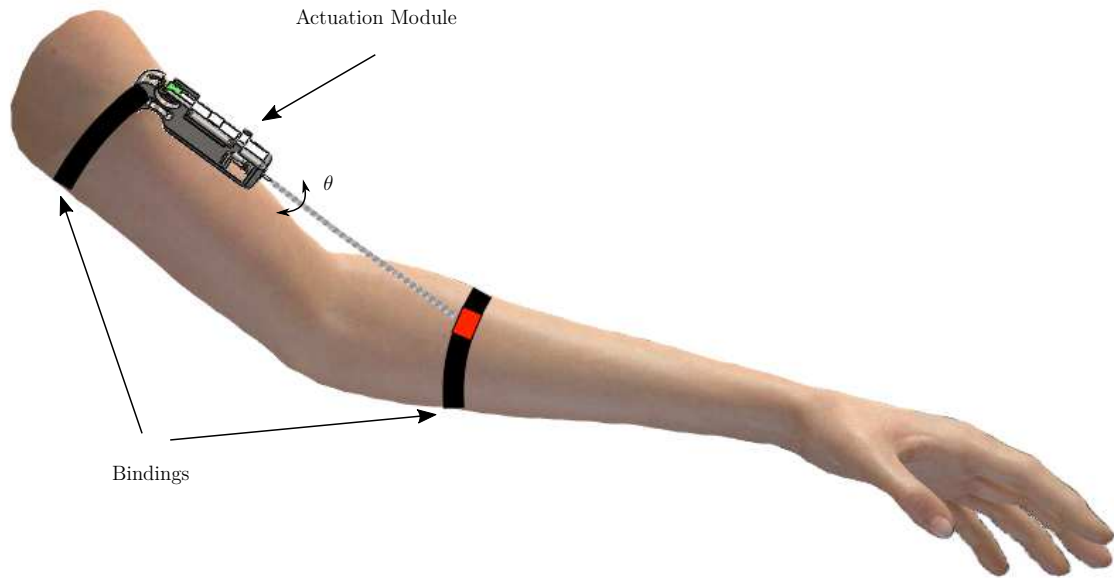


Fig. 6.2 Conceptual view of an elbow exoskeleton based on the twisted string actuation module.

This chapter is organized as follows. Sec. 7.1, describes the mechanical design of the actuation system and the working principle of the proposed force sensor and in Sec. 6.2, the force sensor calibration and experimental results are presented. Sec. 7.3 concludes with some final remarks.

6.1 System Description

A schematic view of the basic working principle of the twisted string actuation (TSA) system is represented by Fig. 6.1. A possible application of this device is shown in Fig. 7.1a, where a light exoskeleton is obtained by connecting the motor module with an integrated force sensor to the forearm of an user.

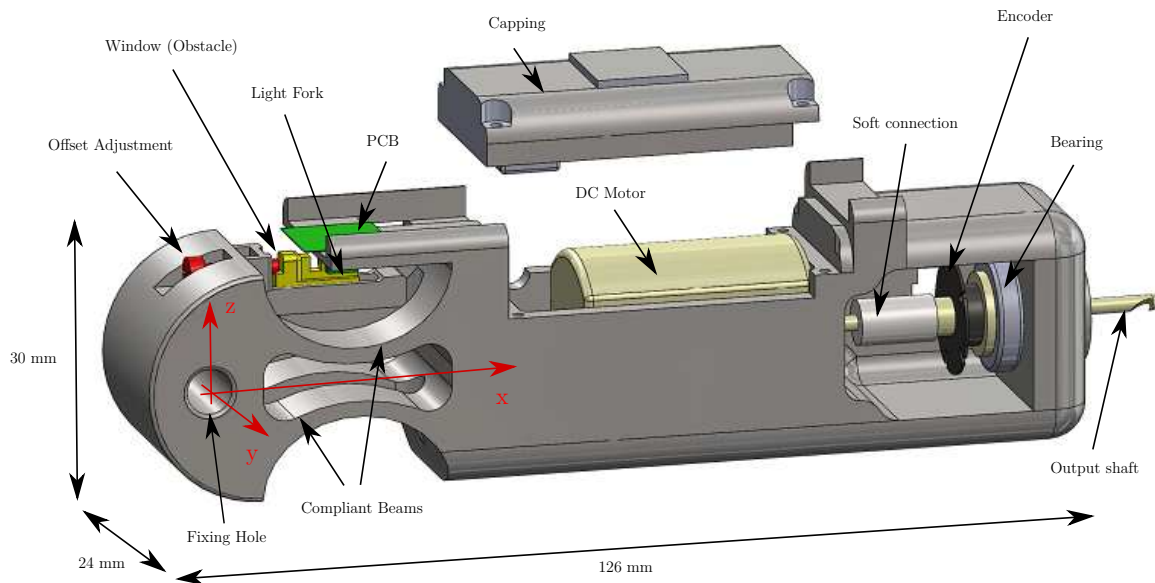


Fig. 6.3 Detail of the twisted string actuation module.

The basic concept of the twisted string actuation system has been presented in CHAPTER... A couple strings that are twisted on one end and attached to a rotative electrical motor and on the other end to the joint to be actuated comprise the transmission system. The total length of the strings is reduced by the rotation to which they are submitted by the electrical motor. This rotation also converts the rotative motion to a linear motion on the other side of the strings.

The integration of a force sensor into the actuation module is necessary to successfully measure the force which the actuators apply directly to the load. Placing the force sensor between the frame connection point on the robot structure and the actuation module is one of the possible proposed solutions. In this setup, all of the components of the actuation system are integrated, thus optimizing encumbrance. A digital interface to input and output signals required for the actuation system control can be provided by the placement of the actuator electronics, including both the motor power electronics

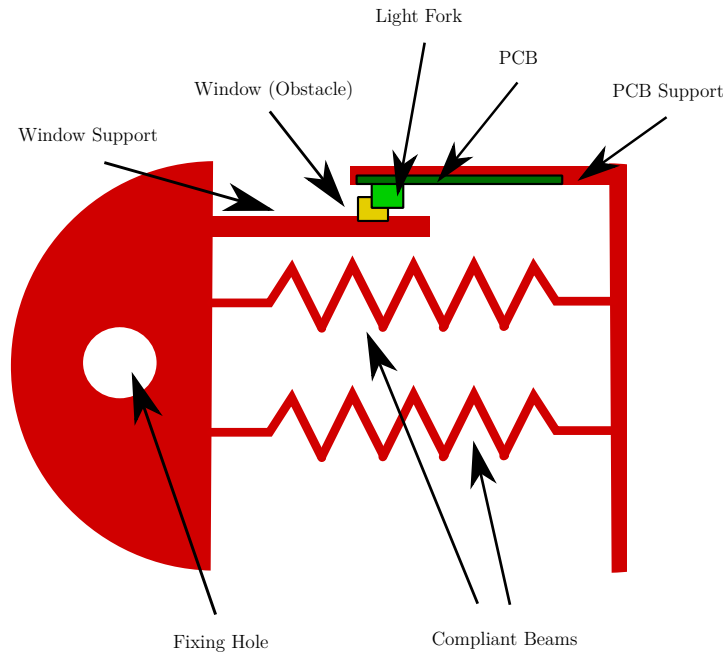


Fig. 6.4 Scheme of the sensor structure and component arrangement.

and the conditioning system for both the optical encoder and the force sensor, in a single printed circuit board.

6.1.1 TSA Module Structure

Fig. 8.4 portrays a detailed 3D view of the actuation module CAD compliant frame. A plastic ABS frame manufactured by 3D rapid prototyping composes the mechanical structure along with a pair of axial-symmetric compliant beams. These beams function as a linear spring granting a certain compliance to the structure as well as the implementation of the force sensor. A DC motor is located in this module along with an optical encoder for position sensing while the output shaft is supported by an axial bearing at the point of the twisted string connection. A silicon tube is used to join the motor and transmission shafts to provide ample flexibility in order to solve problems regarding misalignment of the rotational axes of the motor and the transmission shaft. The par-

ticular structure of the motor module consents the transmission force to be completely supported by the output shaft through a combined bearing while the motor is only used to transmit the necessary torque for driving the twisted string actuation to the output shaft.

6.1.2 Sensor Working Principle

The optoelectronic sensor is described in details in CHAPTER..., and therefore here only a brief summary of its main features is reported. The basic idea is to have a LED illuminating a photo-diode (PD), where the current flowing through the PD can be modulated by means of a mechanical component that partially intercepts the light emitted by the LED.. The position of the mechanical component depends on the deformations occurring on the sensor's body as a consequence of the application of an external force.

A finite element analysis of the sensor and actuation module is shown in Fig. 6.5, while in Fig. 6.6 some experimental data reporting the deformation of the module in response to the application of external forces are presented.

The OMRON EE_SX1108, called a light fork because of its forked structure, is the sensitive element used for the implementation of the proposed sensor. This component is embedded with both an LED and a PD (a phototransistor) facing each other and is provided with a window restricting the light cone coming from the LED to the PD to a thin and well-focused region.

Several advantages accompany the use of this component. A compact sensor implementation is permitted because both the LED and the PD are embedded together in a compressed structure with precise relative position. The light cone is well shaped, providing a very steppy and linear transition region between the fully covered and the fully free light conditions and allowing a good sensitivity and linearity to be obtained.

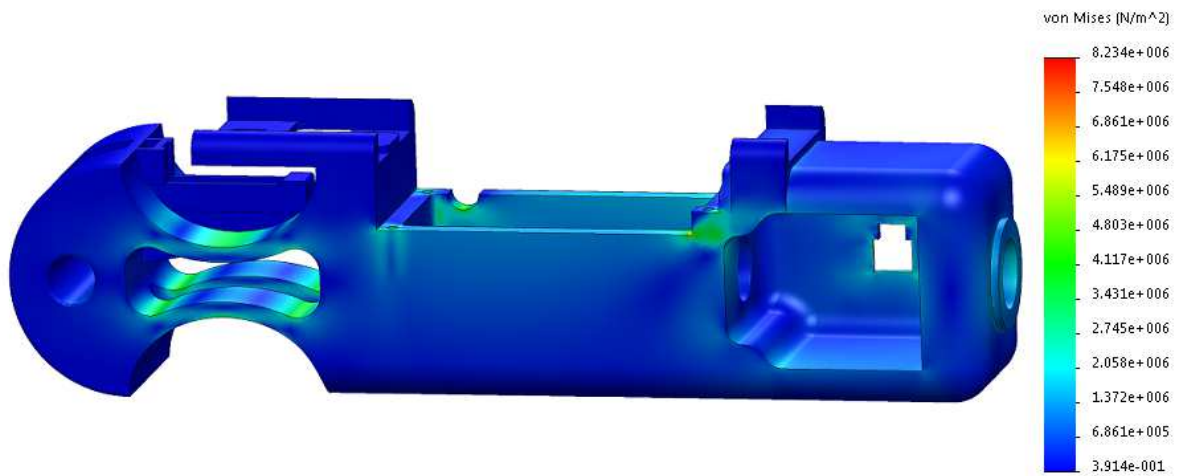


Fig. 6.5 Finite Element Analysis (FEA) of the compliant frame.

6.1.3 Force Sensor Design

Fig. 6.4 is a detailed depiction of the force sensor being designed to be added to a motor module. This force sensor is composed of two faced surfaces where the external force is applied, connected by a double beam curved structure which serves as a linear spring. These two faced surfaces have two support elements independent from the light fork, hosted by a PCB, and the obstacle, occluding the light path for the LED to the PD, attached to them to measure the linear displacement. An offset regulation mechanism comprised by a screw is also available to adjust the position of the obstacle with respect to the light fork along the measurement axis.

The relationship between the measured power and the amount of interception can be exploited to optimize the design of the force sensor in order to meet the specifications in terms of linearity and sensitivity. The proposed force sensor has been implemented following these characteristics.

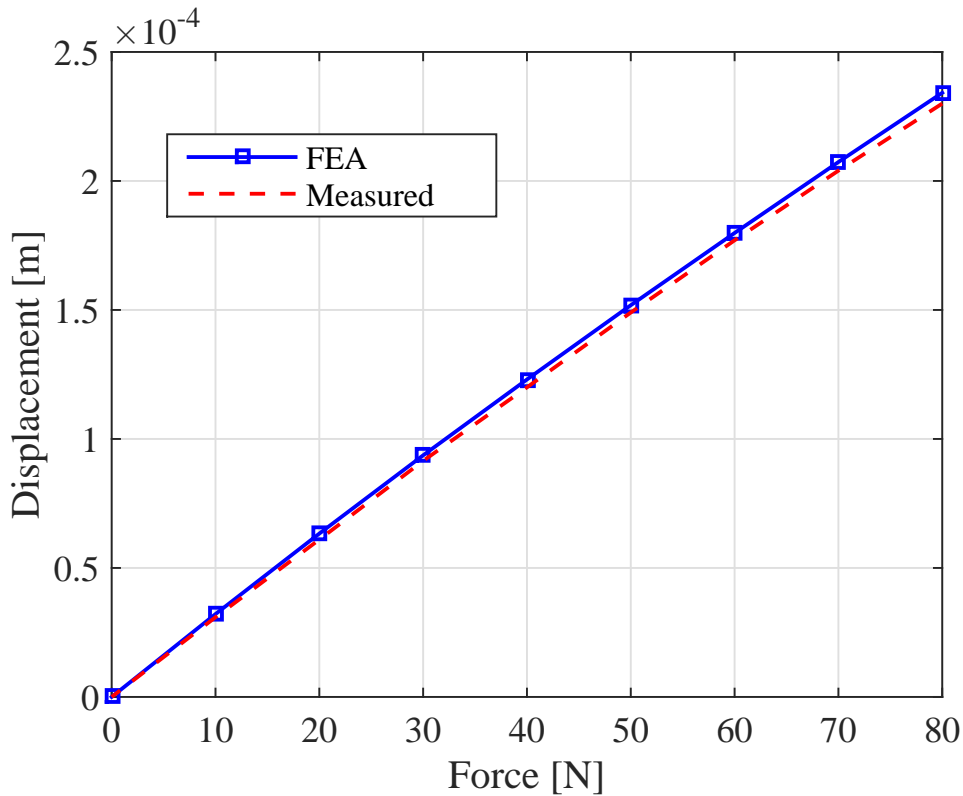


Fig. 6.6 Deformation of the motor module in the direction of the transmission: comparison between experimental values and FEA.

6.1.4 Validation of the Actuation Module Design

The actuation module structure is designed to be symmetric with respect to the axes orthogonal to the direction of the measured force (along the x axis). The mechanical structure must be compatible with the dimensions of the optoelectronic component and adequately designed to attain the linear displacement within the force range. Both experimental measurements and proper Finite Element Analysis (FEA) were used to confirm the proposed actuation module as seen in Fig. 6.5, where the maximum load condition of 80 N is applied. Fig. 6.6 portrays the comparison between the measured deformation and FEA. The result evidences that the measured deformation is slightly smaller than the FEA, which can be influenced by the manufacturing process. The maximum deformation with the maximum load of 80 N is $\Delta X_{max} \simeq 2.34 \cdot 10^{-4}$ m indicating

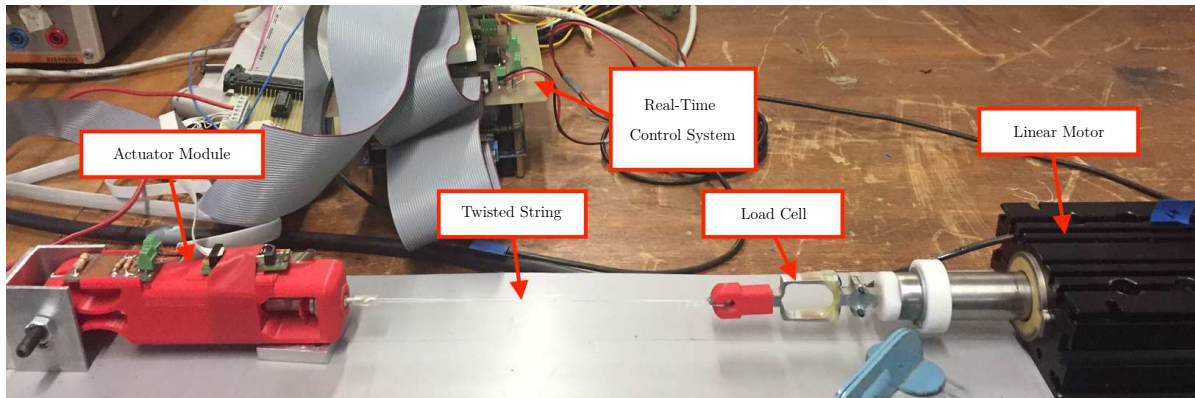


Fig. 6.7 Overview of the experimental setup.

the compliant frame deformation is within the goal working region $\Delta d < 0.2$ mm and can be considered linear.

6.2 Experimental Evaluation

In this section, the experimental evaluation of the proposed actuation module is investigated.

6.2.1 Experimental Setup

Fig. 6.7 depicts an overview of the experimental setup, used for the verification of the proposed actuation module. This setup consists of a rotative DC motor used to twist the strings aligned along the rotation axis of the motor and connected from one side to the motor output shaft and the other side to a linear motor (LinMot-37x160) to be able to apply various loads to the actuation module structure located along the motion axis of the linear motor and equipped with a load cell able to measure a maximum force of 100 N and an integrated encoder with resolution of $1 \mu\text{m}$ to measure the load position. A protected cable for noise rejection connects the load cell to the amplifier.

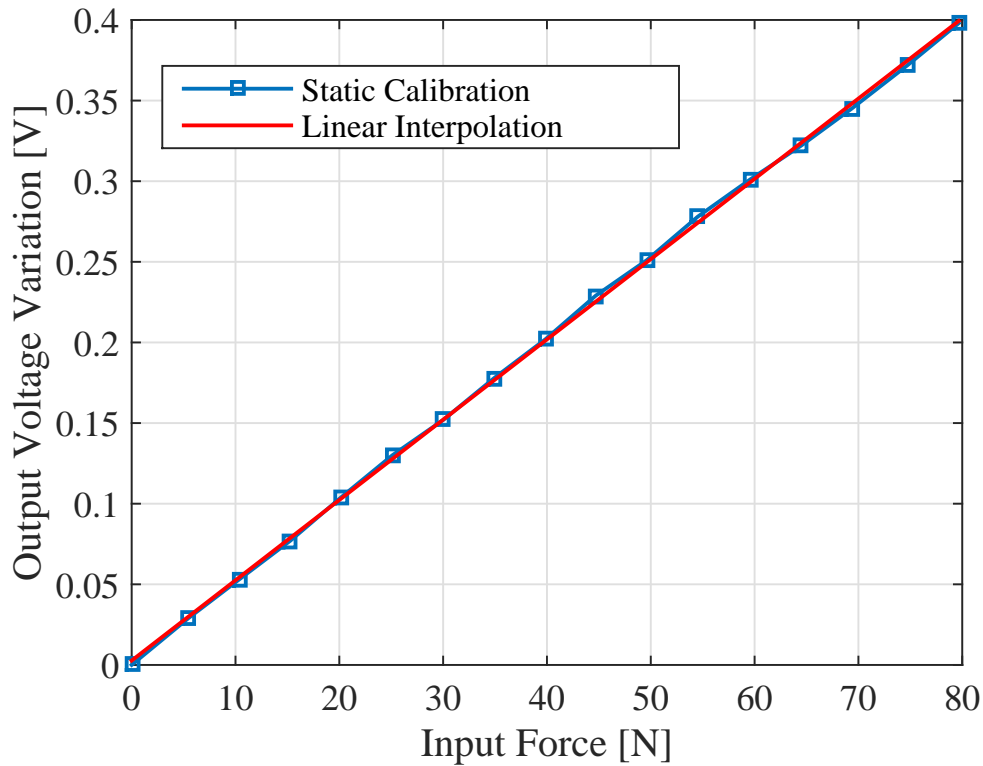


Fig. 6.8 Static Calibration.

The linear motor is driven by a low-level control system to apply different force profiles to compensate for the friction acting on the motor slider [16]. The DC motor is placed into the motor module with an integrated force sensor, position sensor and motor power electronics. Data collection and control of the system during the experiment are managed by a PC-104 running RTAI-Linux real-time operating system and a sensoray 526 data acquisition board.

In order to apply different forces to the actuation module during the experiment, the actuation module is mechanically being fixed from one side and the other side is connected by twisted strings to the load cell mounted to the slider of the linear motor.

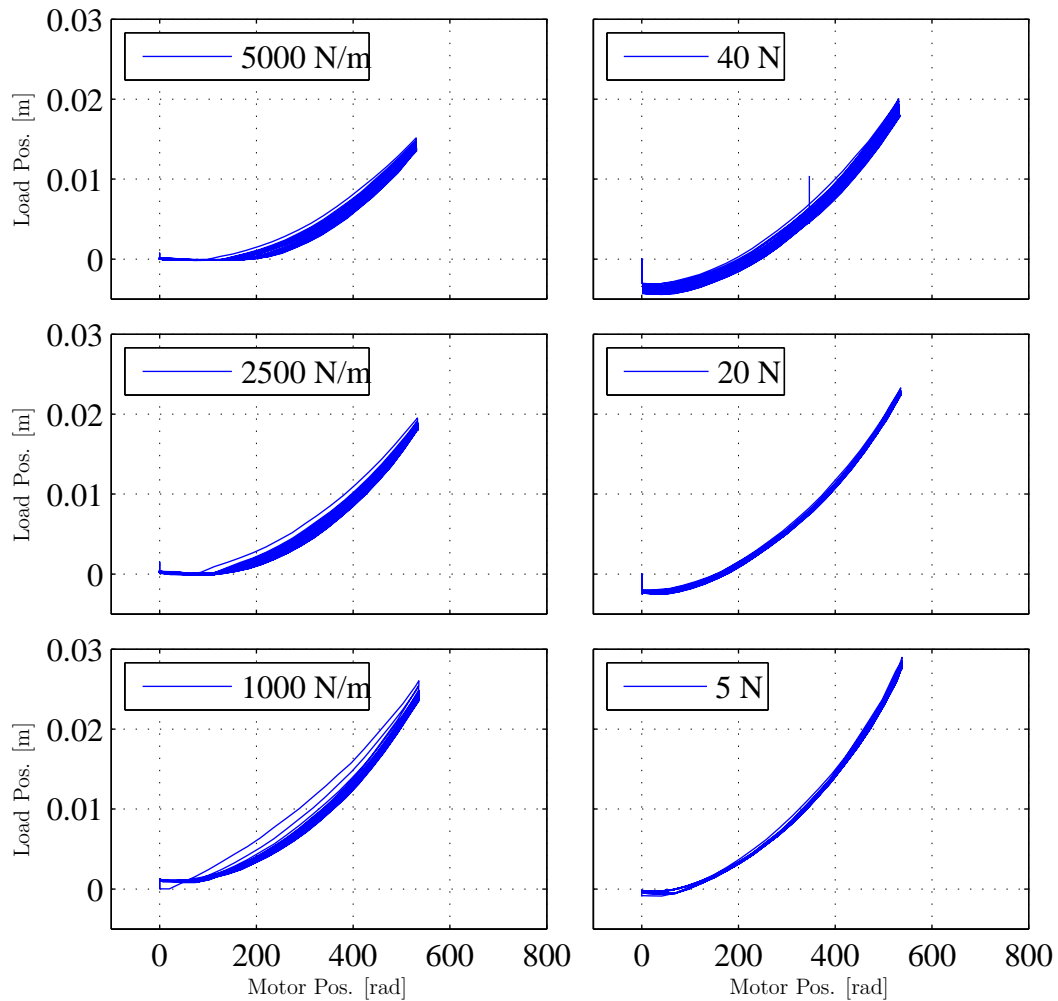


Fig. 6.9 Input output position characteristic with constant load (right) and with spring-like load (left).

6.2.2 Force Sensor Calibration

A static calibration experiment was performed to calibrate the integrated force sensor through the utilization of a load cell attached to the linear motor as a reference sensor. The calibration curve is acquired through the application of various loads up to the maximum value of 80 N to the motor module through the measurement of the corresponding output voltage V_O using the conditioning circuit displayed in Fig. 5.4. The resulting calibration plot is depicted in Fig. 6.8. The experimental measures are compared with a

suitable linear interpolation to evaluate sensor linearity. The results demonstrate that the maximum linearity error of the proposed force sensor is 0.95% and its sensitivity is about 5 mV/N. As visible in Fig. 6.8, the prevention of any amplification of the sensor output is prevented by the range of the output voltage V_O .

6.2.3 Input-Output Characteristic

To evaluate the input-output characteristic of the system, further experiments have been performed.

At the first experiment, the linear motor is initially programmed to apply a constant reference force of 5, 20, 40 N to the actuation module, and the rotative motor is then programmed to move with a trapezoidal trajectory from the initial zero position (untwisted string) to a maximum value of 540 rad and the load position is then measured.

Different conditions of the load have been carried out in the second experiment. The linear motor is programmed to act as a mass-spring-damper system with the load stiffness of 1000, 2500 and 5000 N/m. Fig. 6.11 presents the Input-Output position characteristic of the proposed actuation module with constant load (right) and spring-like load (left). The load position visibly decreases as the input load increases.

6.2.4 System Responses

Two experiments with different force input conditions have been performed to prove the behavior of the proposed actuation system properties in a dynamic environment. A force feedback loop based on the data gathered from the load cell mounted on the slider of the linear motor controls the force applied to the actuation module with the linear motor.

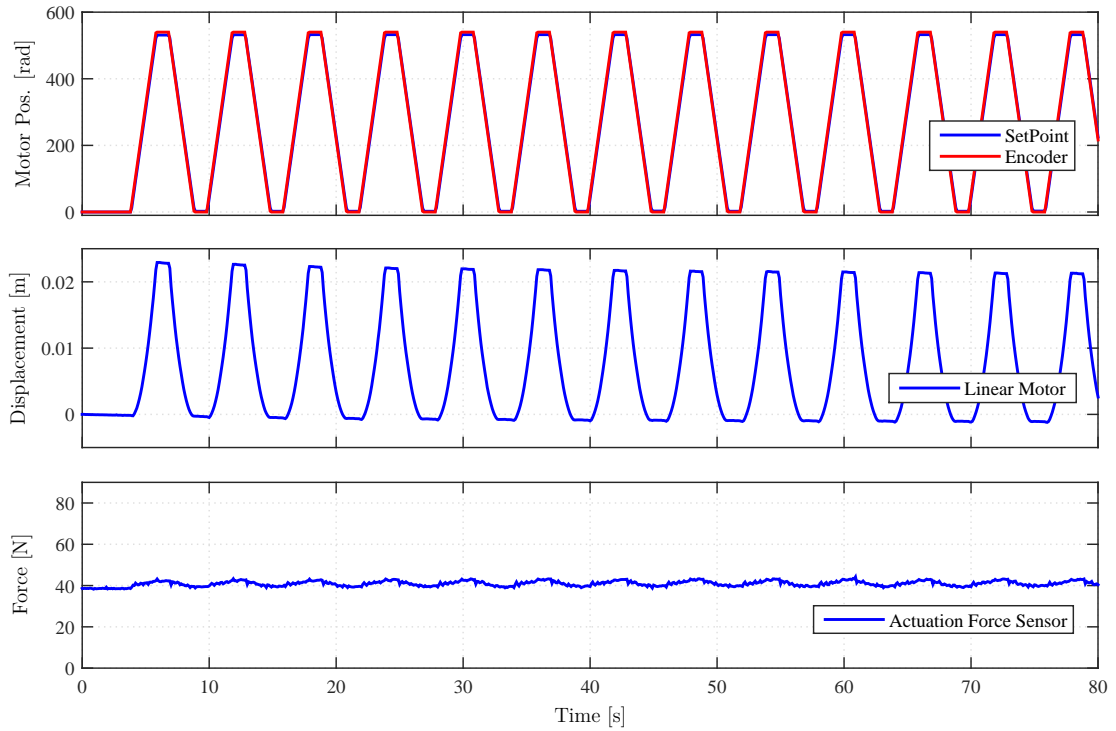


Fig. 6.10 Experimental evaluation of the constant load

Fig. 6.10 demonstrates the results of an experiment where rotative motor is programmed to rotate from untwisted condition (i.e. $\theta = 0$) to a maximum value of 540 rad with a trapezoidal trajectory while the constant load of 40 N is applied to the motor module by linear motor. In Fig. 6.10, the upper plot indicates the tracking responses of the string twisting angle and the angle setpoint, while the middle plot shows the load position. The lower plot reports the force measured by the by the force sensor integrated in the actuation module.

Fig. 6.11 portrays an experimental result with the input load stiffness of 5000 N/m while the rotative motor is programmed to rotate with a trapezoidal trajectory from untwisted condition to a maximum value of 540 rad.

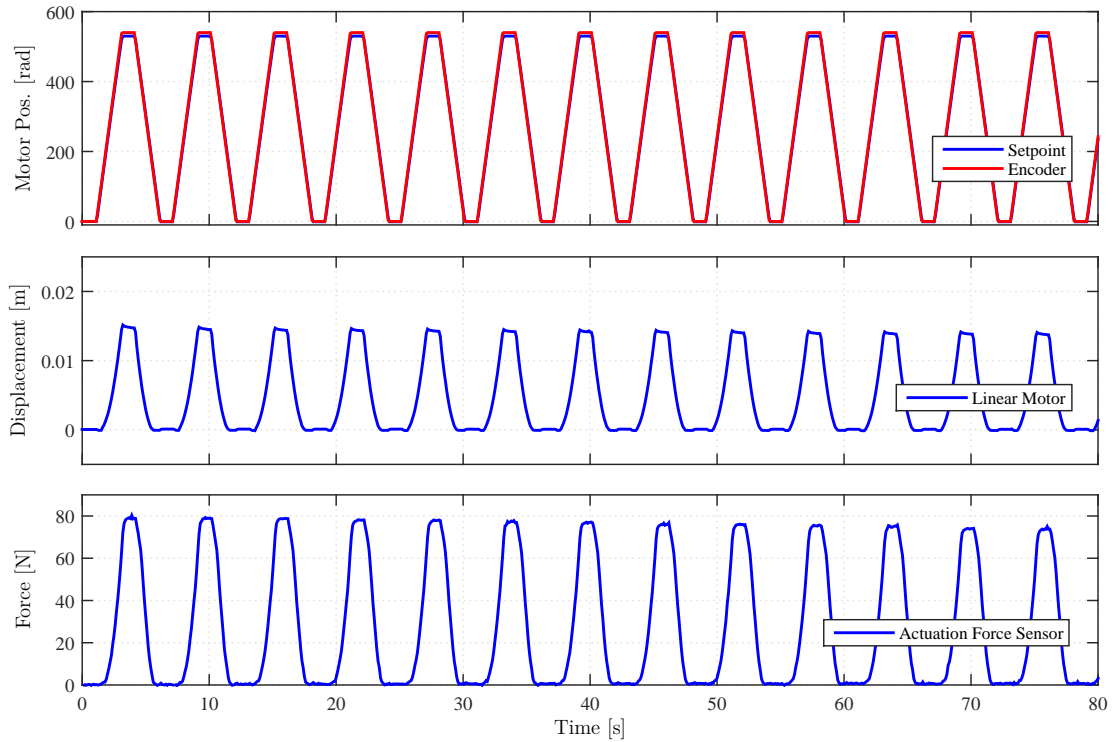


Fig. 6.11 Experimental evaluation of the Spring-like load

6.3 Conclusions

This chapter presents an innovative twisted string actuation module system with an integrated force sensor which can be used for diverse robotic applications. The proposed actuation module structure, the integrated force sensor and the basic sensor working principle are discussed. To check the actuation module compliant frame, a finite element analysis (FEA) together with experimental measures has been performed and the results have been compared. The calibration of the force sensor has also been performed statically and the data have been reconstructed from the sensor output by means of a suitable linear interpolation and the results show a satisfactory fit between the reference force and the sensor output with a linearity error of 0.95% and a sensitivity of about 5 mV/N. Different experiments have been carried out to verify the properties of the

proposed actuation module system. The experimental results prove that the proposed actuation system is sufficient to be used for different robotic applications.

Chapter 7

A Wearable Robotic Device Based on TSA

In more recent years, the use of exoskeletons for the hand and lower/upper-limb support applications has drastically increased [31, 32, 52]. In [53], an upper-limb power-assist exoskeleton by pneumatic muscle actuation with two metal joint was developed. An integrated cable-driven, low-cost and light-weight wearable upper body orthotics system that can be worn over the upper body to generate effective torques to move the arm through a set of assistive motions was introduced in [54]. In [55] a wearable upper body exoskeleton system incorporating a model-based compensation control framework to assist robot-aided shoulder-elbow rehabilitation and power assistance functions is presented. An anthropometric seven degree-of-freedom powered exoskeleton for the upper limb based on a database defining the kinematics and dynamics of the upper limb during daily living activities is presented in [56]. In [57], a cable-driven arm exoskeleton (CAREX) was developed to achieve desired forces on the hand, i.e., both pull and push, in any direction as required in neural training while a 6-DOF upper-limb exoskeleton



(a) A light-weight assistive device mounted on the shoulder of the user.



(b) A light-weight assistive device mounted on the back of the user.

Fig. 7.1 Conceptual view of an elbow exoskeleton based on the twisted string actuation module.

robot [58] and a muscle suit with providing human physical support was developed in [59].

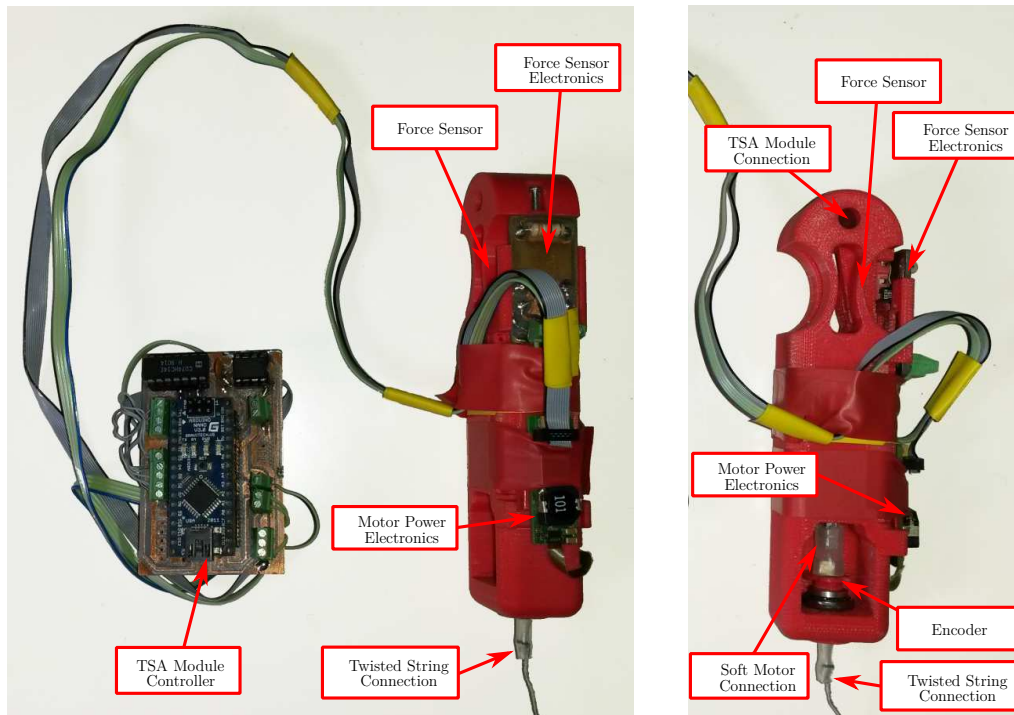
In this chapter, the design of a novel Twisted String Actuation (TSA) module is presented. The main purpose of this device is the development of wearable assistive and rehabilitation systems. Due to its particular structure, TSA is well suited in case the force is directly applied to the user's limbs, without external rigid structures supporting the limb and/or the actuation, as schematized in Fig. 7.1b. The design of the proposed wearable assistive and rehabilitation system aims to: i) remove all rigid joints to have

a lighter and more comfortable system, that can be easily adapted to any user; ii) decrease the weight, size and mechanical complexity of the exoskeleton, avoiding complex regulation mechanisms, to reduce the costs and improve its reliability and affordability; iii) design a modular actuation system that can be reused for implementing different assistive movements. The proposed TSA module is characterized by an integrated force sensor and embedded acquisition and control electronics.

This chapter is organized as follows. Sec. 7.1 describes the mechanical design of the TSA modules and the working principle of the integrated force sensor. In Sec. 6.2 the force sensor calibration and the experimental evaluation of the TSA module are presented, while in Sec. 7.2 the results about the use of the proposed device for the an assistive application is reported. Finally, Sec. 7.3 draws the conclusions and outlines future research activities.

7.1 System Description

The designed system is conceived for rehabilitation and assistive applications, as schematically reported in Fig. 7.1, where a light assistive device is obtained by mounting the TSA module with integrated force sensor on a orthopedic shoulder support strap (see Fig. 7.1a), to allow the TSA to work in a biarticular configuration [60], providing help on the whole arm and not on the elbow only. And Fig. 7.1b shows a TSA system mounted on the back of the user and connected to a forearm through a shoulder path (see Fig. 7.1b). The designed TSA module fits very well with this kind of application due to its light and compact structure and the ability of acting similarly to human muscles, as will be shown in the experiments described in Sec. 7.2.



(a) Upper view of the TSA module prototype.

(b) Lateral view of the TSA module prototype.

Fig. 7.2 Detailed view of the TSA module prototype and control electronics.

7.1.1 TSA Module Design

A schematic view of the designed TSA module is reported in Fig. 6.1. With reference to this picture, the TSA module is composed, from left to right, by: i) a connection element to connect the module to the supporting frame; ii) the force sensor to measure the actuation load; iii) a frame hosting the DC motor, the output shaft where the twisted strings are connected and all the electronics; iv) the twisted string itself connecting the motor module with the load, and the load itself represented in Fig. 6.1 as a translating mass. The basic TSA concept and modelling can be found in [9]. A couple of strings are attached to a rotative electrical motor and twisted on one end, whereas on the other end the strings are connected to a linear moving element, i.e. the load. The overall string length is reduced by the rotation produced by the electrical motor. Therefore, the

rotative motion of the electric motor is converted to a linear motion on the other side of the strings.

Figure 8.4 reports a detailed 3D view of the TSA module design. Its mechanical structure is manufactured by rapid prototyping in ABS plastic. A pair of axial-symmetric compliant beams has been integrated in the TSA module frame on the opposite side with respect to the twisted strings. These beams behave as a linear spring, granting a properly designed compliance to the structure, required for converting the force exerted by the TSA module into a proper frame deformation and thus to the implementation of the force sensor. The integration of a force sensor into the TSA module is of paramount importance to successfully measure the force the actuator applies to the load. In the proposed TSA module, the force sensor is located in between the frame connection point on the robot structure and the frame hosting the DC motor, i.e. on the opposite side of the twisted strings with respect to the rotative motor, as can be seen in Fig. 8.4. A picture of the TSA module prototype developed in this work is reported in Fig. 7.2. In particular, Fig. 7.2a shows also the TSA module embedded controller based on an Arduino NANO board. In the TSA module, an optoelectronic device is then used to detect the frame deformation and convert it back to the applied force causing the deformation. As shown in Fig. 7.2, a DC motor is hosted in the module frame along with an optical encoder for motor angular position sensing, while the output shaft is supported by a combined axial-radial bearing at the point of the twisted string connection to both reduce the friction and prevent the transmission force to damage the motor. A silicon tube is used to connect the DC motor and the module output shafts in order to solve problems related to misalignments of the rotational axes of the motor and the module output shaft. The designed TSA module structure allows the transmission force to be completely supported by the output shaft through the combined bearing, whereas the motor is only used to transmit the necessary torque for driving the twisted string actua-

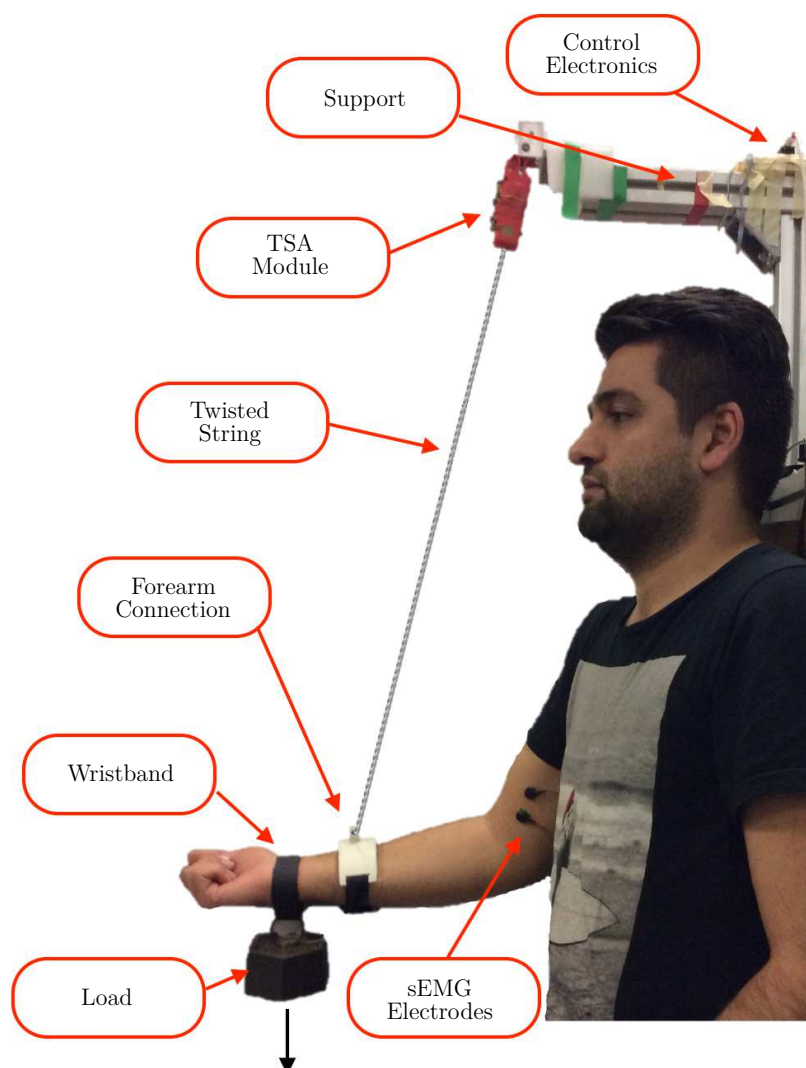


Fig. 7.3 Overview of the experimental setup.

tion to the output shaft. In this setup, all of the components of the actuation system are integrated in a single element, thus optimizing the system encumbrance. A digital interface to input and output signals required for the actuation system control is provided by the actuator electronics, including both the motor power electronics, the conditioning system for both the optical encoder and the force sensor and a microcontroller board for controlling the TSA module (see Fig. 7.2). The communication of the TSA controller with external systems can be implemented both with UART, SPI or I2C interfaces.

7.2 Experimental Evaluation of the TSA Module as an Assistive Device

To show the effectiveness of the proposed system for rehabilitation and assistive applications, the TSA module has been tested on a user as a support to the biceps muscle activity during a load lifting task. In particular, in this test application, sEMG has been used to drive the assistive device. As a preliminary step toward the implementation of an elbow flexion/extension assistive system, in which considered the installation of the device on the back of the user, see Fig. 7.1b, the TSA module has been fixed to a rigid structure, see Fig. 7.3, to simplify the experimental test, in order to use the necessary string length without considering friction and curvature related phenomena introduced by the twisted string path across the shoulder, as can be seen in Fig. 7.1b. To solve this issue, dedicated experiments to study the effect of friction on the TSA transmission characteristics are under development [61]. In this preliminary experimental evaluation, the TSA module operates on the user's forearm and is regulated using a variable stiffness control approach. In this relation, the biceps sEMG signal is used within a specific PI (Proportional-Integral) control scheme in order to suitably adjust the device stiffness to obtain a load partial compensation, limiting the sEMG activity under a suitable threshold value.

7.2.1 Hardware and setup overview

The experimental setup used during this experiment is shown in Fig. 7.3. With reference to this picture, a rigid structure has been implemented to allow the TSA module be firmly fixed in a point above the user's shoulder, such that the string can be in tension with respect to its full length. In particular, the length of the string for this experiment has

been chosen equal to 1 m, in order to exploit the mechanism contraction range related to the best module working condition, that is the 20% of the full string length [9]. The string is therefore connected to an armband fixed on the forearm of the user.

The sEMG signal has been acquired by means of low-cost disposable surface electrodes connected to the acquisition board Cerebro [62]. The sEMG signals are acquired by a high-performance Analog Front End (AFE) [63] that is connected with an ARM Cortex M4 Microcontroller. In this application, the data are sampled at 1 kHz and streamed to a nearby PC using an onboard Bluetooth interface. Before using the sEMG signals in the TSA variable stiffness control scheme, a processing step is necessary. The following filtering procedure is applied to the signals [64]: i) a 50 Hz notch filter for powerline interference cancellation, ii) a 20 Hz high-pass filter, iii) the rectification (absolute value of the signal) and finally iv) the Root Mean Square (RMS) value is computed on a 200 ms window.

7.2.2 Experiment Configuration, Control Scheme and Results

A healthy male subject is involved in the experiment. In particular, the user put on the TSA module, which is connected to the rigid structure and, on the other string end, to the armband fixed to his forearm. During the experiment, the subject is sat in a normal and comfortable position, holding his upper arm parallel to the trunk. A couple of differential sEMG electrodes have been placed in proximity of the biceps brachii muscle in the upper arm, referring to methods and best practices outlined in [65]. In this validation test, the goal is to assist the biceps during the flexion of the elbow for lifting tasks of a load of 2 Kg applied on the wrist. For this reason, only the biceps sEMG activity is acquired, considering negligible the triceps activation. Specifically, the subject is required to perform five consecutive forearm motions, each one consisting in a

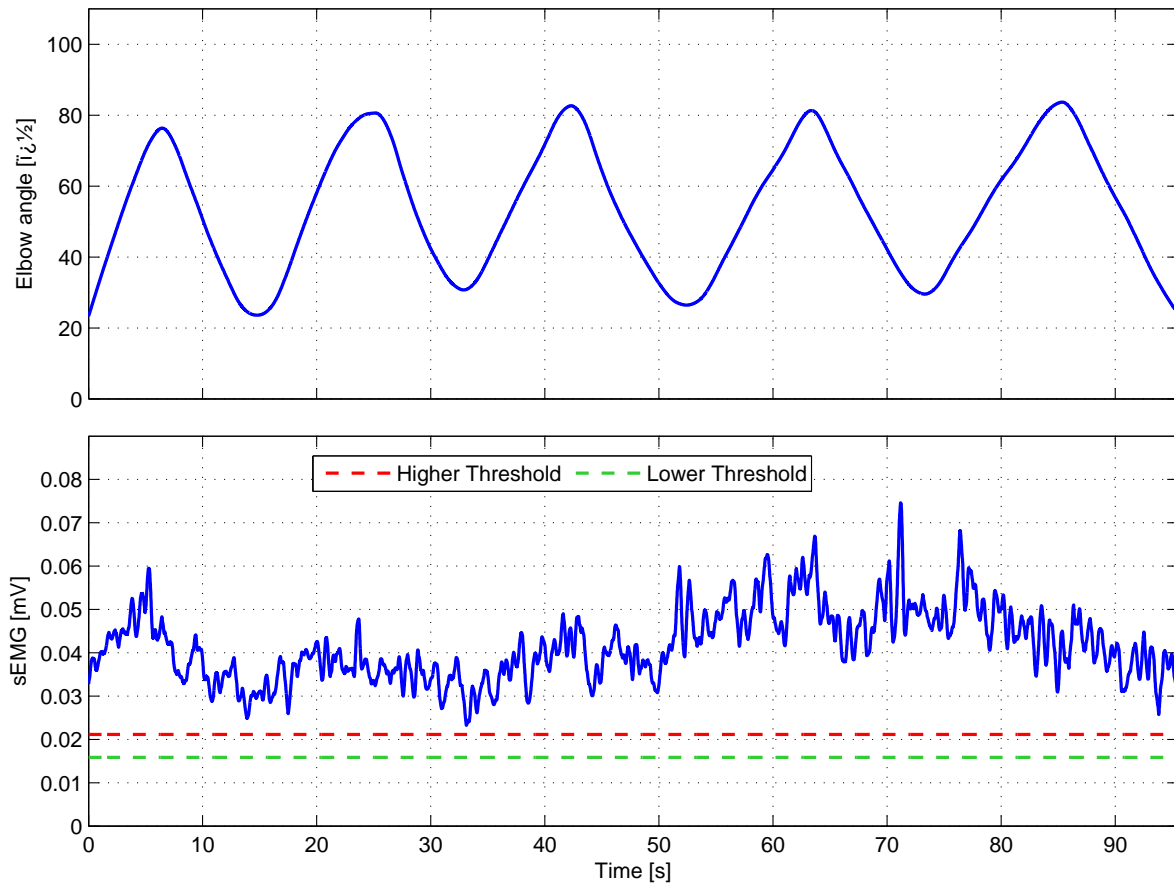
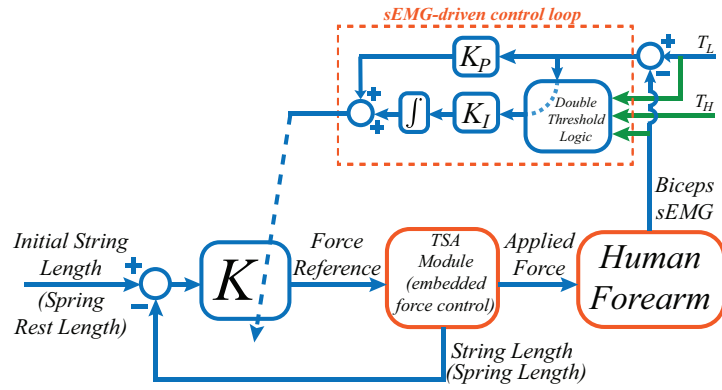


Fig. 7.4 Plots for the lifting task without the assistive device support.

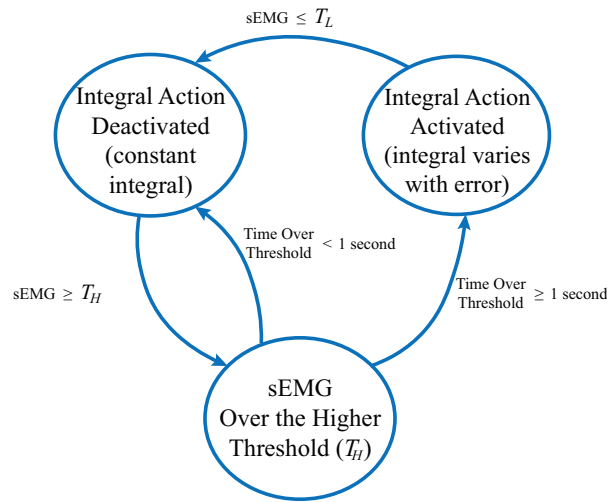
flexion followed by an extension, covering the elbow angle range between approximately 10° and 90° . The user is also requested to perform the movements smoothly and with a reasonably low velocity. Once the 2 Kg load is applied to the forearm by means of a wristband, in the first part of the experiment the user executes the flexion/extension motions freely, without the help of the TSA module. The behaviour of the biceps activity during this task can be observed in Fig. 7.4 looking at the acquired sEMG signal and where the elbow angle is computed from the module's DC motor encoder signal and the setup geometry. In the second phase of the experiment, the subject connects his forearm to the TSA module in order to be assisted during the lifting task of the 2 Kg load. To achieve this goal, the TSA module is controlled through a specific sEMG-driven control scheme illustrated in Fig. 7.5a. With respect to this figure, a stiffness

control is implemented for the TSA module, which means that the device is regulated in such a way to behave like a spring with stiffness K and contraction given by the difference between the actual string length (spring length) and an initial string length less or equal than the length in the case of an elbow flexion of 90° (spring rest length). This is achievable because of the possibility to calculate the string length from the DC motor's encoder signal, and thanks to the presence of a force control loop embedded on the TSA module. In particular, such lower-layer controller uses the force sensor measurement within a standard Proportional-Integral-Derivative (PID) control loop in order to track the requested reference force value. Therefore, in this way, the assistive device is equivalent to a spring attached on the user's forearm and the way it interacts with the human is determined by the value of K . Based on this observation, in our control scheme the value of K is determined by a sEMG control loop, that makes use of a PI controller modified according with a double threshold logic whose functioning is observable in Fig. 7.5b.

In detail, the controller is based on a sEMG error between the measured biceps sEMG signal and lower sEMG threshold, the latter used as reference value. The proportional action of the PI controller (identified by a properly chosen proportional gain K_P) continuously takes as input the sEMG error. On the other hand, the integral action (characterized by a properly chosen integral gain K_I) is activated only when the sEMG signal is continuously over a higher threshold for a period of 1 s, until the increasing of the stiffness K of the TSA module makes the sEMG signal touching the lower threshold value. Such double threshold logic has been implemented because of two considerable advantages: i) a more reliable regulation of the sEMG signal (which presents a substantial inherent variability), with respect to a single reference value approach and ii) the capability of filtering sEMG peaks that surpass the higher threshold for less than 1 s, which are usually present in case of slightly faster motions or unwanted impulsive



(a) Control scheme.



(b) Double threshold logic behaviour.

Fig. 7.5 Variable stiffness control scheme of the TSA module for the assistive application.

contractions, avoiding an increasing of the integral action not oriented to compensate the applied load. Furthermore, the threshold values are determined for the subject by means of a simple calibration phase. In particular, the sEMG signal of the user with the elbow flexed at 90° and with a load of 0.5 Kg is recorded. Then, denoting the thresholds as T_L and T_H , they are computed as

$$T_L = m_{EMG} - \sigma_{EMG}$$

$$T_H = m_{EMG} + \sigma_{EMG} ,$$

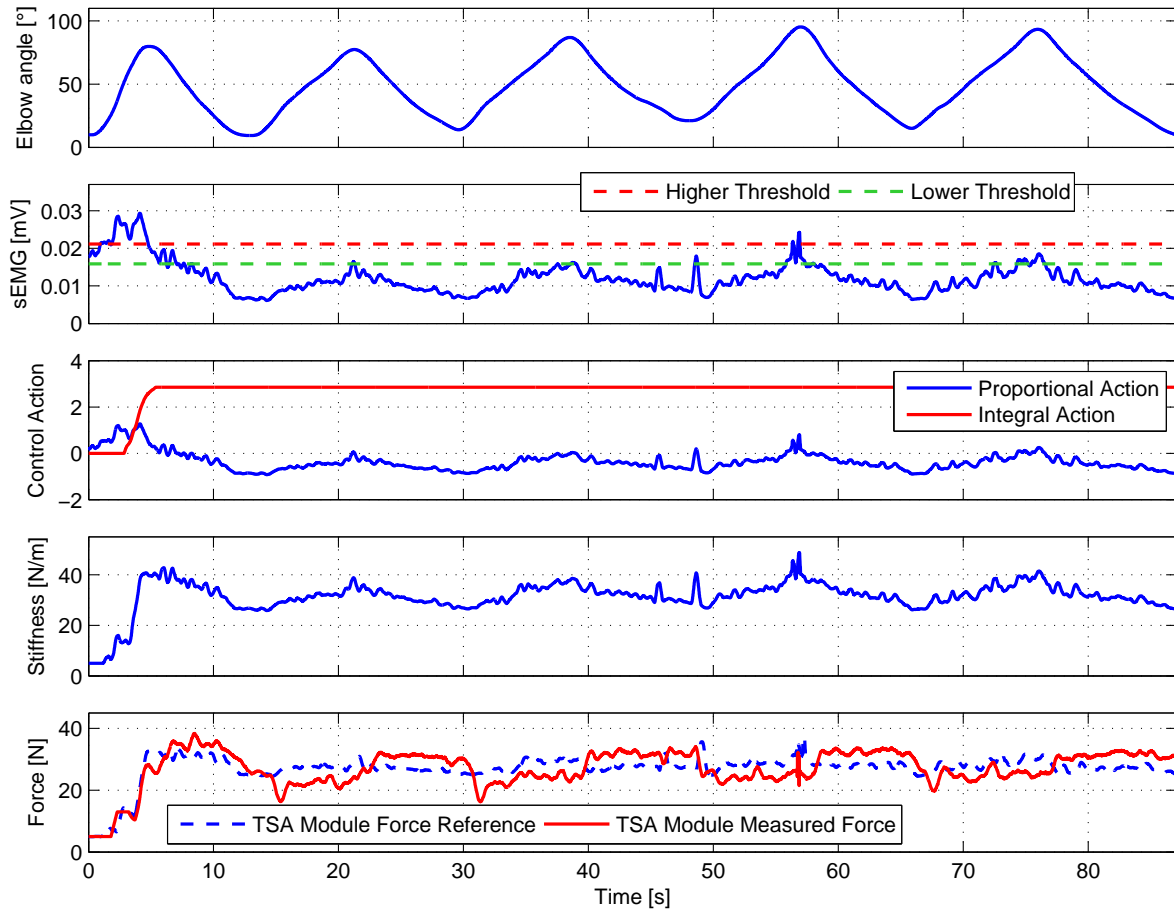


Fig. 7.6 Plots for the lifting task with the assistive device support.

where m_{EMG} is the mean value of the sEMG calibration recording and σ_{EMG} is the standard deviation computed over the same recording. The effects of this control strategy during the lifting task of the 2 Kg load by the user with the TSA module support are shown in the graphs of Fig. 7.6. In particular it is possible to observe how the sEMG initially goes over the higher threshold (red), causing the activation of the sEMG controller integral action after one second. This makes the stiffness of the TSA module rapidly increase in such a way that the biceps sEMG activity decrease until it reaches the lower threshold (green). Then, for the subsequent flexions of the lifting task, the sEMG remain in the neighborhood of the lower threshold without surpassing the higher threshold except for peaks that are successfully filtered by the implemented double

threshold logic, which means that the integral action is not activated in these cases. In other words, this means that the biceps exerts a muscular activity that never surpasses the sEMG value corresponding to the 0.5 Kg calibration recording, saving a quantity greater or equal to 1.5 Kg-related muscle effort. On the light of this and, especially, comparing the sEMG values during the lifting of the 2 Kg load in the case with no support (Fig. 7.4) and with support (Fig. 7.6) the effectiveness of the TSA module as an elbow assistive device is proved.

7.3 Conclusions

This chapter presents an innovative wearable TSA module system with integrated force sensor which can be used for rehabilitation and assistive robotic applications. The proposed TSA module structure, the integrated force sensor and the basic sensor working principle are discussed in this chapter. To validate the TSA module compliant frame, the FEA has been compared with experimental measures. Different experiments have also been carried out to verify the properties of the proposed TSA module.

Furthermore, to show the capabilities of the proposed TSA module in a real assistive applications, an experiment involving a male healthy subject has been carried out, where the TSA module has been used to provide load compensation to the user's elbow joint during lifting tasks of a 2 Kg load. The experimental results show that the device, together with a suitable control scheme, can be successfully used to help and limit the user's biceps muscle activity during dynamic motions when a load is applied in proximity of the wrist.

Future work will be devoted to the installation of the module on the back of the user, in order to obtain a wearable elbow assistive device and to the implementation

of a sEMG-driven control scheme that makes use of both biceps and triceps, exploiting antagonistic muscle activation concepts.

Chapter 8

A Haptic Interface based on TSA

Applications involving remote interaction with both virtual and real environments require the availability of adequate human-machine interfaces (called haptic interfaces) able to provide the operator a feeling of telepresence, intended as the ideal of sensing sufficient information, and communicating this to the human in a sufficiently natural way that she feels herself to be physically present at the remote site [66].

Many researchers have proposed haptic devices using serial and parallel mechanisms. A Gimbal-based parallel device has been presented in [67] (floating actuators) and [68] (non-floating actuators). In [69] a solution composed by a center handle connecting four commercial *Phantom Omni* devices is proposed in order to provide 6 DoF force feedback while two 3 DoF parallel structures connected with a steering handle are presented in [70]. A joystick-like general purpose haptic interface is discussed in [71]. The device proposed in [72] adopts a separable structure composed by lower and upper parallel mechanisms and it's specifically meant to address teleoperation of mobile manipulators.

Several commercial solutions are also available on the market. The most widely used haptic interface is probably the *Phantom Omni*[®] presented in [73] and commercialized

by *Geomagic*® under the name *Geomagic Touch* (formerly Sensable Phantom Omni) [74]. The device is characterized by a 6 DoF serial kinematic chain and provides force feedback only in 3 DoF. The same company also produces an high-end research device called *Phantom Premium*. Force Dimension [75] produces two series of haptic devices with parallel structures (*omega.x* and *delta.x*) and a 7 active DoF device, *sigma.7* with an extra force feedback DoF for grasping. The *Novit Falcon* [76] is a low-cost version of *omega.3* meant to target the game industry but widely used also in research. The *HapticMaster* by MOOG [77] is the only admittance controlled haptic interface on the market.

Maglev 200 from *Butterfly Haptics* [78] is the only commercially available haptic interface based on the principle of Lorentz magnetic levitation.

The cost of standard commercial haptic devices characterized by serial kinematic chains is usually high because of the complex mechanical structure. Other drawbacks of such configurations are high inertia and reduced workspace. In most cases master devices are too heavy and not manipulable enough to allow effective usage [79]. Ideally a master device is supposed to have very low inertia while maintaining the ability to behave very stiffly, allowing a realistic reconstruction of the forces experienced by the slave robot. Cable-based interfaces are promising candidates to solve related to workspace limitations, inertia and cost, at the expense of limited stiffness. The cable transmission principle allows the actuators, which have a non-negligible mass, not to contribute to the end-point inertia providing a considerable force-weight ratio. The usage of cable transmissions is not a new concept in haptic interfaces design, as some wire-based haptic displays have been proposed in the literature. In [80] a wearable haptic interface based on parallel wires in an under-actuated configuration is presented. The discussed device is addressed to blind people and it is the basis of the development of the three-cable haptic interface presented in [81]. A 4-wire driven 3-DoF planar haptic device is proposed in [79], while

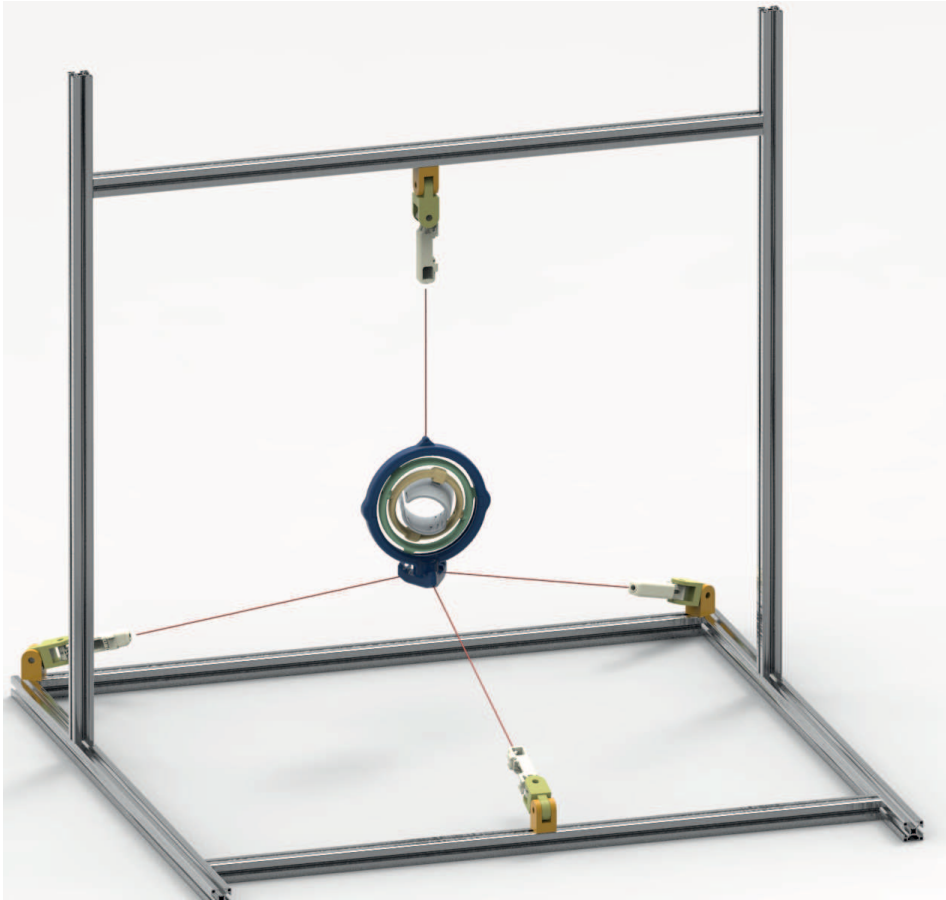


Fig. 8.1 CAD rendering of the proposed haptic interface.

in [82] a 4 strings 3D spatial interface is presented. Over-actuated solutions for 6 DoF with 9 and 8 strings are proposed respectively in [83] and [84]. The advantages of such a configuration are low-inertia, low-cost, and high safety.

In this chapter, an haptic interface based on Twisted String Actuation (TSA) is proposed. The Twisted String Actuation (TSA) [9, 85] represents a very interesting solution for the implementation of very compact, lightweight and low cost linear transmission system for highly-integrated mechatronic devices, such as haptic interfaces. TSA has been already successfully used for the implementation of different robotic devices like robotic hands [86] and [87], exoskeletons [12] and tensegrity robots for space applications [88].

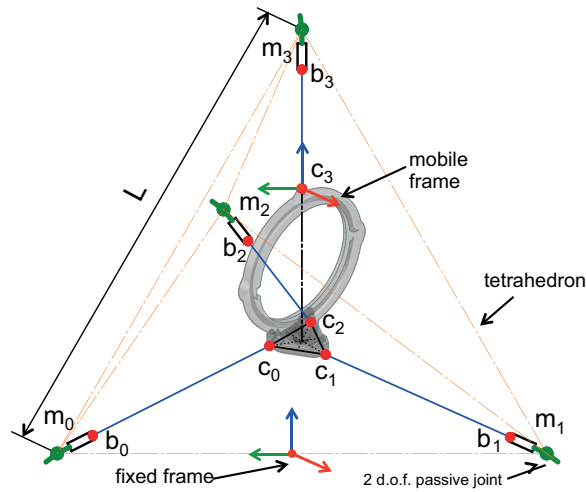


Fig. 8.2 Schematic view of the haptic interface and actuators arrangement.

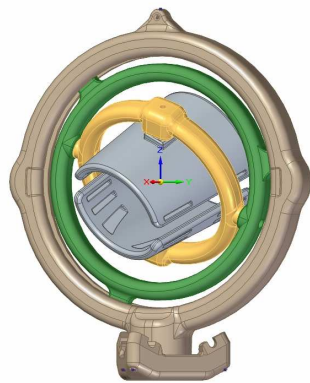
The proposed haptic interface, which conceptual design is reported in Fig. 8.1, is driven by four TSA modules arranged on the vertex of a tetrahedron, as depicted in Fig. 8.2, allowing to render linear forces along the 3 dimensions of the Cartesian space.

The chapter is organized as follow: Section 9.1 describes the overall structure of the proposed device. Section 8.1.2 describes the design of the TSA motor module. The final Section concludes with some guidelines for further developments.

8.1 System Design

8.1.1 Overall System Description

The main idea is to design an haptic interface able to move freely under the intention of the operator and at the same time apply reaction forces in the Cartesian space along the three linear directions. The device can be used as mean to control a remote robot and feed the interaction forces of the tele-manipulated robot directly to the user body. The connection between the haptic device and the human is implemented by means



(a) CAD view of the bracelet.



(b) CAD view of the cable-based actuators and its connections.

Fig. 8.3 Using ropes in transmission systems in ancient time.

of a bracelet (Fig. 8.3a) that is fasten to the user forearm. A set of three gimbals, one mounted on the other with orthogonal pivot axes forming a Cardan suspension, are driven by four cable-based actuators, see Fig. 8.2 and 8.3b, allowing the user to change freely the orientation of the forearm without affecting the force exerted by the actuators along the linear directions of the Cartesian space. In the following, we will refer to this mechanical interface as the mobile frame. TSA modules integrating in a very compact space an high speed-low torque DC motor with incremental encoder and a force sensor are adopted in order to minimize the complexity and the cost of the device. TSA closed loop position and force control are implemented in the module embedded controller. Being the device driven by means of cables, a minimum number of $n + 1$ actuators is necessary to control motion and forces in a n -dimensional space. Therefore, being interested in controlling only linear movements, four actuators are needed. The actuators are arranged on the fixed frame, while the strings are connected between the output shafts of the TSA modules and the anchoring points on the mobile frame. To allow the motor module to be always aligned with the fixing points on the frame and

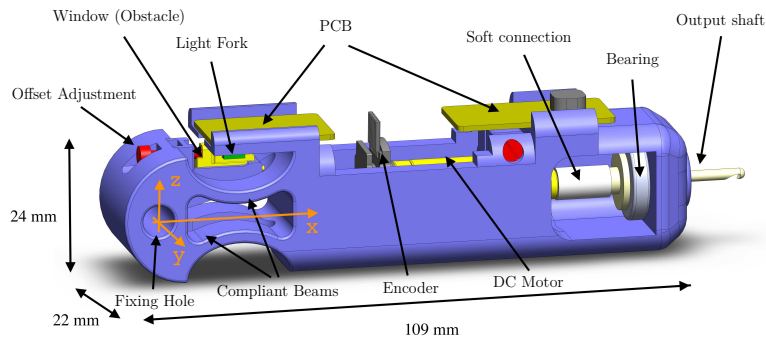


Fig. 8.4 Detail of the TSA module design.

the corresponding point on the mobile frame, an universal joint has been used to fix the TSA modules to the frame.

8.1.2 The TSA Module

The TSA module design and its integrated force sensor has been described in details in [89] and [90], and therefore here only a brief summary of its main features is reported. Figure 8.4 reports a detailed 3D view of the TSA module design. The frame structure is manufactured in ABS plastic [91] by 3D rapid prototyping. It composes a pair of axial-symmetric compliant beams that act as a linear spring, providing to the structure a certain compliance for the implementation of the force sensor. An optoelectronic device is used to detect the frame deformation and convert it back to the applied force. As can be seen in Fig. 8.4, a DC motor equipped with an incremental encoder for angular position sensing is mounted in the module, while the output shaft is supported by an axial bearing at the point of the twisted string connection to both reduce the friction and prevent the transmission force from damaging the motor. A silicon tube is used to connect the transmission shafts and the DC motor in order to solve problems regarding misalignment of the rotational axes of the motor and the module output shaft. The designed TSA module permits the transmission force to be entirely supported by the

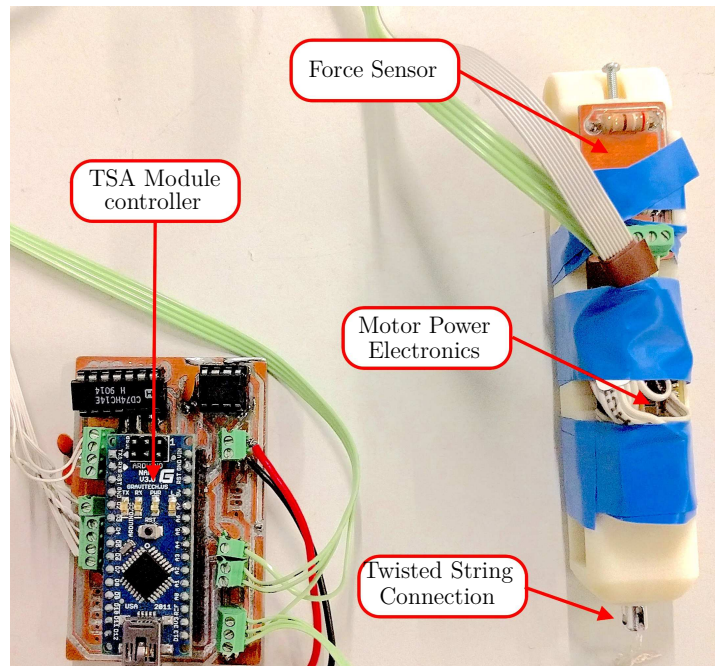


Fig. 8.5 Detailed view of the TSA module prototype and control electronics.

output shaft through the combined bearing, while the motor is only used to transmit the necessary torque for driving the twisted string actuation to the output shaft.

Figure 8.5 depicts the TSA module embedded controller based on an Arduino NANO board. The actuator electronics provide a digital interface for input and output signals required for the actuation system control, including both the motor power electronics, the conditioning system for both the force sensor and the encoder and a microcontroller board for controlling the TSA module, see Fig. 10. The communication between the TSA controller and the external system can be implemented with either UART, SPI or I2C interfaces.

8.2 Conclusions and Future Works

In this chapter, the development of a novel cable-driven haptic interface is presented, able to render a 3D linear force feedback by means of four TSA modules. To the best

of our knowledge the use of twisted string transmission in such a devices has never been investigated. One of the main benefit of rendering forces by means of string tensions is the scalability of the haptic workspace. This aspect makes cable-driven mechanisms potentially suited for overcoming the workspace limitations that characterize haptic solutions based on serial chains.

The structure of the proposed haptic interface presents a tetrahedron-like arrangement of the actuation modules, obtained by considering a spherical workspace, a minimum level of feedback that can be transmitted and the fact that at least 4 tendons are necessary to render linear forces in all the directions of the Cartesian space.

Since the device here presented is still under development, further activities are necessary in order to complete the real setup and proof the effectiveness in terms of force reflection through experimental results. Other future extensions will include the study of a complex mechanical structure, based on Gimbal-like mechanisms, able to allow the actuation forces always to be aligned with the bracelet's center point, avoiding the creation of undesired torques acting on the mobile frame.

Chapter 9

A Wearable Robotic Hand Exoskeleton

Several robotic systems conceived to be directly interfaced with the human hand have developed worldwide during the last years, mainly as haptic interfaces for teleoperated manipulation [92, 93], or for interaction with micro/nano scale phenomenon [94, 95] and medical training [96, 97]. In [98, 99] the development of an haptic interface supported by an external arm that enables the user to interact and feel the virtual object without imposing any weight and providing 3D fingertip force display is presented. In [100] the mechanism optimization for providing proper finger movement and force is performed. Battezzato presented the analysis and optimization of underactuated hand exoskeleton mechanisms in [101, 102]. In [103], a biomimetic hand device (BiomHED) in order to assist survivors in producing complex hand movements with a limited number of actuator is implemented. This system is actuated by exotendons with the capability of the regenerating the distinct joint coordination patterns of human muscle-tendon units.

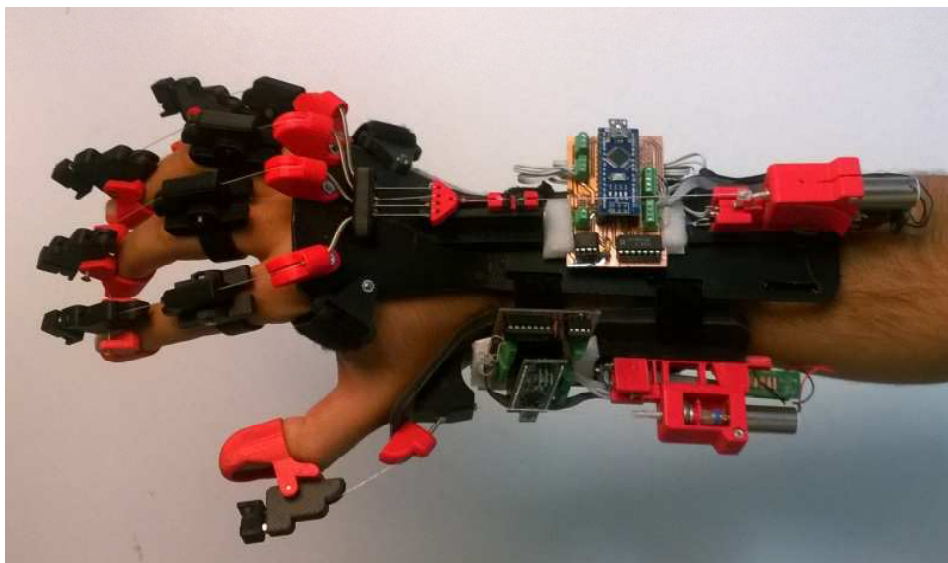


Fig. 9.1 Detailed view of the hand exoskeleton.

The main functionality of robotic hand interfaces such as hand exoskeletons is twice. On one side, haptic hand interfaces are conceived to drive teleoperated systems, both virtual and real, therefore the main purpose is to follow the user movements, minimizing or controlling the interface dynamics during free motion, and providing proper feedback to the user in case of contact with virtualized or real objects on the teleoperated system. On the other side, these interfaces can be used for rehabilitation purposes, guiding the user's finger movements through proper patterns designed to recover the hand functionalities. It is worth remarking that in case of haptic interfaces, different kind of feedback can be provided, such as force [104, 105], vibro-tactile [106–108] or pressure feedback [109, 110].

Besides the different applications, the robotic system design requirements present many common aspects, such as the adaptability to different users, the mobility of the device that should not infer the user's movements and the capability of controlling the feedback provided to the user.

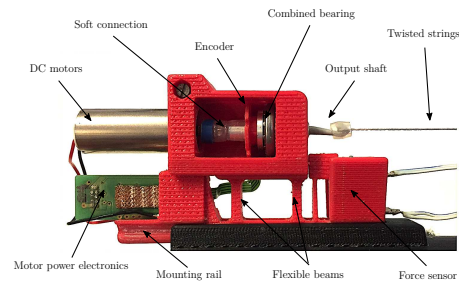


Fig. 9.2 Detail of the actuation module.

In this chapter, the development of an hand exoskeleton driven by means of a couple of Twisted String Actuators (TSAs) [9] is reported. This device is conceived to be used as an haptic interface to drive a teleoperated robotic manipulator equipped with a 3-dof gripper, providing to the user a proper force feedback during grasping activities. Surface Electromyography (sEMG) signals also can be used to detect the shape of the user hand to perform robotic gripper preshape before grasp execution. Moreover, the design of the exoskeleton is oriented to the maximum simplicity, therefore the device is implemented as a wearable system without any external bulky mechanism to guide the finger movements and support the actuation used to provide the force feedback, but relying on the skeleton structure of the hand itself as supporting mechanism for the cable-based actuation system.

This chapter is organized as follow. In Sec. 9.1 the overall device is described, focusing on the design, the actuation system and the controller. In the final Sec. 10 the outcomes of the works are summarized and comments on future work are given.

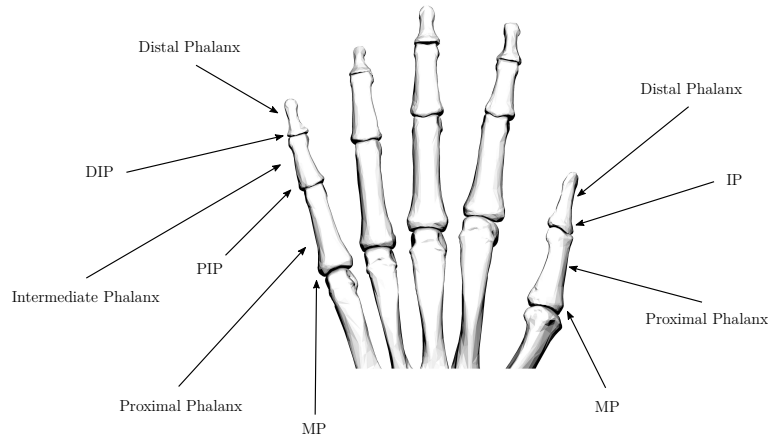


Fig. 9.3 Detailed view of the fingers structure.

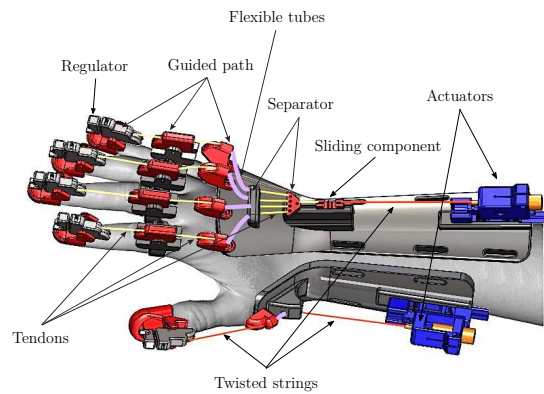
9.1 System Description

9.1.1 Fingers Structure

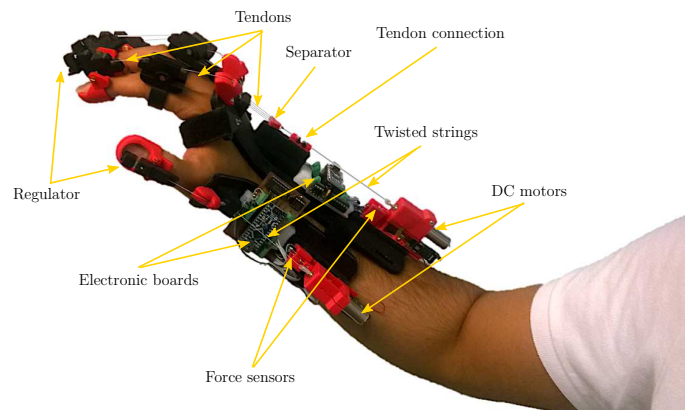
The hand is comprised of five digits and they are called thumb, index, middle, ring and little finger. The four fingers from index to little finger have three phalanges: distal, intermediate and proximal phalanges and have three joints: Distal Interphalangeal (DIP), Proximal Interphalangeal (PIP) and Metacarpophalangeal (MP) joints while The thumb comprised of two phalanges; distal and proximal phalanges and two joints: Interphalangeal (IP) and Metacarpophalangeal (MP) joints (see Fig. 9.3).

9.1.2 Design of the Hand Exoskeleton

Fig. 9.4 demonstrates a simple, light and fully adjustable hand exoskeleton that are easy to attach and fit to the human fingers. All part of the system are made of ABS plastic



(a) Schematic view of the hand exoskeleton

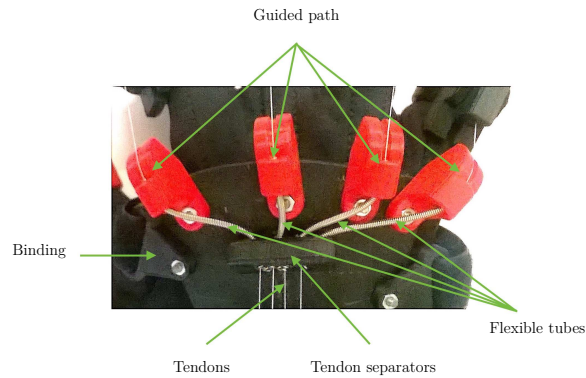


(b) Hand exoskeleton

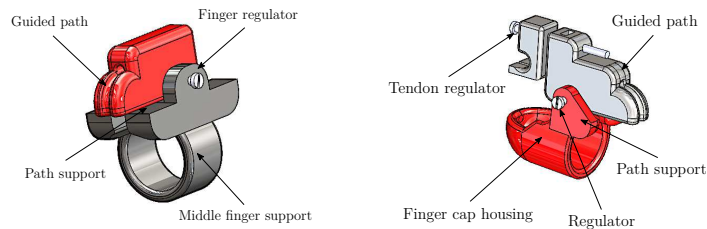
Fig. 9.4 Detail view of the hand exoskeleton.

by 3D rapid prototyping. The hand exoskeleton composed by two parts to actuate the four fingers and thumb separately and are attached to the human wrist. Two actuation modules (See Chapter. 4, Sec. 4.4) with integrated force sensor are also attached to the bases by a mounting rail, see Fig. 9.2.

The four fingers actuation mechanism are connected to the actuation module by means of tendons that are guided through the path and linear guides to prevent the twisting of the tendon itself and with a separator to guide the tendons trough each finger with a flexible tube. As can be seen in Fig. 9.4, the four finger mechanisms consist of three



(a) Base tendon guided path.



(b) Middle finger support. (c) Finger cap structure.

Fig. 9.5 Detailed view of the finger supports.

supporting structures; a guided tendon path that are mounted on the exoskeleton base (Fig. 9.5a), a ring that hosts the curved guided path for the tendons which are mounted on the proximal phalanges and are adjustable by means of screw (Fig. 9.5b). Also an adjustable finger cap placed on distal phalanges and hosts the tendon length regulator, Fig. 9.5c. The path is designed with a curved shape in order to tendons follow the finger movement with the same shape.

The thumb actuation mechanism is a bit different than the other fingers. It consists of two supporting structure that are placed on the base structure and distal phalanx. The thumb is connected to the actuation module directly by twisted string which are guided on a curved path and through a flexible tube to reduce the friction caused by twisting

the strings. More detail about modeling of the twisted string through the curved path is described in Chapter. 3.

9.1.3 Control of the System

Fig. 9.4b shows the TSA module embedded controller based on an Arduino NANO board. In the TSA module, an optoelectronic device is then used to detect the frame deformation and convert it back to the applied force causing the deformation.

A digital interface to input and output signals required for the actuation system control is provided by the actuator electronics, including both the motor power electronics, the conditioning system for both the optical encoder and the force sensor and a microcontroller board for controlling the TSA module (see Fig. 9.4b). The communication of the TSA controller with external systems can be implemented both with UART, SPI or I2C interfaces.

9.2 Conclusions

Moreover, the design of the exoskeleton is oriented to the maximum simplicity, therefore the device is implemented as a wearable system without any external bulky mechanism to guide the finger movements and support the actuation used to provide the force feedback, but relying on the skeleton structure of the hand itself as supporting mechanism for the cable-based actuation system.

In this chapter, a hand haptic interface driven by a couple of twisted string actuators is presented. This device is able to provide independent force feedback to the thumb on one side, and to the the index to little fingers grouped together on the other side. This configuration has been selected to provide the user with force feedback during the

execution of grasping tasks by means of a teleoperated robotic manipulator. This chapter reports the design of the hand exoskeleton, the description of the actuation system and of the embedded controller.

Future work will be devoted to the experimental evaluation of this device. The system will be evaluated both by means of a simple virtual environment that emulates 1-dof grasping activities of rigid and compliant objects and by predefined trajectories to show the applicability of the system for rehabilitation purposes. This device can be used as an haptic interface to drive a teleoperated robotic manipulator equipped with a 3-dof gripper, providing to the user a proper force feedback during grasping activities. Surface Electromyography (sEMG) signals also can be used to detect the shape of the user hand to perform robotic gripper preshape before grasp execution.

Chapter 10

CONCLUSIONS

The twisted string actuation system is particularly suitable for very compact and light-weight robotic devices, like artificial limbs and exoskeletons, since it renders a very low apparent inertia at the load side, allowing the implementation of powerful tendon-based driving systems, using small-size DC motors characterized by high speed, low torque and very limited inertia. Its basic properties has been reported.

One of the major limitations of the TSA system is by now related to the fact that the string should not be in contact with any obstacle, because this contact will stop the string twisting. To understand this effect, an experimental setup has been developed to study the behavior of the TSA in the case the string is in contact with obstacles or constraints guiding the string itself.

The TSA principle is used for the implementation of a variable stiffness Joint by using two actuators in antagonistic configuration by deriving the dynamic model of the system. To evaluate the variable stiffness joint characteristics, an experimental setup has been developed and the identification of the main system parameters is carried out. A simple controller based on the inversion of the device static model is introduced

and experimentally evaluated. Future activities will be devoted to the experimental evaluation of different control strategies on this experimental setup.

A low-cost and easy-to-build optoelectronic force sensor has been implemented and it uses a commercial and very compact optoelectronic component, called light fork, as sensing element. The particular structure of the proposed sensor and the characteristics of the sensing element other than allowing a compact device implementation, allow the easy implementation of the force sensor without requiring particular care or experience in the component assembly. This allowed us to perform a quite fast evaluation of different design implementations. The mathematical model of the sensor compliant frame has been presented and validated by means of both FEA and experimental evaluation of four different sensor specimens. A static calibration and dynamic load experiments has been carried out showing the good linearity and sensitivity of the implemented devices, which are also characterized by very limited hysteresis. In the future work, this sensor can be used in various robotic applications and also for the implementation of multi-axis force/torque.

An innovative twisted string actuation module system with an integrated force sensor which can be used for diverse robotic applications has been presented. To validate the TSA module compliant frame, the FEA has been compared with experimental measures and different experiments have been carried out to verify the properties of the proposed TSA module. The experimental results prove that the proposed actuation system is sufficient to be used for different robotic applications. Then a wearable TSA module system with integrated force sensor which can be used for rehabilitation and assistive robotic applications has been implemented. Furthermore, to show the capabilities of the proposed TSA module in a real assistive applications, an experiment involving four male healthy subjects has been carried out, where the TSA module has been used to provide load compensation to the user's elbow joint during lifting tasks of a 2 Kg load. The

experimental results show that the device, together with a suitable control scheme, can be successfully used to help and limit the user's biceps muscle activity during dynamic motions when a load is applied in proximity of the wrist. Future work will be devoted to the installation of the module on the back of the user, in order to obtain a wearable elbow assistive device and to the implementation of a sEMG-driven control scheme that makes use of both biceps and triceps, exploiting antagonistic muscle activation concepts.

A novel cable-driven haptic interface, able to render a 3D linear force feedback by means of four TSA modules has been presented. The structure of the proposed haptic interface presents a tetrahedron-like arrangement of the actuation modules, obtained by considering a spherical workspace, a minimum level of feedback that can be transmitted and the fact that at least 4 tendons are necessary to render linear forces in all the directions of the Cartesian space. Since the device here presented is still under development, further activities are necessary in order to complete the real setup and proof the effectiveness in terms of force reflection through experimental results. Other future extensions will include the study of a complex mechanical structure, based on Gimbal-like mechanisms, able to allow the actuation forces always to be aligned with the bracelet's center point, avoiding the creation of undesired torques acting on the mobile frame.

A hand haptic interface driven by a couple of twisted string actuators is implemented. This device is able to provide independent force feedback to the thumb on one side, and to the the index to little fingers grouped together on the other side. This configuration has been selected to provide the user with force feedback during the execution of grasping tasks by means of a teleoperated robotic manipulator. The design of the hand exoskeleton and the description of the actuation system and of the embedded controller has been reported. Future work will be focused on the experimental evaluation of this device. The system will be evaluated both by means of a simple virtual environment that emulates 1-dof grasping activities of rigid and compliant objects and by predefined

trajectories to show the applicability of the system for rehabilitation purposes. This device also can be used as an haptic interface to drive a teleoperated robotic manipulator equipped with a 3-dof gripper, providing to the user a proper force feedback during grasping activities. Surface Electromyography (sEMG) signals also can be used to detect the shape of the user hand to perform robotic gripper preshape before grasp execution.

Appendix A

Feedback Linearization of VSA Based on TSA

In this chapter, an ongoing work for the implementation of a variable stiffness joint actuated by a couple of twisted string actuators in antagonistic configuration is reported, see Fig. [A.1](#). A simple control algorithm for controlling the joint stiffness and position simultaneously is discussed, and a the feedback linearization of the device is taken into account and validated in simulation.

A.1 Control Algorithms

In the following, two different controllers for the proposed variable stiffness joint are described. The first control algorithm is simply based on the inversion of the static equations describing the system behavior and on standard PID motor position controllers. The second algorithm takes into account full feedback linearization of the system dynamics to achieve fully decoupled and simultaneous joint position and stiffness control. In

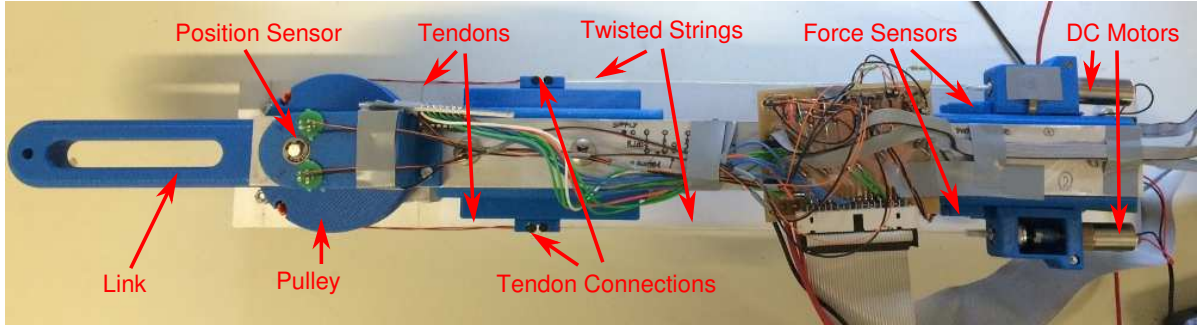


Fig. A.1 Top view of the experimental setup.

both these cases, the joint stiffness is estimated from the joint position and the motors positions according to (Sec. 4, eq. (4.8)).

A.1.1 Static Model Inversion

In this case, the problem to be solved is to find the desired motor positions $\theta_{\{A,B\}d}$ given the desired joint position θ_{jd} and stiffness S_{jd} according to (Sec. 2, eq. (2.10)) and (Sec. 4, eq. (4.8)). To this end, given the desired joint position θ_{jd} , the resulting transmission lengths $p_{A,B}$ are computed from (Sec. 2, eq. (4.1)) and (Sec. 4, eq. (4.2)). Then, substituting these information into (Sec. 2, eq. (2.10)) and (Sec. 4, eq. (4.8)) and inverting them, a couple of equation providing the desired motor positions is obtained.

At this point, standard PID controllers can be used to control the motor position to the desired value. This control approach has the great advantage of not requiring sensor feedback from the joint, fact that may introduce stability issues due to the limited joint stiffness. On the other hand, this control approach is based on the perfect knowledge of the system model and parameters, fact that may introduce significant errors when applied to the real system. To reduce these side effects, an accurate identification of the system parameters and the verification of the models need to be performed.

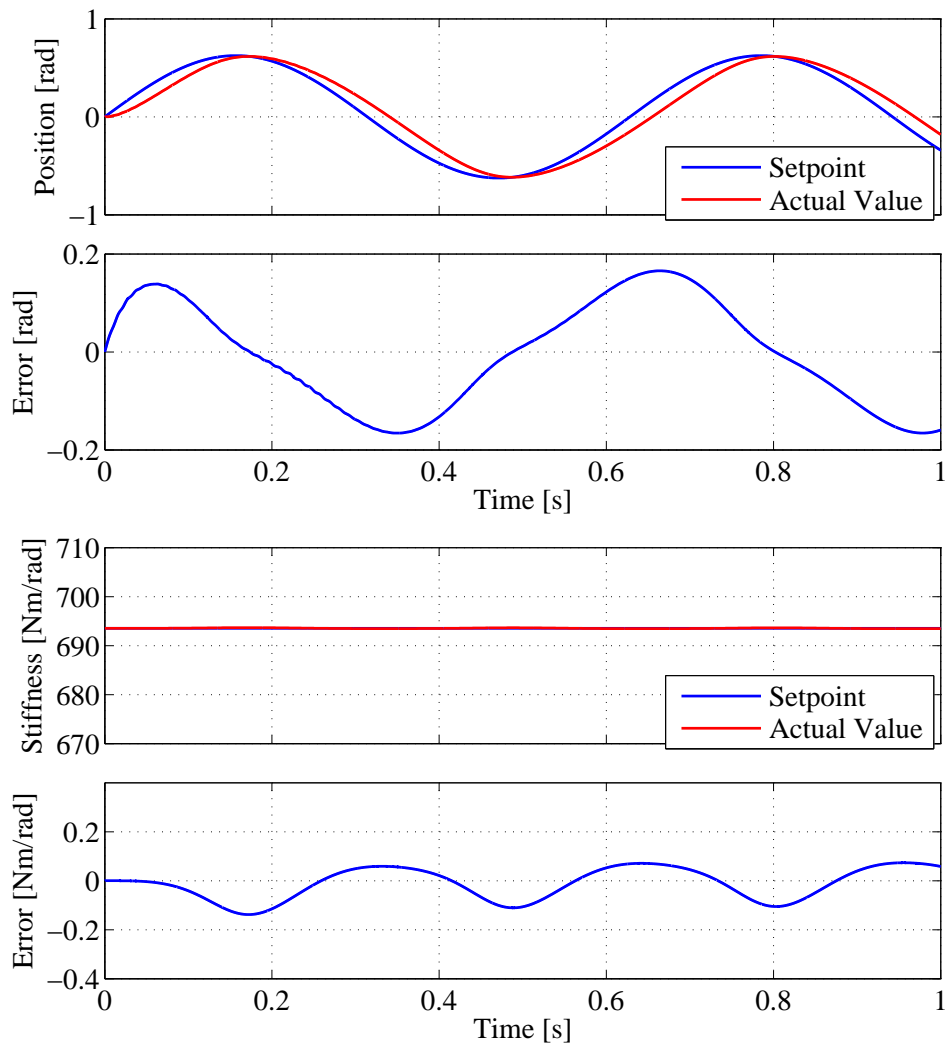


Fig. A.2 Position and stiffness response with constant stiffness setpoint.

In Fig. A.2 the simulation results with constant stiffness and a sinusoidal position reference characterized by a frequency of 10 rad/s and an amplitude of 0.7 rad is reported. While the stiffness error is quite limited, the position error is quite evident: this effect could be ascribed to the link inertia that is neglected by this type of controller. For the sake of completeness, the response of the system to the same position reference but in case of a sinusoidal stiffness setpoint with a frequency of 20 rad/s and an amplitude of 15 Nm/rad is reported in Fig. A.3. Also in this case the tracking of the stiffness reference is quite accurate while a position error of the same order of magnitude of the previous simulation is still present.

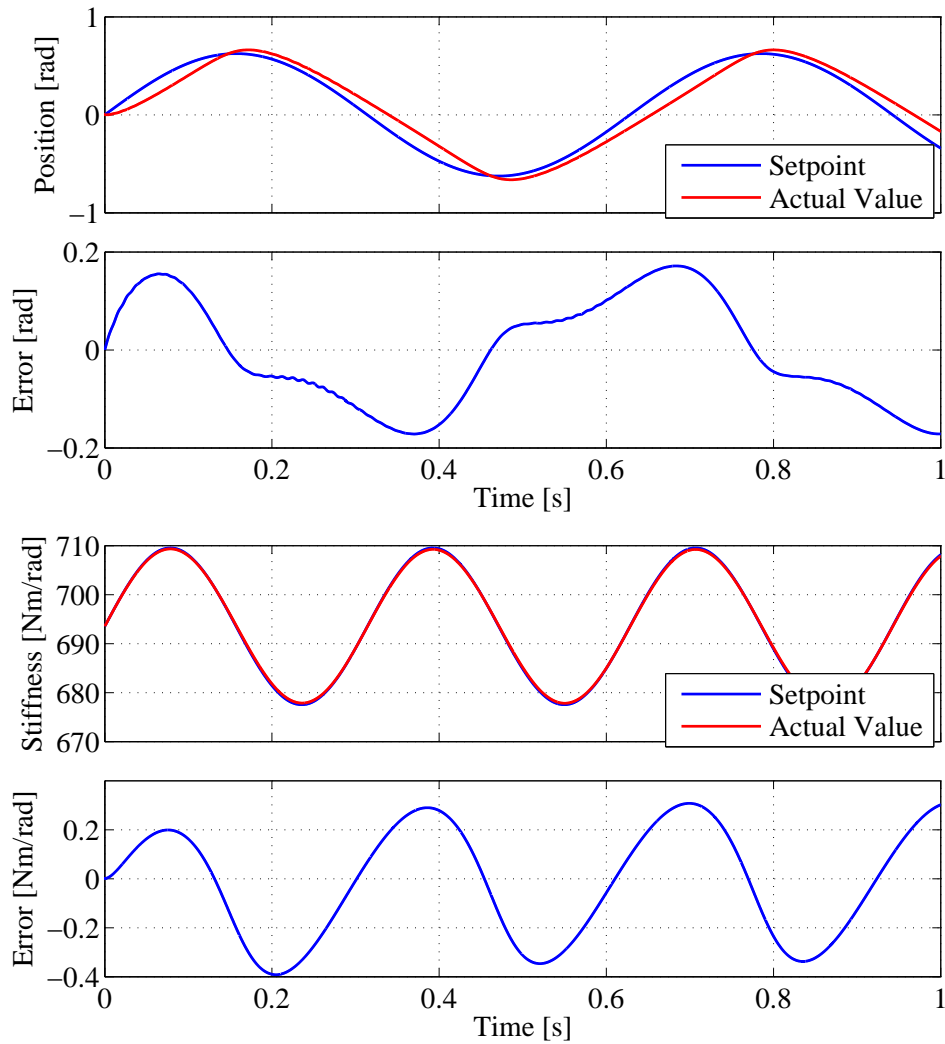


Fig. A.3 Position and stiffness response with variable stiffness setpoint.

A.1.2 Feedback Linearization

The control problem is now formulated as the tracking of a desired position reference θ_{jd} and stiffness reference S_{jd} , which is assumed sufficiently smooth so that the time derivative of the position reference are definite and bounded up to the 4-th order and the time derivative of the stiffness reference are definite and bounded up to the 2-nd order.

The basic idea behind the feedback linearization approach of the considered system is to find a control vector $u = [\tau_A \quad \tau_B]^T$ capable of realizing a linear relationship between

the input reference signals and the system outputs by means of a static state feedback. This control strategy implicitly requires the availability of the whole system state, i.e. both motors and joint positions and velocities, fact that needs to be carefully taken into account during the controller implementation into the real system.

In order to establish the relationship between the control input $u = [\tau_A \quad \tau_B]^T$ and the output $y = [\theta_j \quad S_j]^T$, the second-order derivative of the joint dynamic equation (4.5) and the stiffness equation (4.8) is computed neglecting the effect of the external disturbance torque

$$\theta_j^{[4]} = J_j^{-1} r_J \left(\frac{\partial^2 F_{LA}}{\partial t^2} - \frac{\partial^2 F_{LB}}{\partial t^2} \right) \quad (\text{A.1})$$

$$\ddot{S}_j = r_J^2 \left[\frac{\partial^2 S_A}{\partial t^2} + \frac{\partial^2 S_B}{\partial t^2} \right] \quad (\text{A.2})$$

It can be easily verified that the previous equations can be rewritten in the form

$$\begin{bmatrix} \theta_j^{[4]} \\ \ddot{S}_j \end{bmatrix} = F(q) + G(q) u \quad (\text{A.3})$$

where $q = [\theta_{mA} \quad \dot{\theta}_{mA} \quad \theta_{mB} \quad \dot{\theta}_{mB} \quad \theta_j \quad \dot{\theta}_j]^T$ is the system state vector. It is worth noticing that, even if the computation of the second time derivative of both the joint acceleration and stiffness is required in eq. (A.3), it can be proven that the terms appearing in (A.3) can be expressed as a function of the system state q only. The details of this computation are not here reported for brevity. Another important point to note is that the motor input u explicitly appears into the equations. This allows to state that the relative degree of the

joint position is 4 (i.e. the order of the position derivative) and the one of the stiffness is 2 (i.e. the order of the stiffness derivative).

While the vector $F(q)$ collects all the terms of eqs. (A.1) and (A.2) that are not multiplied by the motor input torque vector u (the expression of this vector is not here reported for brevity), the matrix $G(q)$ (also called decoupling matrix) collecting all the input dependent terms can be written in the form

$$G(q) = r_j J_m^{-1} \begin{bmatrix} J_j^{-1} \frac{\partial F_{LA}}{\partial \theta_{mA}} & -J_j^{-1} \frac{\partial F_{LB}}{\partial \theta_{mB}} \\ r_j \frac{\partial S_A}{\partial \theta_{mA}} & r_j \frac{\partial S_B}{\partial \theta_{mB}} \end{bmatrix} \quad (\text{A.4})$$

Under the assumption of non-singularity of the matrix $G(q)$ (this can be ensured by a proper selection of the system operation range, and in particular by ensuring that $\theta_{m\{A,B\}} > 0$, the proof is not here reported for brevity), the control vector u that allows achieving the static feedback linearization of the system is defined as

$$u = G(q)^{-1}(-F(q) + v) \quad (\text{A.5})$$

where $v = [v_1 \ v_2]^T$ is an auxiliary control input used to stabilize the system and achieve the setpoint tracking. This control vector leads to the linear system

$$\begin{bmatrix} \theta_j^{[4]} \\ \ddot{S}_j \end{bmatrix} = \begin{bmatrix} v_1 \\ v_2 \end{bmatrix} \quad (\text{A.6})$$

This linear system can be seen as the union of two independent (decoupled) systems,

one with output $\theta_j^{[4]}$ and input v_1 and the second with output \ddot{S}_j and input v_2 . It can be also easily seen that this two linear systems are composed by chain of integrators, 4 integrators for the first system and 2 for the second, then this two systems are unstable since the first system presents 4 poles in the origin whereas the second has 2 poles in the origin. The this approach turns the control problem of a nonlinear system into the stabilization of a linear system, that can be easily obtained by a proper design of a state feedback matrix as reported in the next section.

Note that the implementation of the state feedback control (A.5) requires the measurement of the whole system states. It is then assumed that the angular position of the motors $\theta_{m\{A,B\}}$, their angular velocity $\dot{\theta}_{m\{A,B\}}$, the position of link θ_j and its velocity $\dot{\theta}_j$ can be measured.

A.1.3 Control of the Feedback-Linearized System

The feedback linearization controller (A.5) turns the non-linear model of the variable stiffness joint actuated by antagonistic twisted string actuators into a set of two decoupled linear systems (A.6). Therefore, the control problem is moved to the design of two stabilizing controllers for tracking the desired position and stiffness profiles. To this purpose, an optimal control approach for the design of the state feedback matrix has been selected. Considering the position and stiffness reference signals θ_{jd} and S_{jd} and defining the position and stiffness tracking error as

$$\tilde{\theta}_j = \theta_{jd} - \theta, \quad \tilde{S}_j = S_{jd} - S_j \quad (\text{A.7})$$

the system (A.6) can be written as

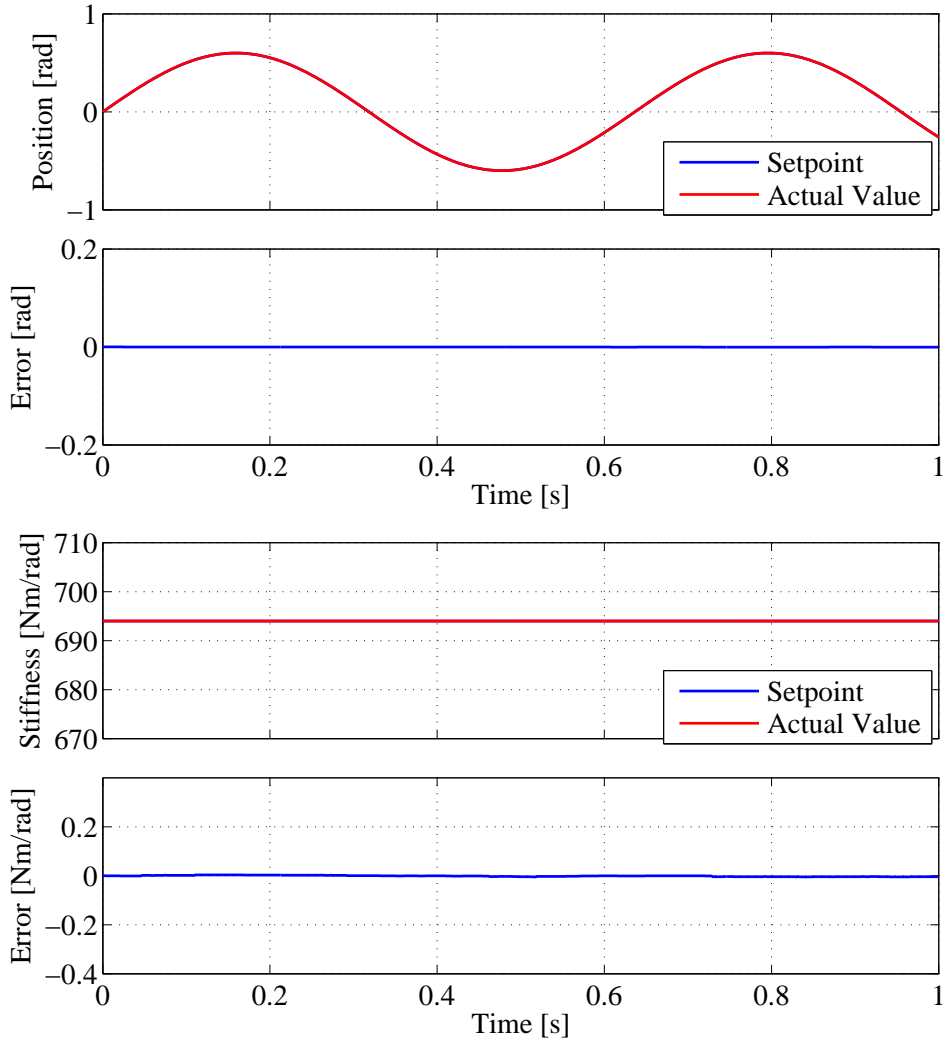


Fig. A.4 Simulation of the joint system with feedback linearization control: sinusoidal position setpoint and constant stiffness.

$$\begin{bmatrix} \theta_j^{[4]} \\ \ddot{S}_j \end{bmatrix} = \begin{bmatrix} v_1 + \theta_{jd}^{[4]} \\ v_2 + \ddot{S}_{jd} \end{bmatrix} \Rightarrow \begin{bmatrix} \tilde{\theta}_{jd}^{[4]} \\ \ddot{\tilde{S}}_j \end{bmatrix} = \begin{bmatrix} v_1 \\ v_2 \end{bmatrix} \quad (\text{A.8})$$

It is important to point out that the definition of the controller (A.8) implies that the the position trajectory is continuous and derivable up to the 4-th order and the stiffness trajectory is continuous and derivable up to the 2-nd order.

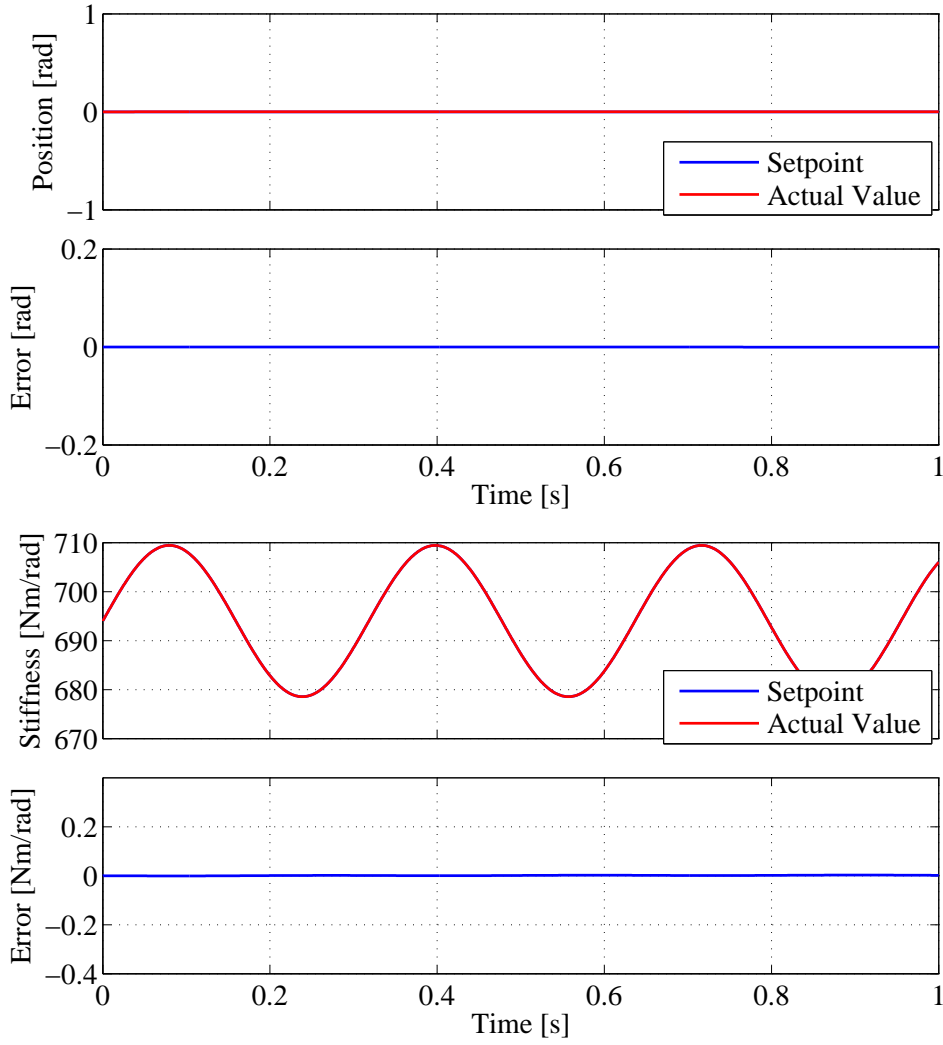


Fig. A.5 Simulation of the joint system with feedback linearization control: constant position setpoint and sinusoidal stiffness setpoint.

Considering the system (A.6) and selecting $\tilde{\boldsymbol{\theta}} = [\ddot{\theta}_j \quad \dot{\theta}_j \quad \theta_j]^T$ and $\tilde{\boldsymbol{S}} = [\dot{S}_j \quad S_j]^T$ as the states of the two position and stiffness linear subsystems, these systems can be written in the state-space form as

$$\dot{\tilde{\boldsymbol{\theta}}} = \mathbf{A}_\theta \tilde{\boldsymbol{\theta}} + \mathbf{B}_\theta v_1 \quad (\text{A.9})$$

$$\dot{\tilde{\boldsymbol{S}}} = \mathbf{A}_s \tilde{\boldsymbol{S}} + \mathbf{B}_s v_2 \quad (\text{A.10})$$

where

$$\mathbf{A}_\theta = \begin{bmatrix} 0 & 1 & 0 & 0 \\ 0 & 0 & 1 & 0 \\ 0 & 0 & 0 & 1 \\ 0 & 0 & 0 & 0 \end{bmatrix}, \quad \mathbf{B}_\theta = \begin{bmatrix} 0 \\ 0 \\ 0 \\ 1 \end{bmatrix} \quad (\text{A.11})$$

$$\mathbf{A}_S = \begin{bmatrix} 0 & 1 \\ 0 & 0 \end{bmatrix}, \quad \mathbf{B}_S = \begin{bmatrix} 0 \\ 1 \end{bmatrix} \quad (\text{A.12})$$

The, the control vector $v = [v_1 \ v_2]^T$ can be selected as

$$v_1 = - \begin{bmatrix} k_{\theta 0} & k_{\theta 1} & k_{\theta 2} & k_{\theta 3} \end{bmatrix} \tilde{\boldsymbol{\theta}}_j = -\mathbf{K}_\theta \tilde{\boldsymbol{\theta}} \quad (\text{A.13})$$

$$v_2 = - \begin{bmatrix} k_{S0} & k_{S1} \end{bmatrix} \tilde{\mathbf{S}} = -\mathbf{K}_S \tilde{\mathbf{S}} \quad (\text{A.14})$$

leading to the following decoupled linear systems with states feedback

$$\dot{\tilde{\boldsymbol{\theta}}} = (\mathbf{A}_\theta - \mathbf{B}_\theta \mathbf{K}_\theta) \tilde{\boldsymbol{\theta}} \quad (\text{A.15})$$

$$\dot{\tilde{\mathbf{S}}} = (\mathbf{A}_s - \mathbf{B}_s \mathbf{K}_s) \tilde{\mathbf{S}} \quad (\text{A.16})$$

where \mathbf{K}_θ and \mathbf{K}_s are the state feedback gain matrices. Due to the similarity of two subsystems and for the sake of brevity, the design of feedback gain \mathbf{K}_θ will be reported only, the design of \mathbf{K}_s follows the same design procedure. Adopting an optimal design approach, the matrix \mathbf{K}_θ can be computed as

$$\mathbf{K}_\theta = R^{-1} \mathbf{B}^T \mathbf{P} \quad (\text{A.17})$$

where R is a scalar positive input weighting factor and $n \times n$ matrix \mathbf{P} is determined from the solution of the CARE equation

$$\mathbf{A}^T \mathbf{P} + \mathbf{P} \mathbf{A} - \mathbf{P} \mathbf{B} R^{-1} \mathbf{B}^T \mathbf{P} + \mathbf{Q} = \mathbf{0} \quad (\text{A.18})$$

where \mathbf{Q} is a semi-positive definite matrix that weights the state components.

To verify whether the states feedback linearization allows achieving the desired set-point tracking and decoupling of the position and stiffness profiles and whether the optimal states feedback control is able to ensure the stability of the linearized system and good dynamic performance, the simulation of the variable stiffness joint model with feedback linearization and linear control of the linearized system has been carried out. With the aim of verifying both the performance and the system stability, the two subsystems are firstly evaluated independently under a sinusoidal position reference signals with a frequency of 10 rad/s and an amplitude of 0.7 rad and constant stiffness setpoint, and the simulation results are reported in Fig. A.4. From these plots it is possible to see that, as expected, both the position and stiffness regulation show a stable behavior

and the tracking error is almost zero. This latter fact is achieved thanks to the nature of the feedback linearization and the optimal control of the linearized system.

Fig. A.5 reports the simulation results with a sinusoidal stiffness reference of 15 Nm/rad amplitude, 20 rad/s frequency and constant position reference. Also in this case, the plots show that both the position and stiffness regulation exhibit a stable behavior and the tracking error is almost zero as expected.

Finally, The dynamics performance with both of sinusoidal reference signals on position and stiffness is illustrated in Fig. A.6. These plots allow to verify that the two systems are decoupled, indeed the same performance obtained in the previous two cases are obtained even during the simultaneous tracking of both position and stiffness profiles.

A.2 Conclusions

The twisted string actuation system is a very simple, cheap, small and lightweight actuation system, suitable for highly integrated robotic devices like artificial limbs, exoskeletons and robotic hands. In this chapter, a theoretical investigation about the use of this actuation principle for the implementation of a variable stiffness mechanism using two actuators in antagonistic configuration is reported. In this analysis, the intrinsic stiffness variability of the twisted string actuation is exploited. Firstly, a simple controller based on the inversion of the static model of the device has been studied to verify the behavior of the system under the effect of a simple controller. Then aiming at improving the control system performance, a feedback linearization approach and a linear optimal control strategy are adopted to achieve fully decoupled control of the position and the stiffness profiles. Future activities will be devoted to the implementation of an experimental setup for the evaluation of the properties of the proposed mechanism and the validation of the proposed controllers.

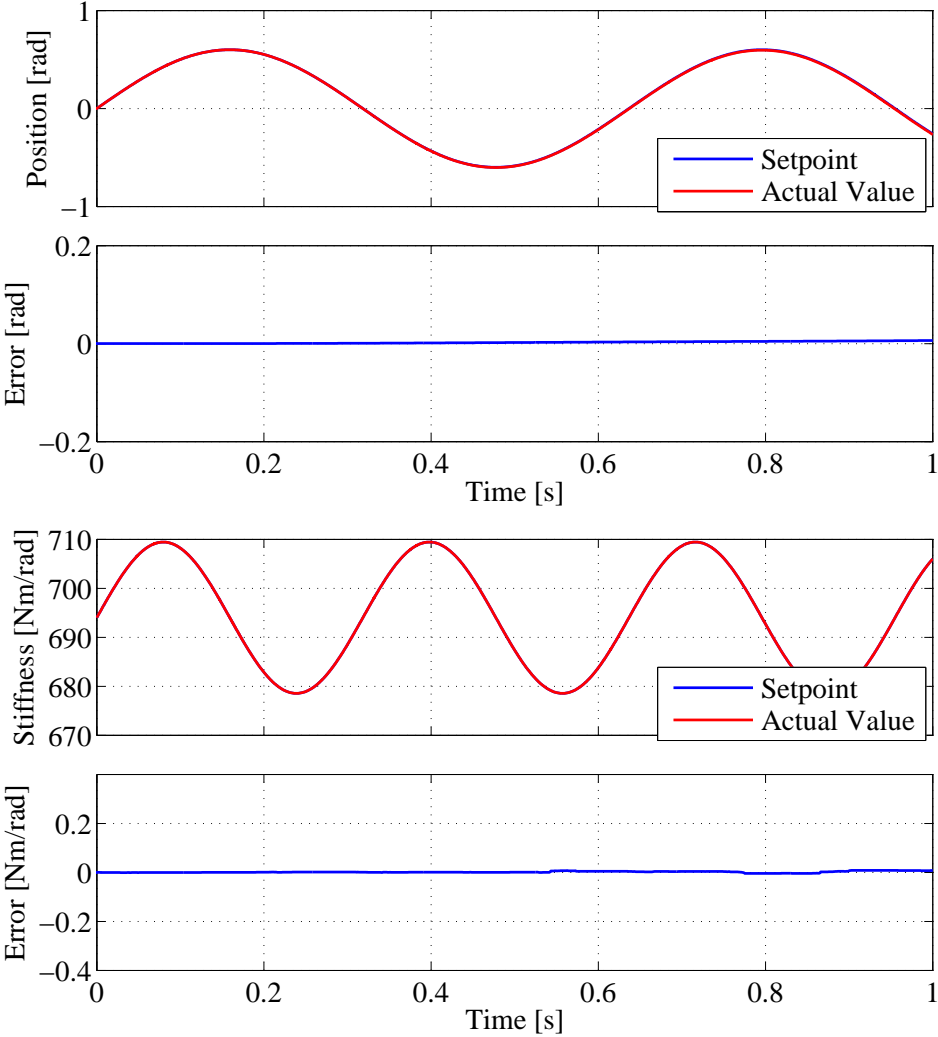


Fig. A.6 Simulation of the joint system with feedback linearization control: sinusoidal position setpoint and sinusoidal stiffness setpoint.

Appendix B

PUBLICATIONS

Publications in Journals

1. **M. Hosseini**, R. Meattini, G. Palli, C. Melchiorri, "A Wearable Robotic Device Based on Twisted String Actuation for Rehabilitation and Assistive Applications." *Journal of Robotics* 2017 (2017).
2. G. Palli, **M. Hosseini**, C. Melchiorri, "A Simple and Easy-to-Build Optoelectronics Force Sensor Based on Light Fork: Design Comparison and Experimental Evaluation", *Sensors & Actuators A: Physical*, in press, 2017.
3. G. Palli, **M. Hosseini**, and C. Melchiorri. "Experimental Evaluation of Guided Twisted Actuation." *IFAC-PapersOnLine* 49.21 (2016): 380-385.

Publications in Conferences

1. **M. Hosseini**, R. Meattini, G.Palli, C.Melchiorri, "Development of sEMG-Driven Assistive Devices Based on Twisted String Actuation ",3rd International Conference on Control, Automation and Robotics (ICCAR 2017).
2. **M. Hosseini**, G. Palli C. Melchiorri," Design and Implementation of a Simple and Low-Cost Optoelectronic Force Sensor for Robotic Applications", 2016 IEEE International Conference on Advanced Intelligent Mechatronics, July 12-15, 2016, Banff, Alberta, Canada (AIM 2016).
3. R.Meattini, **M. Hosseini**, G.Palli, C.Melchiorri, "Early Evaluation of sEMG-Driven Muscle Modelling for Exoskeleton-based Rehabilitation and Assistive Applications",2016 IEEE Conference on Robotics and Biomimetics (ROBIO 2016), December 3-7, 2016, Qingdao, China.
4. G. Palli, **M. Hosseini**, C. Melchiorri," Twisted String Actuation with Sliding Surfaces", 2016 IEEE/RSJ International Conference on Intelligent Robots and Systems, October 9-14, Daejeon, Korea (IROS 2016)
5. G. Palli, **M. Hosseini**, L. Moriello, C. Melchiorri," Modeling and Identification of a Variable Stiffness Joint Based on Twisted String Actuators", IEEE/RSJ International Conference on Intelligent Robots and Systems, September 28- October 3, Hamburg, Germany (IROS 2015)
6. G. Palli, L. Pan, **M. Hosseini**, L. Moriello, C. Melchiorri," Feedback Linearization of Variable Stiffness Joints Based on Twisted String Actuators", 2015 IEEE International Conference on Robotics and Automation, May 26-30, 2015, Washington, USA (ICRA 2015)

7. A. Pepe, **M. Hosseini**, U. Scarcia, G. Palli C. Melchiorri,” Development of An Haptic Interface Based on Twisted String Actuators”, 2017 IEEE International Conference on Advanced Intelligent Mechatronics, (AIM 2017) in press. 2017

References

- [1] I. Gaponov, D. Popov, and Jee-Hwan Ryu. Twisted string actuation systems: A study of the mathematical model and a comparison of twisted strings. *IEEE/ASME Trans. on Mechatronics*, 19(4):1331–1342, 2014.
- [2] C May, B Holz, T Wurtz, C Natale, G Palli, and C Melchiorri. Twisted string actuation-history principle and performance. In *Workshop on Actuation & Sensing in Robotics*, 2010.
- [3] SC Jacobsen, RB Jerrard, D Knutti, and J Carruth. The ladd actuator as a prosthetic muscle. In *The Fifth International Symposium on External Control of Human Extremities, Dubrovnik, Yugoslavia*, 1975.
- [4] JJ Beaman. A dynamic model of a concentric ladd actuator. *Journal of dynamic systems, measurement, and control*, 105:157, 1983.
- [5] M Buehler. Ladd transmissions: Design, manufacture, and new compliance models. *Journal of Mechanical Design*, 119:197, 1997.
- [6] Takashi Sonoda and Ivan Godler. Multi-fingered robotic hand employing strings transmission named “twist drive”. In *Intelligent Robots and Systems (IROS), 2010 IEEE/RSJ International Conference on*, pages 2733–2738. IEEE, 2010.
- [7] Ivan Godler and Takashi Sonoda. A five fingered robotic hand prototype by using twist drive. In *Robotics (ISR), 2010 41st International Symposium on and 2010 6th German Conference on Robotics (ROBOTIK)*, pages 1–6. VDE, 2010.
- [8] Shoham Moshe. Twisting wire actuator. *Journal of Mechanical Design*, 127(3): 441–445, jul 2004.

-
- [9] G. Palli, C. Natale, C. May, C. Melchiorri, and T. Würtz. Modeling and control of the twisted string actuation system. *IEEE/ASME Trans. on Mechatronics*, 18(2):664–673, 2013.
- [10] T. Sonoda and I. Godler. Multi-fingered robotic hand employing strings transmission named “Twist Drive”. In *Proc. IEEE/RSJ Int. Conf. on Intelligent Robots and Systems*, pages 2733–2738, Taipei, Taiwan, 2010.
- [11] G. Palli, C. Melchiorri, G. Vassura, U. Scarcia, L. Moriello, G. Berselli, A. Cavallo, G. De Maria, C. Natale, S. Pirozzi, C. May, F. Ficuciello, and B. Siciliano. The DEXMART Hand: Mechatronic design and experimental evaluation of synergy-based control for human-like grasping. *The Int. Journal of Robotics Research*, 33(5):799–824, 2014.
- [12] D. Popov, I. Gaponov, and Jee-Hwan Ryu. Bidirectional elbow exoskeleton based on twisted-string actuators. In *Proc. IEEE/RSJ Int. Conf. on Intelligent Robots and Systems*, pages 5853–5858, 2013.
- [13] In-Won Park and Vytas SunSpiral. Impedance controlled twisted string actuators for tensegrity robots. In *Proc. Int. Conf. on Control, Automation and Systems*, Kintex, Korea, 2014.
- [14] D. Popov, I. Gaponov, and Jee-Hwan Ryu. Towards variable stiffness control of antagonistic twisted string actuators. In *Proc. IEEE/RSJ Int. Conf. on Intelligent Robots and Systems*, pages 2789–2794, 2014.
- [15] Dmitry Popov, Kwang-Hyun Lee, Igor Gaponov, and Jee-Hwan Ryu. Twisted strings-based elbow exoskeleton. *The Journal of Korea Robotics Society*, 8(3):164–172, 2013.
- [16] G. Palli and C. Melchiorri. Velocity and disturbance observer for non-model based load and friction compensation. In *Proc. Int. Workshop on Advanced Motion Control*, pages 194–199, Trento, Italy, 2008.
- [17] G. Palli and S. Pirozzi. Optical force sensor for the DEXMART Hand twisted string actuation system. *Sensors & Transducers*, 148(1):28–32, 2013.

-
- [18] G. Palli and S. Pirozzi. Integration of an optical force sensor into the actuation module of the DEXMART Hand. *International Journal of Robotics and Automation*, 29(2):193–201, 2014.
- [19] G. Palli, G. Borghesan, and C. Melchiorri. Modeling, identification and control of tendon-based actuation systems. *IEEE Trans. on Robotics*, 28(2):277–290, 2012.
- [20] H. Olsson, K. J. Aström, C. Canudas de Wit, M. Gäfvert, and P. Lischinsky. Friction models and friction compensation. *European Journal of Control*, 4(3):176–195, 1998.
- [21] A. Bicchi, G. Tonietti, M. Bavaro, and M. Piccigallo. *Variable Stiffness Actuators for Fast and Safe Motion Control*, volume 15 of *Springer Tracts in Advanced Robotics*. Springer Berlin / Heidelberg, 2005.
- [22] R. Schiavi, G. Grioli, S. Sen, and A. Bicchi. VSA-II: a novel prototype of variable stiffness actuator for safe and performing robots interacting with humans. In *Proc. of the IEEE Int. Conf. on Robotics and Automation*, pages 2171 – 2176, Pasadena, CA, May 19-23 2008.
- [23] S. Wolf and G. Hirzinger. A new variable stiffness design: Matching requirements of the next robot generation. In *Proc. of the IEEE Int. Conf. on Robotics and Automation*, Pasadena, CA, May 19-23 2008.
- [24] I Sardellitti, G. Palli, N.G. Tsagarakis, and D.G. Caldwell. Antagonistically actuated compliant joint: Torque and stiffness control. In *Proc. IEEE/RSJ Int. Conf. on Intelligent Robots and Systems*, pages 1909–1914, Oct 2010.
- [25] A Jafari, N.G. Tsagarakis, and D.G. Caldwell. AwAS-II: A new actuator with adjustable stiffness based on the novel principle of adaptable pivot point and variable lever ratio. In *Proc. IEEE Int. Conf. on Robotics and Automation*, pages 4638–4643, May 2011.
- [26] L.C. Visser, R. Carloni, and S. Stramigioli. Energy-efficient variable stiffness actuators. *IEEE Trans. on Robotics*, pages 865–875, 2011.
- [27] B. Vanderborght, A. Albu-Schaeffer, A. Bicchi, E. Burdet, D.G. Caldwell, R. Carloni, M. Catalano, O. Eiberger, W. Friedl, G. Ganesh, M. Garabini, M. Grebenstein, G. Grioli, S. Haddadin, H. Hoppner, A. Jafari, M. Laffranchi, D. Lefeber,

- F. Petit, S. Stramigioli, N. Tsagarakis, M. Van Damme, R. Van Ham, L.C. Visser, and S. Wolf. Variable impedance actuators: A review. *Robotics and Autonomous Systems*, 61(12):1601–1614, 2013.
- [28] G. Palli and S. Pirozzi. Optical sensor for angular position measurements embedded in robotic finger joints. *Advanced Robotics*, 27(15):1209–1220, 2013.
- [29] Farrokh Janabi-Sharifi, Vincent Hayward, and Chung-Shin J. Chen. Discrete-time adaptive windowing for velocity estimation. *IEEE Trans. on Control Systems technology*, 8(6):1003–1009, 2000.
- [30] F. Flacco and A De Luca. Residual-based stiffness estimation in robots with flexible transmissions. In *Proc. IEEE Int. Conf. on Robotics and Automation*, pages 5541–5547, Shanghai, China, May 2011.
- [31] Aaron M Dollar and Hugh Herr. Lower extremity exoskeletons and active orthoses: challenges and state-of-the-art. *Robotics, IEEE Transactions on*, 24(1):144–158, 2008.
- [32] RARC Gopura and Kazuo Kiguchi. Mechanical designs of active upper-limb exoskeleton robots: State-of-the-art and design difficulties. In *Rehabilitation Robotics, 2009. ICORR 2009. IEEE International Conference on*, pages 178–187. IEEE, 2009.
- [33] E Winder, C A Pomeroy, and U C Wejinya. Closed-loop optimal control-enabled piezoelectric microforce sensors. *IEEE/ASME Trans. on Mechatronics*, 11(4):420–427, 2006.
- [34] W.A. Lorenz, M.A. Peshkin, and J.E. Colgate. New sensors for new applications: force sensors for human/robot interaction. In *Proc. IEEE Int. Conf. on Robotics and Automation*, volume 4, pages 2855–2860, 1999.
- [35] J. Peirs, J. Clijnen, D. Reynaerts, H. Van Brussel, P. Herijgers, B. Corteville, and S. Boone. A micro optical force sensor for force feedback during minimally invasive robotic surgery. *Sensors and Actuators A: Physical*, 115(2–3):447–455, 2004.
- [36] G. Palli and S. Pirozzi. Force sensor based on discrete optoelectronic components and compliant frames. *Sensors and Actuators A: Physical*, 165:239–249, 2011.

- [37] G. Palli and S. Pirozzi. A miniaturized optical force sensor for tendon-driven mechatronic systems: Design and experimental evaluation. *Mechatronics*, 22(8): 1097–1111, 2012.
- [38] G. Borghesan, G. Palli, and C. Melchiorri. Design of tendon-driven robotic fingers: Modeling and control issues. In *Proc. IEEE Int. Conf. on Robotics and Automation*, pages 793–798, Anchorage, AK, 2010.
- [39] Mitsunori Tada and Takeo Kanade. Design of an mr-compatible three-axis force sensor. In *Intelligent Robots and Systems, 2005.(IROS 2005). 2005 IEEE/RSJ International Conference on*, pages 3505–3510. IEEE, 2005.
- [40] Jeroen Missinne, Erwin Bosman, Bram Van Hoe, Geert Van Steenberge, Sandeep Kalathimekkad, Peter Van Daele, and Jan Vanfleteren. Flexible shear sensor based on embedded optoelectronic components. *Photonics Technology Letters, IEEE*, 23(12):771–773, 2011.
- [41] S. Hirose and K. Yoneda. Development of optical 6-axial force sensor and its signal calibration considering non linear calibration. In *Proc. IEEE Int. Conf. on Robotics and Automation*, volume 1, pages 46–53, Tsukuba, Japan, 1990.
- [42] J. Heo, J. Chung, and J. Lee. Tactile sensor arrays using fiber bragg grating sensors. *Sensors and Actuators A: Physical*, 126(2):312–327, 2006.
- [43] K. Kamiyama, K. Vlack, T. Mizota, H. Kajimoto, N. Kawakami, and S. Tachi. Vision-based sensor for real-time measuring of surface traction fields. *Computer Graphics and Applications, IEEE*, 25(1):68–75, 2005.
- [44] R. Coral E. Torres-Jara, I. Vasilescu. A soft touch: compliant tactile sensors for sensitive manipulation. In *CSAIL Technical Report MIT-CSAIL-TR-2006-014*, 2006.
- [45] R.A. Russell G. Hellard. A robust, sensitive and economical tactile sensor for a robotic manipulator. In *Proc. of Australasian Conference on Robotics and Automation*, pages 100–104, 2002.
- [46] G. De Maria, C. Natale, and S. Pirozzi. Force/tactile sensor for robotic applications. *Sensors and Actuators A: Physical*, 175:60–72, 2012.

-
- [47] A. Tar and G. Cserey. Development of a low cost 3d optical compliant tactile force sensor. In *Proc. IEEE/ASME Int. Conf. Advanced Intelligent Mechatronics*, pages 236–240, 2011.
- [48] Hao Su, Michael Zervas, Cosme Furlong, and Gregory S Fischer. A miniature mri-compatible fiber-optic force sensor utilizing fabry-perot interferometer. In *MEMS and Nanotechnology, Volume 4*, pages 131–136. Springer, 2011.
- [49] J Gafford, F Doshi-Velez, R Wood, and C Walsh. Machine learning approaches to environmental disturbance rejection in multi-axis optoelectronic force sensors. *Sensors and Actuators A: Physical*, 248:78–87, 2016.
- [50] S.O. Kasap. *Optoelectronics and Photonics: Principles and Practices*. Prentice Hall, Englewood Cliffs, NJ, 2001.
- [51] Joseph Edward Shigley. *Shigley’s mechanical engineering design*. Tata McGraw-Hill Education, 2011.
- [52] Joel C Perry, Jacob Rosen, and Stephen Burns. Upper-limb powered exoskeleton design. *IEEE/ASME transactions on mechatronics*, 12(4):408, 2007.
- [53] Zhichuan Tang, Kejun Zhang, Shouqian Sun, Zenggui Gao, Lekai Zhang, and Zhongliang Yang. An upper-limb power-assist exoskeleton using proportional myoelectric control. *Sensors*, 14(4):6677–6694, 2014.
- [54] Ignacio Galiana, Frank L Hammond, Robert D Howe, and Marko B Popovic. Wearable soft robotic device for post-stroke shoulder rehabilitation: Identifying misalignments. In *Proc. IEEE/RSJ Int. Conf. on Intelligent Robots and Systems*, pages 317–322, 2012.
- [55] Barkan Ugurlu, Masayoshi Nishimura, Kazuyuki Hyodo, Michihiro Kawanishi, and Tatsuo Narikiyo. Proof of concept for robot-aided upper limb rehabilitation using disturbance observers. *IEEE Trans. on Human-Machine Systems*, 45(1):110–118, 2015.
- [56] Joel C Perry and Jacob Rosen. Design of a 7 degree-of-freedom upper-limb powered exoskeleton. In *Proc. IEEE/RAS-EMBS Int. Conf. on Biomedical Robotics and Biomechatronics*, pages 805–810, 2006.

- [57] Ying Mao and Sunil Kumar Agrawal. Design of a cable-driven arm exoskeleton (carex) for neural rehabilitation. *IEEE Trans. on Robotics*, 28(4):922–931, 2012.
- [58] Ranathunga Arachchilage Ruwan Chandra Gopura and Kazuo Kiguchi. Development of a 6dof exoskeleton robot for human upper-limb motion assist. In *Proc. Int. Conf. on Information and Automation for Sustainability*, pages 13–18, 2008.
- [59] Hiroshi Kobayashi and Hirokazu Nozaki. Development of muscle suit for supporting manual worker. In *Proc. IEEE/RSJ Int. Conf. on Intelligent Robots and Systems*, pages 1769–1774, 2007.
- [60] H. Dong and N. Mavridis. Adaptive biarticular muscle force control for humanoid robot arms. In *Proc. IEEE-RAS Int. Conf. on Humanoid Robots*, pages 284–290, 2012.
- [61] G Palli, M Hosseini, and C Melchiorri. Experimental evaluation of guided twisted actuation. *IFAC-PapersOnLine*, 49(21):380–385, 2016.
- [62] S. Benatti, B. Milosevic, F. Casamassima, P. Sch[^]nle, P. Bunjaku, S. Fateh, Q. Huang, and L. Benini. EMG-based hand gesture recognition with flexible analog front end. In *Proc. IEEE Biomedical Circuits and Systems Conference*, pages 57–60, Oct 2014.
- [63] P. Sch[^]nle, F. Schulthess, S. Fateh, R. Ulrich, F. Huang, T. Burger, and Q. Huang. A DC-connectable multi-channel biomedical data acquisition ASIC with mains frequency cancellation. In *Proc. ESSCIRC*, pages 149–152, Sept 2013.
- [64] R. Meattini, S. Benatti, U. Scarcia, L. Benini, and C. Melchiorri. Experimental evaluation of a sEMG-based human-robot interface for human-like grasping tasks. In *Proc. IEEE Int. Conf. on Robotics and Biomimetics*, pages 1030–1035, Dec 2015.
- [65] A. Perotto and E.F. Delagi. *Anatomical Guide for the Electromyographer: The Limbs and Trunk*. Charles C Thomas, 2005.
- [66] Thomas B Sheridan, Dana S Kruser, and Stanley Deutsch. Human factors in automated and robotic space systems: Proceedings of a symposium. part 1. 1987.

- [67] Yuichi Tsumaki, Hitoshi Naruse, Dragomir N Nenchev, and Masaru Uchiyama. Design of a compact 6-dof haptic interface. In *Robotics and Automation, 1998. Proceedings. 1998 IEEE International Conference on*, volume 3, pages 2580–2585. IEEE, 1998.
- [68] Sung-Uk Lee, S Hochul, and S Kim. Design of a new haptic device using a parallel gimbal mechanism. In *International Conference on Computer Applications in Shipbuilding. ICCAS*, 2005.
- [69] Tian Qiu, William R Hamel, and Dongjun Lee. Design and control of a low cost 6 dof master controller. In *Robotics and Automation (ICRA), 2014 IEEE International Conference on*, pages 5313–5318. IEEE, 2014.
- [70] Minh Hung Vu and Uhn Joo Na. A new 6-dof haptic device for teleoperation of 6-dof serial robots. *IEEE Transactions on Instrumentation and Measurement*, 60(11):3510–3523, 2011.
- [71] Soo S. Lee and Jang M. Lee. Design of a general purpose 6-dof haptic interface. *Mechatronics*, 13(7):697 – 722, 2003. ISSN 0957-4158. doi: [http://dx.doi.org/10.1016/S0957-4158\(02\)00038-7](http://dx.doi.org/10.1016/S0957-4158(02)00038-7). URL <http://www.sciencedirect.com/science/article/pii/S0957415802000387>.
- [72] Dongseok Ryu, Jae-Bok Song, Changhyun Cho, Sungchul Kang, and Munsang Kim. Development of a six dof haptic master for teleoperation of a mobile manipulator. *Mechatronics*, 20(2):181–191, 2010.
- [73] Thomas H Massie, J Kenneth Salisbury, et al. The phantom haptic interface: A device for probing virtual objects. In *Proceedings of the ASME winter annual meeting, symposium on haptic interfaces for virtual environment and teleoperator systems*, volume 55, pages 295–300, 1994.
- [74] URL <http://www.geomagic.com/en/products/phantom-omni/overview/>.
- [75] Force Dimension website. Force Dimension Haptic Devices, 2017. URL <http://www.forcedimension.com/>.
- [76] URL <http://www.novint.com/>.

- [77] Richard Q Van der Linde, Piet Lammertse, Erwin Frederiksen, and B Ruiter. The hapticmaster, a new high-performance haptic interface. In *Proc. Eurohaptics*, pages 1–5, 2002.
- [78] URL <http://butterflyhaptics.com/products/>.
- [79] Paolo Gallina, Giulio Rosati, and Aldo Rossi. 3-dof wire driven planar haptic interface. *Journal of Intelligent & Robotic Systems*, 32(1):23–36, 2001.
- [80] C Bonivento, A Eusebi, C Melchiorri, M Montanari, and G Vassura. Wireman: A portable wire manipulator for touch-rendering of bas-relief virtual surfaces. In *Advanced Robotics, 1997. ICAR'97. Proceedings., 8th International Conference on*, pages 13–18. IEEE, 1997.
- [81] Robert L Williams, Venkat Chadaram, and Federica Giacometti. Three-cable haptic interface. In *ASME 2006 International Design Engineering Technical Conferences and Computers and Information in Engineering Conference*, pages 817–824. American Society of Mechanical Engineers, 2006.
- [82] Masahiro Ishii and Makoto Sato. A 3d spatial interface device using tensed strings. *Presence: Teleoperators and Virtual Environments*, 3(1):81–86, 2017/02/18 1994. doi: 10.1162/pres.1994.3.1.81. URL <http://dx.doi.org/10.1162/pres.1994.3.1.81>.
- [83] Randel Lindemann and Delbert Tesar. Construction and demonstration of a 9-string 6 dof force reflecting joystick for telerobotics. 1989.
- [84] M Ishii and M Sato. Six degree-of-freedom master using eight tensed strings. In *ISMCR'98, Proc. of the Eighth Internat. Symp. on Measurement and Control in Robotics*, volume 455, pages 251–255, 1998.
- [85] G Palli, M Hosseini, and C Melchiorri. Experimental evaluation of guided twisted actuation. *IFAC-PapersOnLine*, 49(21):380–385, 2016.
- [86] Takashi Sonoda and Ivan Godler. Multi-fingered robotic hand employing strings transmission named “twist drive”. In *Intelligent Robots and Systems (IROS), 2010 IEEE/RSJ International Conference on*, pages 2733–2738. IEEE, 2010.
- [87] Gianluca Palli, Claudio Melchiorri, Gabriele Vassura, U Scarcia, Lorenzo Moriello, Giovanni Berselli, Alberto Cavallo, Giuseppe De Maria, Ciro Natale, Salvatore

- Pirozzi, et al. The dexmart hand: Mechatronic design and experimental evaluation of synergy-based control for human-like grasping. *The International Journal of Robotics Research*, 33(5):799–824, 2014.
- [88] In-Won Park and Vytas SunSpiral. Impedance controlled twisted string actuators for tensegrity robots. In *Control, Automation and Systems (ICCAS), 2014 14th International Conference on*, pages 1331–1338. IEEE, 2014.
- [89] M. Hosseini, R. Meattini, G. Palli, and C. Melchiorri. Development of semg-driven assistive devices based on twisted string actuation. In *Proc. IEEE Conf. on Control, Automation, Robotics (ICCAR 2017)*, 2017.
- [90] M Hosseini, G Palli, and C Melchiorri. Design and implementation of a simple and low-cost optoelectronic force sensor for robotic applications. In *Advanced Intelligent Mechatronics (AIM), 2016 IEEE International Conference on*, pages 1011–1016. IEEE, 2016.
- [91] ABSplus-P430 Production Grade Thermoplastic for Design Series 3D Printers. URL http://usglobalimages.stratasys.com/Main/Files/Material_Spec_Sheets/MSS_FDM_ABSplusP430.pdf.
- [92] I. Ivanisevic and V. J. Lumelsky. Configuration space as a means for augmenting human performance in teleoperation tasks. *Trans. Sys. Man Cyber. Part B*, 30(3): 471–484, 2000.
- [93] R. V. Dubey, S. E. Everett, N. Pernaleté, and K. A. Manocha. Teleoperation assistance through variable velocity mapping. *IEEE Trans. on Robotics and Automation*, 17(5):761–766, 2001.
- [94] M. Guthold, M. R. Falvo, W. G. Matthews, S. Paulson, S. Washburn, D. A. Erie, R. Superfine, F. P. Brooks, and R. M. Taylor. Controlled manipulation of molecular samples with the nanomanipulator. *IEEE/ASME Trans. on Mechatronics*, 5(2): 189–198, 2000.
- [95] Sylvain Marlière, Daniela Urma, Jean-Loup Florens, and Florence Marchi. Multi-sensorial interaction with a nano-scale phenomenon: the force curve. In *Proc. of EuroHaptics*, pages 246–253, 2004.

-
- [96] A. Bardorfer, M. Munih, A. Zupan, and A. Primožic. Upper limb motion analysis using haptic interface. *IEEE/ASME Trans. on Mechatronics*, 6(3):253–260, 2001.
- [97] C. Basdogan, C. H. Ho, and M. A. Srinivasan. Virtual environments for medical training: graphical and haptic simulation of laparoscopic common bile duct exploration. *IEEE/ASME Transactions on Mechatronics*, 6(3):269–285, 2001.
- [98] H. Kawasaki, Yasuhiko Doi, Shinya Koide, T. Endo, and T. Mouri. Hand haptic interface incorporating 1d finger pad and 3d fingertip force display devices. In *Proc. Int. Symposium on Industrial Electronics*, pages 1869–1874, 2010.
- [99] H. Kawasaki and T. Mouri. Design and control of five-fingered haptic interface opposite to human hand. *IEEE Trans. on Robotics*, 23(5):909–918, 2007.
- [100] Jamshed Iqbal, Hamza Khan, Nikos G. Tsagarakis, and Darwin G. Caldwell. A novel exoskeleton robotic system for hand rehabilitation ,À conceptualization to prototyping. *Biocybernetics and Biomedical Engineering*, 34(2):79 – 89, 2014.
- [101] Alessandro Battezzato. Towards an underactuated finger exoskeleton: An optimization process of a two-phalange device based on kinetostatic analysis. *Mechanism and Machine Theory*, 78:116 – 130, 2014.
- [102] Alessandro Battezzato. Kinetostatic analysis and design optimization of an n-finger underactuated hand exoskeleton. *Mechanism and Machine Theory*, 88:86 – 104, 2015.
- [103] Sang Wook Lee, Katlin A Landers, and Hyung-Soon Park. Development of a biomimetic hand extensor device (biomhed) for restoration of functional hand movement post-stroke. *IEEE Trans. on Neural Systems and Rehabilitation Engineering*, 22(4):886–898, 2014.
- [104] C. A. Avizzano, F. Bargagli, A. Frisoli, and M. Bergamasco. The hand force feedback: analysis and control of a haptic device for the human-hand. In *Systems, Man, and Cybernetics, 2000 IEEE International Conference on*, volume 2, pages 989–994 vol.2, 2000.
- [105] Merwan Achibet, Géry Casiez, and Maud Marchal. DesktopGlove: a Multi-finger Force Feedback Interface Separating Degrees of Freedom Between Hands. In

- IEEE Computer Society, editor, *3DUI'16, the 11th Symposium on 3D User Interfaces*, Proc. of the Symposium on 3D User Interfaces, page 10, Greenville, United States, 2016.
- [106] Péter Galambos. Vibrotactile feedback for haptics and telemanipulation: Survey, concept and experiment. *Acta Polytechnica Hungarica*, 9(1):41–65, 2012.
- [107] R Montaña-Murillo, R Posada-Gómez, A Martínez-Sibaja, BE Gonzalez-Sanchez, AA Aguilar-Lasserre, and P Cornelio-Martínez. Design and assessment of a remote vibrotactile biofeedback system for neuromotor rehabilitation using active markers. *Procedia Technology*, 7:96–102, 2013.
- [108] Pontus Olsson, Stefan Johansson, Fredrik Nysjö, and Ingrid Carlbom. Rendering stiffness with a prototype haptic glove actuated by an integrated piezoelectric motor. In *International Conference on Human Haptic Sensing and Touch Enabled Computer Applications*, pages 361–372. Springer, 2012.
- [109] C. Tejeiro, C. E. Stepp, M. Malhotra, E. Rombokas, and Y. Matsuoka. Comparison of remote pressure and vibrotactile feedback for prosthetic hand control. In *2012 4th IEEE RAS EMBS International Conference on Biomedical Robotics and Biomechatronics (BioRob)*, pages 521–525, 2012.
- [110] Gregg A. Tabot, John F. Dammann, Joshua A. Berg, Francesco V. Tenore, Jessica L. Boback, R. Jacob Vogelstein, and Sliman J. Bensmaia. Restoring the sense of touch with a prosthetic hand through a brain interface. *Proceedings of the National Academy of Sciences*, 110(45):18279–18284, 2013.